

https://dspace.org/

Are Fe and Co implanted ZnO and III-nitride semiconductors magnetic?

Masenda, Hilary

2014-07-22
http://hdl.handle.net/10539/14962

Downloaded from a DSpace repository. https://dspace.org/

Are Fe and Co implanted ZnO and III-nitride semiconductors magnetic?

Hilary Masenda

A thesis submitted to the Faculty of Science, University of the Witwatersrand, Johannesburg, in fulfilment of the academic requirements for the degree of Doctor of Philosophy.

Johannesburg
February 2014

Declaration

The experimental work described in this thesis was performed as part of the following major projects: (i) "*Emission Mössbauer spectroscopy of advanced materials for opto- and nano- electronics*" and (ii) "*Formation and Shaping of Magnetic Nano-clusters in Ion implanted Oxides*".

Project (i) was undertaken at the ISOLDE facility, CERN. The measurements were carried out within the Mössbauer Collaboration (IS501) with following participating organisations: University of the Witwatersrand, University of the KwaZulu-Natal, Aarhus University (Denmark), University of Iceland (Iceland), University of Leuven (Belgium), University of Copenhagen (Denmark) and the Laboratorio Nazionale MDM CNR-INFM (Italy).

The first part of Project (ii) involved pre-implantation and/or preparation of ZnO samples by ion implantation of stable isotopes carried out at the Institute of Solid State Physics, University of Jena by Dr S. Geburt. The second part of the project incorporated conversion electron Mössbauer spectroscopy (CEMS) and vibrating sample magnetometer (VSM) measurements carried out at iThemba LABS, Cape Town under the supervision of Professors K. Bharuth-Ram and T. B. Doyle, respectively. The principal investigators of the overall project are Professors K. Bharuth-Ram and C. Ronning, University of Jena.

In addition to the preparation and participation in the experiments at ISOLDE and measurements at iThemba LABS, the data analysis and understanding of results was carried under the guidance of Prof D. Naidoo (principal supervisor) and Prof K. Bharuth-Ram (co-supervisor).

I declare that this thesis has not been submitted before for any degree or diploma examination in any other tertiary institution.

Signed:_____.
Hilary Masenda
February 17, 2014

Abstract

The chemical nature, lattice site locations and magnetic behaviour of Fe and/or Co ions implanted in nitrides (GaN, AlN, and InN) and in ZnO have been investigated using Mössbauer spectroscopy and vibrating sample magnetometer (VSM) techniques.

Mössbauer data on nitride and ^{56}Fe pre-implanted ZnO samples were obtained from emission Mössbauer spectroscopy (eMS) measurements at the ISOLDE facility, CERN, following the implantation of radioactive $^{57}Mn^{*}$ which β-decays to the 14.4 keV Mössbauer state of ^{57}Fe. In addition, conversion electron Mössbauer spectroscopy (CEMS) data were collected on ZnO single crystals co-implanted with ^{57}Fe + ^{56}Fe and ^{57}Fe + ^{59}Co ions in a box profile.

Emission Mössbauer spectra obtained for GaN and AlN reveal magnetic structure in the 'wings' assigned to high spin Fe^{3+} weakly coupled to the lattice showing spin-lattice relaxation effects. The observed spin-relaxation rate (τ^{-1}) closely follows a T^2 temperature dependence, typical of a two-phonon Raman process expected in the high temperature region. The spectra for InN did not display any magnetic structure, presumably due to the absence of high spin Fe^{3+}. The central region of the spectra for all nitride samples showed an angle dependence reflecting the crystalline nature of the environment of most ^{57}Fe probes while a small fraction was attributed to implantation induced damage in isolated amorphous regions. The absence of recoil produced interstitials in the nitride samples could be explained by displacement energies of III sublattice atoms being greater than the recoil imparted to the ^{57}Fe ions in the $^{57}Mn^{*}$ β-decay, resulting in the daughter ^{57}Fe maintaining the substitutional lattice site occupied by $^{57}Mn^{*}$ upon implantation.

For the ^{56}Fe pre-implanted ZnO samples, magnetic structure is visible in the 'wings' of the spectra as observed previously for virgin ZnO. The spin-lattice relaxation rates of Fe^{3+} in the pre-implanted ZnO samples increase with increasing fluence at equivalent temperatures.

Strong magnetic features are evident in the CEMS spectrum of ZnO:^{57}Fe+^{56}Fe after annealing at 973 K which are attributed to different Fe sites in ε-Fe_2O_3 nanoparticles. This result is supported by VSM measurements conducted at 4 K and

293 K showing ferromagnetic signals with coercive fields of ~0.08 T and ~0.02 T, and corresponding remanent magnetisation fields which are ~62% and ~34% of the saturation magnetisation at respective temperatures. The spectrum for ZnO:^{57}Fe+^{59}Co did not reveal any magnetic feature at 973 K, but shows a switch to hyperfine parameters consistent with Fe^{3+} in different local environments. The absence of any magnetic structure in the spectra suggests the absence of ε-Fe_2O_3, attributed to low concentration of Fe atoms.

The spin-lattice relaxation rates of Fe^{3+}, lattice site locations, annealing behaviour and variation of hyperfine parameters of spectral components as a function of temperature in these materials are discussed.

In addition, a report on the development of a new parallel plate avalanche counter (PPAC) based on an FeAl single line electrode is presented.

To

Innocent and Lawrence

Thank You!

Acknowledgements

The success of any project is usually a combination of many hands and minds, in that regard, I wish to take this opportunity to recognise a number of people who have contributed greatly towards of my studies.

I am greatly indebted to my supervisor, *Prof Deena Naidoo* and co-supervisor, *Prof Krish Bharuth-Ram* for their mentorship and guidance during my studies and for bringing me into international collaborations. I appreciate their efforts and time taken to read through analysis reports and the drafts of my thesis with a critical eye and for their encouragements, comments, suggestions, and time consuming consultations in spite of various other commitments. More importantly, I would like to take this opportunity to thank them for sharing their expertise in different aspects of research in Mössbauer spectroscopy and ion-solid interaction; you both have done a commendable job that is worth recognition.

Secondly, I am deeply grateful to my collaborators, specifically; *Prof H. P. Gunnlaugsson* for his suggestions on potential analysis models and advice during the experimental work at ISOLDE, *Prof T. B. Doyle* for his insights and expertise during VSM measurements, and *Prof C. Ronning* for his suggestions and correspondence concerning different aspects of the particular project. Moreover, I would like to express my appreciation to all the members of the $^{57}Mn^{*}$ *Mössbauer Collaboration at ISOLDE* for all their assistance during experiments, useful discussions during research review meetings, and stimulating discussions. Furthermore, a special recognition to *Dr S. Geburt* and *S. Milz* for stable implantations and all their assistance. In addition, many thanks to you all for your friendships and hospitality during beam-times and my research visits at your respective institutions.

I am grateful for funding from the National Research Foundation (NRF) through the grant-linked bursary scheme, the SA-CERN program for funding all ISOLDE related trips covering air fares, accommodation and subsistence, the Bradlow Foundation, WITS Financial Aid for the merit awards, the JC Carstens Foundation and the Mary Scholes scholarships for financial support towards my subsistence in

my final year. Moreover, I would like to acknowledge additional financial support from my supervisors especially during my final year for fees and living expenses.

Many thanks to both academic and administrative staff in the School of Physics, University of the Witwatersrand and iThemba LABS, Cape Town, who have contributed in one way or another towards my studies, even though parts of the other research projects you were involved and offered your assistance are not discussed in this report.

Moreover, my appreciation goes to all who have read through the draft copy of my thesis and offered their suggestions, especially *Dr K. Johnston* and *Dr P. S. Fasinu*.

A special thanks to friends and colleagues; *Kuda, Mehluli, Wisdom, Motochi, Lawrence, Stewart, Tino, Modjadji, Desmond, Cindy, Mrs E. Nkiwane, Eugene (Mtax), Philemon, Patrick, Mai Shope,* and all those whose names may not be mentioned but have contributed in various way. Not forgetting clergy and parishioners of Holy Trinity Catholic Church - Braamfontein and the Young Adults.

My sincere gratitude also goes to my *family*, and my best friend and fiancée *Shelly* for all their support and encouragement during the course of my studies.

Finally, *Ad maiorem Dei gloriam*, for "...*in Him all things hold together*" Col 1:17.

"Crystals are like people: it is the defects in them that make them interesting"

Sir Charles Frank

Table of Contents

Declaration ii
Abstract iii
Dedication v
Acknowledgements vi
Table of Contents ix
List of Figures xiii
List of Tables xviii

Introduction 1
Overview of thesis 4

Chapter 1 5
Fundamental Concepts and Literature Review 5
1.1. Properties of III-nitrides and ZnO 5
1.2. Point defects 7
1.3. Literature Survey 7
1.3.1. Displacement energies 7
1.3.2. Defects, radiation damage and annealing processes 9
1.3.3. Site location and charge states of dopant ions 12
1.3.4. Magnetism in transition metal doped ZnO and III-nitrides 15
1.3.5. Exchange interactions 17
1.3.6. Overview of literature review 18
1.4. A summary of emission Mössbauer measurements in oxides 20
1.5. Paramagnetic relaxation 22
1.5.1. Spin-lattice relaxation 22
1.5.2. Spin-spin relaxation 24
1.6. Aims and Objectives 24

Chapter 2 27
Mössbauer Effect and Hyperfine Parameters 27
2.1. The Mössbauer effect 27
2.2. Recoil free fraction 28
2.3. Spectral line shape and natural linewidth 29
2.4. Mössbauer isotope: ^{57}Fe 30

2.5. Mössbauer spectrum 31
2.6. Hyperfine interaction parameters 32
2.6.1. Isomer Shift: Electric Monopole Interaction 33
2.6.2. Quadrupole Splitting: Electric Quadrupole Interaction 35
2.6.3. Magnetic Splitting: Magnetic Dipole Interaction 38
2.6.4. Combined magnetic and quadrupole interactions 40
2.6.5. Angular dependence of hyperfine parameters 40
2.6.5.1. Quadrupole splitting 40
2.6.5.2. Magnetic splitting 41
2.6.6. Temperature dependence of hyperfine parameters 41
2.6.6.1. Thermal vibrations: Second order Doppler Shift 41
2.6.6.2. Quadrupole Splitting 42
2.6.7. Relaxation in Mössbauer Spectroscopy 43

Chapter 3 44

Materials Modification and Experimental Details 44

3.1. Description of samples 44
3.2. Material modification by ion implantation 47
3.3. Implantation profiles, parameters and fluences 48
3.3.1. $^{57}Mn^{*}$ in Nitrides and ZnO 48
3.3.2. ^{56}Fe pre-implanted ZnO samples 49
3.3.3. "Box" Profile Samples 49
3.3.3.1. ZnO:^{56}Fe+^{57}Fe 49
3.3.3.2. ZnO:^{59}Co+^{57}Fe 50
3.4. Mössbauer Spectroscopy 51
3.5. Conversion Electron Mössbauer Spectroscopy 51
3.5.1. CEMS Measurements and annealing conditions 52
3.6. Emission Mössbauer Spectroscopy at ISOLDE 52
3.6.1. Beam production 53
3.6.2. Experimental set-up 53
3.6.3. Resonance detectors 55
3.6.3.1. ^{57}Fe enriched stainless steel detector 55
3.6.3.2. CEMS Detector 57
3.6.4. Mössbauer electronics 57

3.6.5. eMS measurements 58
3.6.6. Comparison of strengths and weaknesses of Mössbauer spectroscopic techniques 59
3.7. Vibrating Sample Magnetometer 60
3.7.1. Principle of operation 60
3.7.2. VSM measurements 62
3.8. Summary of measurements 62

Chapter 4 65
Analysis, Results and Discussion 65
4.1. eMS measurements on nitrides 65
4.1.1. Analysis and Results: GaN 66
4.1.1.1. Lattice site assignments 71
4.1.1.2. Temperature dependence of hyperfine parameters in GaN 73
4.1.1.3. Annealing Behaviour 77
4.1.2. Analysis and Results: AlN 79
4.1.2.1. Lattice site location 81
4.1.2.2. Temperature dependence of hyperfine parameters in AlN 82
4.1.2.3. Area Fractions 86
4.1.3. Analysis and Results: InN 88
4.1.3.1. Nature of Fe in InN 89
4.1.3.2. Temperature dependence of hyperfine parameters 91
4.1.3.3. Annealing Behaviour 92
4.1.4. Absence of interstitials in nitrides 93
4.1.5. Summary of results in III-nitrides 94
4.2. Virgin ZnO and ^{56}Fe pre-implanted ZnO 96
4.2.1. Hyperfine interaction (HI) parameters 101
4.2.2. Fluence dependence of crystal field splitting values for Fe_C. 102
4.2.3. Properties of the magnetic component 102
4.2.4. Variation of relative area fraction with temperature 103
4.2.5. Relaxation Rates 105
4.2.6. Summary of Results in ^{56}Fe pre-implanted ZnO 106
4.3. ZnO samples implanted with box profile of ^{56}Fe and ^{59}Co 107
4.3.1. ZnO:^{57}Fe+^{56}Fe 107

4.3.1.1. Conversion Electron Mössbauer Spectroscopy (CEMS) studies. 107
4.3.1.2. VSM studies 111
4.3.2. ZnO:^{57}Fe+^{59}Co 113
4.3.2.1. CEMS Results 113
4.3.3. Summary of results in box profile implanted ZnO samples 115
4.4. Overview of Results 116

Chapter 5 120
Concluding Remarks 120

Appendix A: Basics on Magnetism 124
A.1. Magnetism 124
A.1.1. Classes of magnetic materials 124
A.1.1.1. Diamagnetism 124
A.1.1.2. Paramagnetism 125
A.1.1.3. Ferrimagnetism 126
A.1.1.4. Ferromagnetism 127
A.1.1.5. Antiferromagnetism 129
A.1.2. Density of states on ferromagnetic material 129

Appendix B: FeAl Detector Development 131
B.1. Introduction 131
B.2. FeAl sample preparation 131
B.3. Typical FeAl Mössbauer Spectrum 131
B.4. Theory behind offline tests 132
B.5. Offline Tests Measurements 133
B5.1. Data Analysis and Results 133
B.6. Online Detector Tests Measurements 135
B.7. Conclusion and Future Tests 136

References 137

List of Figures

Figure 1.1: Wurtzite crystal structure of GaN: (a) 2×2 unit cells, (b) unit cell and (c) view along the *c*-axis. 6
Figure 1.2: A schematic illustration of different types of point defects..... 7
Figure 1.3: Processes that contribute to spin-lattice relaxations: (a) Direct process, (b) Orbach process and (c) Raman Process 22
Figure 2.1: Non-resonant γ-ray absorption due to loss in energy to recoil. 27
Figure 2.2: Resonant emission and absorption of γ-photon between nuclei, and resonance fluorescence and conversion electrons. 28
Figure 2.3: Intensity distribution for γ-ray emission as a function of transition energy E_0 where *e* and *g* are excited and ground states, respectively.30
Figure 2.4: Decay schemes for $^{57}Mn^{*}$, $^{57}Co^{*}$ and ^{57}Fe 31
Figure 2.5: Progress in the development of an emission Mössbauer spectrum. ... 32
Figure 2.6: The nuclear energy levels shifts in the source and absorber due to the electric monopole interaction (a) resulting in the Mössbauer isomer shift shown in (b)..... 33
Figure 2.7: Isomer shift values observed for ^{57}Fe compounds measured relative to α-Fe at room temperature. 35
Figure 2.8: Splitting of the energy level in the ^{57}Fe state with I=3/2 resulting in quadrupole splitting of the resulting Mössbauer spectrum. 37
Figure 2.9: Magnetic dipole interaction resulting in the nuclear Zeeman splitting of the energy levels and the Mössbauer spectrum showing a sextet .39
Figure 3.1: XRD pattern for AlN film on a Sapphire substrate. 45
Figure 3.2: XRD pattern for GaN film on a Sapphire substrate..... 46
Figure 3.3: XRD pattern for InN film on GaN/Sapphire substrates 46
Figure 3.4: XRD patterns for ZnO single crystal. 47
Figure 3.5: Implantation profile for $^{57}Mn^{*}$ in (a) nitrides and (b) ZnO at $\theta_1 = 60^{o}$. 48
Figure 3.6: Implantation profile for ZnO implanted with ^{56}Fe. 49
Figure 3.7: Implantation profile of ^{57}Fe and ^{56}Fe in ZnO. 50
Figure 3.8: (a) Implantation profile for ^{57}Fe and ^{59}Co in ZnO and (b) Fe/Co ratio as a function of depth. 50
Figure 3.9: Decay scheme for ^{57}Co to ^{57}Fe and different backscattering processes for ^{57}Fe following resonant absorption of an incident γ-ray. 52

Figure 3.10: Beam production at ISOLDE. 53
Figure 3.11: Pictorial image of the experimental set-up for emission Mössbauer spectroscopy at ISOLDE. 54
Figure 3.12: A cross-sectional view of a typical PPAC. 55
Figure 3.13: Schematic diagram of the experimental set-up and electronics at ISOLDE. 57
Figure 3.14: Cross-sectional view of a VSM system with insert showing the working principle. 61
Figure 4.1: (a) Emission Mössbauer spectrum of GaN obtained at 300 K and at an emission angle of 60^o and (b) zoomed-in view of the two BT sextets used to analyse the magnetic structure in (a). 66
Figure 4.2: Room temperature ^{57}Fe emission Mössbauer spectra obtained after implantation of ^{57}Mn* into GaN at emission angles of 0^o and 60^o relative to the sample *c*-axis. 66
Figure 4.3: ^{57}Fe Mössbauer spectra simulated with Blume-Tjon model using hyperfine field of ±50 T at relaxation time indicated. 68
Figure 4.4: ^{57}Fe emission Mössbauer spectra obtained after implantation of ^{57}Mn* into GaN at the temperatures indicated and θ_γ = 60^o. 70
Figure 4.5: Temperature dependence of isomer shifts observed in the Mössbauer spectra for Fe implanted GaN. 73
Figure 4.6: Temperature dependence of the quadrupole splitting for Fe_C observed in the Mössbauer spectra for Fe implanted GaN. 74
Figure 4.7: Two Blume-Tjon sextets and their sum, Fe_{Mag}, (in blue) shown in the central region of the emission Mössbauer spectra of ^{57}Mn* implanted GaN at temperatures indicated. 75
Figure 4.8: The temperature dependence of the spin-lattice relaxation rate of the Fe^{3+} paramagnetic state in GaN. 76
Figure 4.9: A plot of relaxation rates as a function of temperature obtained for GaN compared with data from previous studies of oxides. 76
Figure 4.10: Areal fractions of spectral components as a function of temperature, observed in the Mössbauer spectra after implantation of ^{57}Mn* into GaN. 77
Figure 4.11: ^{57}Fe emission Mössbauer spectra obtained at 306 K after implantation of ^{57}Mn* into AlN at emission angles indicated. 79

Figure 4.12: ^{57}Fe Mössbauer spectra obtained after ^{57}Mn* implantation into AlN held at the temperatures indicated and $\theta_\gamma = 60^o$. 80
Figure 4.13: Temperature dependence of the isomer shifts for Fe_C and Fe_S observed in the Mössbauer spectra for Fe implanted AlN. 82
Figure 4.14: Temperature dependence of the quadrupole splitting for Fe_C observed in the Mössbauer spectra for Fe implanted AlN compared with GaN….. 83
Figure 4.15: Two Blume-Tjon sextets (and their sum) showing the magnetic structure fitted for Fe implanted AlN spectra at the temperatures indicated. 84
Figure 4.16: A comparison of relaxation rate trends of GaN and AlN with previously studied oxides. 85
Figure 4.17: Areal fractions of spectral components as a function of temperature, observed in the Mössbauer spectra for AlN after ^{57}Mn* implantation…… 86
Figure 4.18: ^{57}Fe emission Mössbauer spectrum obtained at 310 K for InN after implantation of ^{57}Mn* at $\theta_\gamma = 60^o$. 88
Figure 4.19: ^{57}Fe emission Mössbauer spectra obtained after implantation of ^{57}Mn* into InN at 304 K at and emission angles indicated. 89
Figure 4.20: ^{57}Fe emission Mössbauer spectra obtained after implantation of ^{57}Mn* into InN at the temperatures indicated and $\theta_\gamma = 60^o$. 90
Figure 4.21: Temperature dependence of the isomer shifts observed in the Mössbauer spectra for ^{57}Mn* implanted InN. 91
Figure 4.22: Temperature dependence of the quadrupole splitting for Fe_C observed in the Mössbauer spectra for ^{57}Mn* implanted III-nitrides. 91
Figure 4.23: Areal fractions of spectral components as a function of temperature as determined from the Mössbauer spectra of InN following ^{57}Mn* implantation. 92
Figure 4.24: Room temperature (305 K) emission Mössbauer spectrum obtained after implantation of ^{57}Mn* into virgin ZnO. Fe_{Mag} (Fe^{3+}) represents the sum of the five BT sextets. 96
Figure 4.25: ^{57}Fe emission Mössbauer Spectra for ZnO pre-implanted with ^{56}Fe at indicated fluences. 99
Figure 4.26: A plot of E_0 values as a function of fluence compared with other Mössbauer measurements. 102

Figure 4.27: Fluence dependence of the area fraction of Fe^{3+} at room temperature. 102
Figure 4.28: Area fractions of the spectral components obtained from the analysis of the ZnO sample pre-implanted with 8×10^{13} ions/cm^2 of ^{56}Fe. 103
Figure 4.29: Area fractions of spectral components obtained from the analysis of the ZnO sample pre-implanted with 5×10^{13} ions/cm^2 of ^{56}Fe. 104
Figure 4.30: Relaxation rates of the pre-implanted ZnO samples as a function of indicated fluence compared with trends in virgin ZnO and α-Al_2O_3..... 105
Figure 4.31: CEMS spectra for as-implanted ZnO:^{57}Fe+^{56}Fe sample and after annealing at 773 K..... 107
Figure 4.32: CEMS spectra for ZnO:^{57}Fe+^{56}Fe obtained after annealing at 973 K and 1173 K. 109
Figure 4.33: Magnetisation curves for the virgin ZnO sample measured at temperatures of 4 K and 293 K and fitted with 7th and 9th order polynomials, respectively. 112
Figure 4.34: Magnetisation curves of ZnO:^{57}Fe+^{56}Fe measured at 4 K and 293 K after annealing at 973 K. 112
Figure 4.35: Room temperature CEMS spectra for the as-implanted ZnO:^{57}Fe+^{59}Co sample and after annealing at 773 K and 973 K. 113

Figure A.1: Diamagnetism: (a) Crystalline and (b) amorphous lattice showing atoms without net magnetic moments, (c) Temperature dependence of susceptibility and (d) Field dependence of magnetisation of a diamagnetic material. 125
Figure A.2: Paramagnetism: Spin lattice arrangements in (a) crystalline and (b) amorphous structures showing spins randomly oriented, (c) Temperature dependence of χ^{-1} (d) $M(H)$ curve at different temperatures. 125
Figure A.3: Ferrimagnetism: (a) Spin lattice arrangement, (b) Temperature dependence of χ^{-1}, (c) Variation of spontaneous magnetisation with temperature, (d) $M(H)$ curve at different temperatures. 126

Figure A.4: (a) Neighbouring moments in a ferromagnetic material, (b) Parallel alignment of neighbouring spins in different magnetic domains, (c) Overall spontaneous magnetisation in magnetic domains. 127
Figure A.5: Magnetisation curve for a ferromagnetic material, showing hysteresis loop and arrangement of magnetic domains. 128
Figure A.6: Ferromagnetism: (a) Temperature dependence of χ^{-1}, (b) Variation of spontaneous magnetisation with temperature, (c) $M(H)$ curve at different temperatures in a ferromagnetic material. 128
Figure A.7: (a) Spin lattice arrangements in an antiferromagnetic material (b) Temperature dependence of χ^{-1} (c) $M(H)$ curve at different temperatures. 129
Figure A.8: Schematic illustration of the electronic density of states in (a) A ferromagnetic metal and (b) A normal metal. 130

Figure B.1: Typical emission Mössbauer spectrum for FeAl sample with a signal to background ratio ~20. 132
Figure B.2: FeAl emission Mössbauer spectrum illustrating spectral parameters. 132
Figure B.3: Curves of optimisation parameters obtain as a function of acetone vapour pressure and bias voltage at plate separation distances indicated. 134
Figure B.4: $^{57}Mn^{*}$ emission Mössbauer spectra for AlN obtained with FeAl and stainless steel detectors respectively. 136

List of Tables

Table 1.1:Selected properties for group III-nitrides and ZnO..... 6
Table 3.1:Details of samples used in this study. 45
Table 3.2:Simulation results from $^{57}Mn^{*}$ in III-nitrides and ZnO..... 49
Table 3.3:List of samples prepared by ion implantation and measurements conducted. 64
Table 4.1:Room temperature hyperfine parameters obtained for Fe implanted in GaN. 71
Table 4.2:Hyperfine parameters for Fe implanted in AlN obtained at room temperature..... 81
Table 4.3:Hyperfine parameters extracted from the analysis of the InN spectrum recorded at 310 K. 89
Table 4.4:Hyperfine parameters extracted from the analysis of the virgin ZnO spectrum measured at room temperature. 97
Table 4.5:Room temperature hyperfine parameters extracted for ZnO pre-implanted with ^{56}Fe at indicated fluences. 100
Table 4.6: Hyperfine parameters, Gaussian broadening and area fractions of fitted spectral components for the as-implanted ZnO:^{57}Fe+^{56}Fe sample and after annealing at 773 K. 108
Table 4.7: Hyperfine parameters, Gaussian broadening and area fractions of the fitted spectral components for the ZnO:^{57}Fe+^{56}Fe sample after annealing at 973 K and 1173 K. 109
Table 4.8: Hyperfine parameters, Gaussian broadening and area fractions of the fitted spectral components for the ZnO:^{57}Fe+^{59}Co sample. 114

Introduction

Semiconductors have been at the core of most technological developments in the electronic industry since the discovery of the first *transistor* [1,2] in 1947. Currently assembled in millions on a single *integrated circuit* (IC) or *microchip*, transistors are the key active components mainly utilised as *amplifiers* and *switches*.

The entire semiconductor industry relies on intentionally incorporating impurity or foreign atoms in order to improve existing materials and also to tailor-make their properties to specific applications. The inter-atomic bonding mechanism between valence electrons and the resulting atomic arrangement influence the electrical, optical, photonic and magnetic properties of semiconducting materials.

In electronic devices, the electron charge is solely responsible for the functionality and behaviour of semiconducting materials. Over the past few decades, intensive research spawned to extend functionality of established solid state devices by use of the electron spin in addition to its charge. A new era started in the late 1980s with the discovery of the *giant magnetoresistance* (GMR) effect by independent groups led by A. Fert [3] and P. Grünberg [4]. In 2007, these researchers shared the Nobel Prize in Physics for this discovery. The GMR effect is observed as a significant change in electrical resistance in *spin-valves* (thin films comprising of alternating ferromagnetic and non-magnetic layers), depending on whether the magnetisation of ferromagnetic layers are aligned in parallel or anti-parallel [3,4,5]. The former alignment results in low resistance whilst the latter yields high resistance. This gave birth to a new field of research known as "*spin electronics*" which is commonly referred to as "*spintronics*" [6]. Spintronics exploits how the mobility of electrons in a ferromagnetic material is influenced by the spin and its associated magnetic moment. The success of the discovery was first published in *The Wall Street Journal* [7] when IBM announced news of actual *read heads* for *magnetic hard drives* using the GMR effect not just 'proof of concept' devices. However, the performance of spin-valve devices was exceeded and replaced by *magnetic tunnel junctions* (MTJs) based on the tunnelling magnetoresistance (TMR) effect. Non-volatile magnetic random-access memory (MRAM) devices were the first 'fruits'

of this modification. Solid state devices based on GMR and TMR effects have similar sandwich structures; however, insulating non-magnetic layers are utilised in MTJs in place of non-magnetic conductive layers. In addition to non-volatility, spintronic devices have shown to have high processing speeds, increased storage capacity, and power efficient [8] compared to conventional electronic devices.

The advantages of spintronic devices based on the magnetoresistance effect have been highlighted, but, in these devices, *semiconductor materials* are used for *information processing* while *metallic magnetic materials* are used for *data storage*. The main goal in spintronics is to design a system encompassing semiconducting and ferromagnetic properties in one material. This is bound to extend functionality and be cost effective by reducing processing time and energy costs. However, semiconductor materials such as Si, GaN, and ZnO are not magnetic while ferromagnetic materials such as Fe, Co and Ni are not semiconductors. Moreover, semiconductors and metals have different crystal structures and conductivity mismatch that will hinder functionality of the resulting heterostructures and lower effective spin-injection [9]. On the other hand, both ferromagnetic and semiconducting properties are known to coexist in chromium spinels [10,11] and europium chalcogenides [12]. Nevertheless, such magnetic semiconductors have *Curie temperatures* (T_c) far below room temperature (RT) (T_c < 100 K), which limits their practical application in spintronic devices. Furthermore, the magnetoresistance effect (in both GMR and TMR) is a semi-classical phenomenon [13,14,15] which stems from combined spin-dependent scattering [16,17] experienced by electrons at interfaces and in bulk layers. As a result, the quantum nature of individual electron spin and its control have not been fully exploited.

An attractive alternative is the modification of existing semiconductor materials by incorporating magnetic metallic dopants or impurities to realise *dilute magnetic semiconductors* (DMS). A DMS material is one in which a small fraction of the host cations are substititutionally replaced by magnetic ions either from transition metals (TM) or rare earth (RE) elements [18]. Current microelectronic devices are semiconductor based; hence magnetic semiconductors would be compatible with existing IC technology. Moreover, in contrast to metals, semiconductors have the

ability to amplify electrical as well as optical signals, thus creating more possibilities for data processing. Transition metal doped non-magnetic semiconductors, mainly oxides and nitrides have attracted much attention since theoretical predictions that these materials could exhibit ferromagnetic behaviour at and above room temperature resulting from carrier-mediated magnetic interactions [19]. Research in this field has been progressing on two fronts:

a) In wide band gap semiconducting materials such as ZnO and GaN doped with 3*d* metals:

   There exist several review reports of such systems in both GaN and ZnO [20,21,22,23]. TM doped wide band gap semiconductors have been shown to exhibit different forms of magnetism, while the origin of the observed magnetic effects is still under debate [24,25,26,27]. A detailed summary of the published theoretical and experimental work will be given under the literature survey section in chapter 1.

b) In narrow gap semiconductors, for example GaAs doped with Mn:

   Carrier mediated ferromagnetic behaviour has been observed in GaAs doped with Mn, but still with a Curie temperature below room temperature. In 1996, Ohno *et al*. [28] first reported a T_c of 110 K, but more recently in 2008, Wang *et al.* [29], determined T_c for this system to be ~185 K. The larger T_c is attributed to the progress in tuning the quality of material during growth. In (Ga,Mn)As, Mn ions on Ga substitutional sites act as acceptors and the resulting itinerant holes mediate ferromagnetic coupling between the localised Mn magnetic spins [19]. This system could provide fundamental insight if the mechanism can be realised in other DMS materials.

The search for a fundamental understanding of the origin and nature of magnetism in dilute semiconductors continues motivated by the possibility of potential technological applications in spintronics. The projects presented in this thesis seek to contribute to this search, and focus on studies of magnetism in: (a) ^{57}Fe implanted III-nitrides (GaN, InN and AlN) and (b) ^{57}Fe, ^{56}Fe and ^{59}Co implanted ZnO. ^{57}Fe Mössbauer spectroscopy was applied using the following approaches; (a) emission

Mössbauer spectroscopy (eMS) using the short-lived radioactive isotope, $^{57}Mn^{*}$ with a half-life, $t_{1/2}$ = 1.5 min, as a precursor and (b) conversion electron Mössbauer spectroscopy (CEMS) using implantation of stable ^{57}Fe isotope and a conventional $^{57}Co^{*}$ source. In addition, vibrating sample magnetometer (VSM) was utilised to give magnetisation information about the samples under study. Mössbauer spectroscopy has been selected as the main research tool because of its extreme sensitivity to both the bonding mechanism and the local environment in the vicinity of the probe atoms.

Overview of thesis

Chapter 1 focuses on the properties of materials under study and a literature survey on structural, electronic and magnetic behaviour of transition metal doped semiconductors. Moreover, the theory behind paramagnetic spin-flip mechanisms is presented in this chapter while the introductory concepts on magnetism and the different classes are given in ***Appendix A***. Lastly, chapter 1 outlines the aims and objectives of the research project guided by the literature review and the identified research gaps. In ***Chapter 2*** the theory of the Mössbauer effect and the related hyperfine parameters are discussed. ***Chapter 3*** gives a brief description of material modification by ion implantation and introduces the experimental techniques employed in this study (eMS, CEMS and VSM). The analysis of data obtained from eMS, CEMS and VSM measurements on nitrides and ZnO samples, and the interpretation of results are presented and discussed in ***chapter 4***, which concludes with an overview of the main findings. ***Chapter 5*** presents an outlook from the main conclusions and recommendations for further studies. The details of the development of a new parallel plate detector based on an FeAl electrode and preliminary test measurements are reported and discussed in ***Appendix B***.

Chapter 1

Fundamental Concepts and Literature Review

III-nitrides, ZnO and their alloys form a unique class of semiconducting materials with extraordinary qualities in terms of their crystal structure, optical properties, and electrical properties among others. These novel qualities have made them useful in a wide range of applications in optoelectronic and high-frequency devices such as light emitting diodes (LEDs), laser diodes, and monolithic microwave integrated circuits (MMICs) and high power field effect transistors (FETs) for satellite and terrestrial communication [30,31,32,33]. Their functionality as semiconducting materials is greatly influenced by the presence of intrinsic or extrinsic defects created either during growth or doping processes. Recently, these materials, mainly ZnO and GaN have attracted much attention following the prediction of their potential application in spintronic devices when doped with transition metals [19,34].

A summary of relevant properties of III-nitrides and ZnO materials is given in this chapter. In addition, a brief discussion of different types of point defects is included since their nature and lattice site location is vital for understanding new properties in doped semiconducting materials. Moreover, a literature survey of transition metals in nitrides and ZnO is presented and the chapter concludes with an outline of the aims and specific objectives of the projects undertaken.

1.1. Properties of III-nitrides and ZnO

Group III-nitrides and ZnO are thermodynamically stable in the wurtzite structure for bulk materials under ambient conditions but may also be found in zinc-blende and rock salt structure under different conditions. In the wurtzite structure, ZnO, AlN, GaN and InN have a C^4_{6v} - $P6_3mc$ space group symmetry, where each atom is tetrahedrally bonded to four nearest neighbours (and vice versa) resulting from sp^3 hybridisation, typical of covalent bonding, however, these materials have partial ionic character, especially ZnO is more ionic than covalent. Figure 1.1 (a) and (b) depicts 2×2 unit cells and a unit cell, respectively for typical configuration of atoms

in a wurtzite structure, exemplified by GaN, while Figure 1.1 (c) shows the view along the *c*-axis.

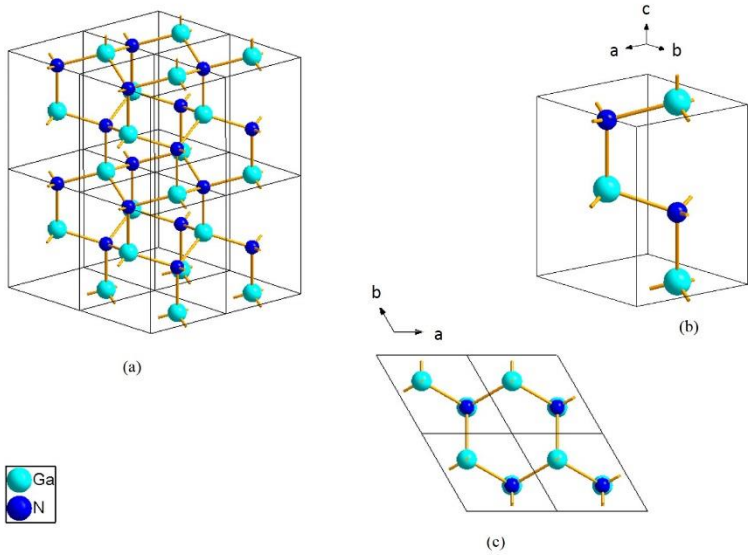


Figure 1.1: Wurtzite crystal structure of GaN: (a) 2×2 unit cells, (b) unit cell and (c) view along the *c*-axis.

A list of selected properties for AlN, GaN, AlN and ZnO measured at room temperature is presented in Table 1.1.

Table 1.1: Selected properties for group III-nitrides and ZnO.

Property	AlN	GaN	InN	ZnO
Density (g.cm^{-3})	3.257 [35]	6.15 [36,37]	6.81-6.98 [38]	5.607 [39]
Debye Temperature (K)	980 [40], 991 [41]	820 [42], 673 [41]	660 [43], 444 [41]	440 [44]
Melting Point (K)	3273 [31]	2773 [45]	1373 [31]	2242 [46]
Bond length (Å)	1.86 [47]	1.94 [47]	~2.12 [48]	1.97 [46]
Band Gap (eV)	6.23 [49]	3.51 [49], 3.42 [50]	0.7-1.0 [51,52,53,54,55,56,57]	3.4 [58]
Phillips Ionicity [59]	0.449	0.500	0.578	0.616

The relatively high Debye temperature, melting point, and shorter bond length in AlN suggests that the Al-N bonds are stronger than to Ga-N and In-N bonds. The bond strength decreases as one descends group III of the Periodic Table. In addition, the nitrides and ZnO have partially ionic and partially covalent bonds, which are defined by their respective Phillips' ionicity values. Interestingly, GaN and ZnO have similar melting points, bond lengths, band gaps and densities. However, the Debye temperature for GaN is higher than that for ZnO, suggesting that Ga-N bonds are stronger than Zn-O bonds in the respective materials. Furthermore, the Phillips

ionicity for ZnO is slightly greater than for GaN, indicating that ZnO is more ionic than GaN. These similarities and differences are expected to influence their behaviour as semiconducting materials.

1.2. Point defects

Crystalline materials have a periodic arrangement of atoms in their lattice structure and deviation from this regular atomic structure results in crystal defects known as *point defects*. These *point defects* can manifest as a missing atom from a regular lattice site (vacancy), atoms in incorrect lattice sites (antisite/substitutional impurity defects) or an atom in an open space between two ordinary lattice host atoms (interstitial defect). Impurity atoms can also be incorporated in other defect structures resulting in substitutional or interstitial-vacancy complexes. The different types of point defects are shown in Figure 1.2.

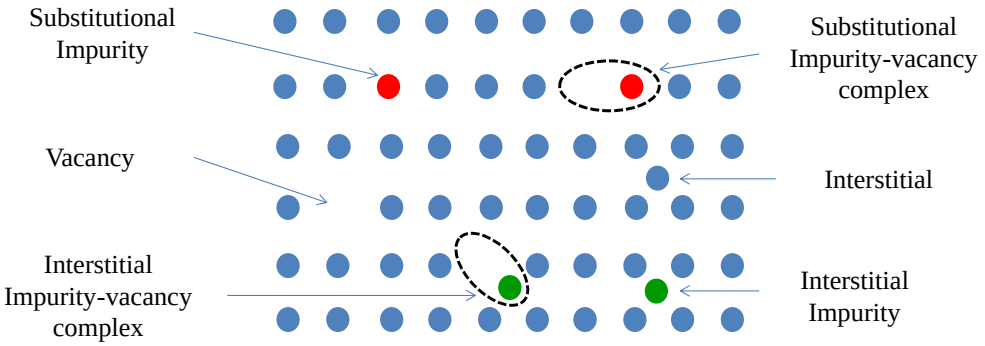


Figure 1.2: A schematic illustration of different types of point defects.

1.3. Literature survey

In this section, a number of published reports on transition metal doped III-nitrides and ZnO semiconductors will be reviewed and have been categorised into sub-sections highlighting information on ion-solid interactions.

1.3.1. Displacement energies

The ion implantation process involves collisions between ions and target atoms resulting in slowing down of the ions and loss of energy through nuclear and electronic stopping [60]. An important property in determining the nature of the defect and/or damage formation created by the implantation process in host materials is the threshold displacement energy (E_d) i.e. the minimum kinetic energy

required to permanently remove the host atom from its lattice site upon impact resulting in a stable defect. Depending on the initial kinetic energy transferred from the incident ions to the target atoms, the primary knock-on atoms may in turn further displace other host atoms resulting in several atomic collision cascades. Subsequently, this may lead to a distribution of vacancies, interstitials and/or various types of defects. However, if the kinetic energy imparted to the host atoms is less than E_d, the energy is transferred to lattice vibrations and distributed as heat among the surrounding atoms.

A. Displacement energies in III-Nitrides

Different E_d values have been reported in the literature for nitrides, mainly GaN and AlN, from both theoretical calculations [61,62,63,64] and experimental work [65,66]. In 1977, Desnica *et al.* [61] applied Van Vechten's theory [67] to determine the displacement energy in GaN for Ga atoms of E_d(Ga) to be 25.5 eV. The theory utilises the sum of vacancy formation, interstitial formation and lattice distortion energies. On the other hand, Van Vechten [67] reported values of E_d(Ga) = 24.3 eV and E_d(N) = 32.5 eV while molecular dynamics simulations performed by Nord *et al.* [63] suggest that the smallest displacement energies are E_d(Ga) = 18.8 eV and E_d(N) = 22 eV for Ga and N, respectively. Furthermore, these authors found that the average values calculated over all angles results in higher values of E_d(Ga) = 45±1 eV and E_d(N) = 109±2 eV. These results suggest that more energy is required to displace N atoms than Ga atoms. On the contrary, Xiao *et al.* [64] recently presented molecular dynamics simulations for five main crystallographic directions in GaN and estimated higher average values of E_d(Ga) = 73.2 eV compared to E_d(N) = 32.4 eV. In 1997, Look *et al.* [65] studied transport properties of electron irradiated GaN films and showed that E_d(Ga) is 20.5 eV and E_d(N) is 10.8 eV. Electron irradiation studies by Ionascut-Nedelcescu and co-authors [66] in 2002 monitored the changes in luminescence of GaN LEDs as a function irradiation energies (300-1400 keV) and found a displacement energy of E_d(Ga) = 19 eV resulting from a threshold irradiation energy of 440 keV. The authors did not observe any displacement of N atoms and concluded that the nitrogen sublattice repairs itself through room temperature annealing.

In 1977, Van Vechten [62] employed a semi-empirical analysis from which displacement energies of E_d(Al) = 27 eV and E_d(N) = 35 eV were obtained for AlN. Recently, Wendler [68] estimated values of E_d(Al) = 42 eV and E_d(N) = 35 eV in AlN using cross section of damage formation per ion obtained from Rutherford backscattering spectrometry (RBS) in channelling mode (RBS/C) and values calculated using SRIM [69].

There are very few reports and limited information on average displacement energies in InN. Jones [70] applied SRIM calculations and determined mean threshold displacement energies of 15 eV for both In and N in InN.

B. Displacement energies in ZnO

Similar to GaN, there is a wide range of displacement values reported for both atoms in ZnO. In a review article on the properties of ZnO, Zinkle and Kinoshita [71] reported displacement energies of 47-55 eV for the O sublattice and 40-70 eV for the Zn sublattice. Lorenz *et al*. [72], performed RBS/C studies in ZnO implanted with N, Ar and Er ions and obtained a maximum displacement energy of E_d(Zn) = 65 eV for the (0001) oriented ZnO which is in good agreement with the results reported by Zinkle and Kinoshita. However, earlier thermodynamic calculations by Van Vechten [67] show very small displacement value of E_d(Zn) = 18.5 eV and an E_d(O) = 41.4 eV, while Locker and Meese [73] obtained a threshold displacement energy of 57 eV for both sublattices. On the other hand, cathodoluminescence (CL) studies following electron irradiation by Pazionis and Schulz [74] resulted in a calculated value of E_d(Zn) = 56 eV. Moreover, simulations presented by Erhart *et al*. [75], give an E_d(Zn) of 45 eV along the *c*-axis and 42 eV for all directions.

1.3.2. Defects, radiation damage and annealing processes

A. Structural characterisation of dopants in III-Nitrides

Several investigations [76,77,78,79,80,81,82] have been conducted to monitor radiation induced damage, defects formed and annealing behaviour of ion implantation, especially in GaN and AlN using different dopants. A number of studies [76,78,79] attest to the radiation hardness of GaN and AlN, which may be attributed to the dynamic annealing during the irradiation and/or implantation processes coupled

with strong interatomic bonds in these materials. In 1996, Tan *et al.* [76] applied 90 keV Si implantation in GaN and found a critical amorphisation fluence of 2.4×10^{16} ions/cm^2 while 5×10^{16} ions/cm^2 of Ca^+ and Ar^+ ions implanted in GaN was reported by Liu *et al.* [77] in 1997. Further studies by Liu *et al.* [80] using 1×10^{16} ions/cm^2 of Fe^+ implantation in GaN confirmed resistance to amorphisation. In AlN, amorphisation was observed by Lorenz *et al.* [79] after implantation of 300 keV Eu ions to fluences as high as 1.4×10^{17} ions/cm^2. The authors recommended channelled implantation to lower the damage formed, and observed that the induced damage is stable up to temperatures of ~1573 K. In the case of InN, a few reports on ion implantation are available. Lacroix and co-authors [83] have observed high sensitivity to damage formation after 300 keV low fluence implantation (5×10^{12} ions/cm^2) of Eu atoms. Nitrogen depletion was observed after annealing at 823K [84], and also during elastic recoil detection analysis (ERDA) [85], from ion implantation and irradiation [86,87] studies. Lacroix *et al.* [83], suggested that the damage formation is stimulated by the formation of a dense network of extended defects and also observed that fluences in the range $10^{15\text{-}17}$ ions/cm^2 are responsible for the breakdown of the wurtzite crystal structure in both GaN and AlN compared to InN [83].

A review of positron annihilation investigations in III-nitrides by Tuomisto [88] points to III-sublattice vacancies as the predominant defects in these materials and also observed N vacancies (V_N). On the contrary, density functional theory (DFT) [89] calculations indicated that nitrogen vacancies as the dominant native defects in GaN. However, Doppler broadening spectra and positron lifetime measurements for Si^+, O^+ and Be^+ performed by Uedono *et al.* [90] suggested the presence of complexes in the form of $V_{Ga}V_N$'s divacancies in addition to gallium vacancies (V_{Ga}). Upon annealing at 673 K, these authors observed the agglomeration of defects which they attributed to the mobility and dissociation of V_{Ga}'s and $V_{Ga}V_N$'s. On the other hand, Saarinen *et al.* [91,92], reported that Ga vacancies created by 2 MeV electron irradiation recovered upon annealing in the temperature range of ~500-700 K, while Uedono *et al.* [90] suggested that heat treatments around 1173 K suppresses the clustering of these defects and aided the annealing of implantation induced defects.

In addition, Lee *et al.* [93] performed a number of structural characterisation measurements on GaN films, after implantation of 5×10^{16} ions/cm^2 of Co, Cr and V ions with an energy of 250 keV at 623 K and subsequent annealing. The authors utilised X-ray diffraction (XRD), selective area diffraction pattern (SADP) and transmission electron microscopy (TEM) and found that the implantation induced damage was in the form of defects and dislocation loops. No secondary phase formation even within the detectable limits of the characterisation techniques was observed and the authors were unable to specify the type of defects. Kim *et al.* [94] applied high resolution-XRD, SADP and TEM on GaN implanted with 3×10^{16} ions/cm^2 of Co ions and confirmed the absence of any peaks associated with secondary phase formation. Although the secondary phases were not observed, both research groups did not completely eliminate the notion of the existence of cluster formation and the contribution of the implanted ions to magnetism in GaN. However, additional X-ray photoelectron spectroscopy (XPS) depth measurements by Kim *et al.* [95] revealed the presence of Co or CoGa magnetic clusters. Further studies by Talut *et al.* [96] showed α-Fe nanocluster formation in GaN implanted with 200 keV ^{57}Fe ions at 623 K for ion fluences between 4×10^{16} and 1.6×10^{17} ions/cm^2 after annealing between 973 K and 1123 K. The Fe cluster sizes depended on ion fluence and annealing temperatures.

B. Defects in ZnO

A number of Raman spectroscopy studies of virgin and doped ZnO layers grown by different techniques have reported [97,98,99] anomalous Raman modes, most of which could be explained by the presence of local vibrational modes of impurities or defects, specifically N local defects. Similar modes located at around 277, 511, 583 and 644 cm^{-1} were detected for Sb Al, and Fe doped ZnO films intentionally grown without N. The mode at 277 cm^{-1} was also present in Ga doped ZnO [100]. Since these modes have no direct relation to N incorporation, their origin was suggested to be as a result of host lattice defects. Moreover, additional modes at 720, 631 and 531 cm^{-1} were observed in Fe, Ga, and Sb dopants, respectively, while Li doped ZnO did not reveal any additional modes. Manjón *et al.* [101], also argued that most of these observed modes are associated with silent modes due to the breakdown of the translational crystal symmetry induced by the defects and

dopants. These authors also observed similar modes in nitride films and alloys. The Raman spectrum for ZnO implanted with 8×10^{16} ions/cm^2 (~16.92 at %) of Fe^+ ions at 80 keV exhibits the E_2 (high), A_1(LO) and $2E_2$(M) modes which suggests that the Fe ions are incorporated in Zn substitutional positions in ZnO. This non-covalent substitution of Fe on Zn lattice sites act as acceptors and provide localised spins, which play a key role in ferromagnetism [102]. However, ZnO implanted with Mn at an energy of 220 keV with different fluences (10^{15}-10^{17} ions/cm^2), gave a mode at around 230 cm^{-1} and was found in all implanted samples. This mode was assigned to radiation induced damage of the ZnO crystal structure [103]. A second mode observed at 523 cm^{-1} was attributed to Zn-related vibrations due to Mn incorporation. Theoretical calculations [103] reveal that this mode is due to the vibration of Zn atoms surrounded by its first nearest neighbour O atoms, being partially replaced by Mn atoms in the ZnO crystal lattice.

1.3.3. Site location and charge states of dopant ions

A. Lattice site location and charge states of TM ions in III-Nitrides

In 2001, Alves *et al.* [104] performed a transmission Mössbauer study of GaN implanted with 150 keV Fe ions with fluence of 1×10^{16} ions/cm^2. The spectrum of the as-implanted sample was dominated by a doublet (~90%) with hyperfine parameters of δ = 0.12 mm/s and ΔE_Q = 0.52 mm/s; and a single line with δ = -0.17mm/s. The single line was attributed to paramagnetic Fe clusters and the doublet assigned to the majority of Fe ions occupying Ga sites. No clear assignment of any implanted ions in damaged regions was reported by the authors. After annealing in flowing N_2 at 923 K for 15 min and 1273 K for 2 min, 100% of the Fe atoms were found to be located on substitutional Ga sites [80,104]. This conclusion was supported by their RBS measurements in channelling configuration (RBS/C) and proton induced X-ray emission (PIXE) measurements, which also confirmed the lattice recovery of the induced damage in the implanted sample. These observations were confirmed by emission channelling (EC) measurements by Wahl *et al.* [105] on GaN samples implanted with 60 keV ^{59}Fe ions at room-temperature with a fluence of 1×10^{13} ions/cm^2. Their results provided direct evidence that 80% of the implanted Fe atoms in the as-implanted sample were incorporated on substitutional sites whilst the remainder were located on “random” sites [105].

Annealing the sample up to 1173 K resulted in no change in the substitutional fraction. Similar measurements on rare earth [106] elements in III-nitrides introduced by ion implantation or *in-situ* doping with molecular beam epitaxy (MBE), showed that all the RE ions did not occupy the perfect substitutional site but were displaced around this site and a small fraction of the ions were located in the so-called "random" sites. Further EC and perturbed angular correlation (PAC) studies of heavy (^{111}In and ^{89}Sr) and light (^{8}Li and ^{24}Na) radioactive ions implanted in GaN and AlN were reported by Ronning *et al.* [107]. The EC results showed that the heavy ions mainly occupied substitutional III sub-lattice sites directly upon room temperature implantation, no significant change was observed after annealing up to 1073 K. The light ions mainly occupied interstitial sites at room temperature. Even though implantation induced damage could be completely annealed at high temperatures (T~1073 K), the authors did not rule out the presence of point defects. Diffusion and occupation of interstitial sites by Li ions were observed in GaN and AlN for implantations performed above 700 K. However, after annealing for 10 minutes at 1073 K, Na ions showed a lattice site change to substitutional sites in AlN but not in GaN. In 2006, Dhara *et al.* [108] conducted systematic PIXE measurements on 400 keV Co implanted GaN samples (with concentrations of 5, 8, and 11 at. %) at 620 K after subsequent annealing for 7 minutes in ultrahigh pure N_2 at 700ºC and found that Co atoms were located on Ga lattice sites.

Conversion electron Mössbauer spectroscopy (CEMS) measurements of Fe implanted AlN with high fluences ranging from 7×10^{16} at./cm^2 to 2×10^{17} at./cm^2 were reported by Borowski *et al.* [109]. The spectrum for the as-implanted sample (6×10^{16} Fe at./cm^2) was analysed with a single line S (δ = -0.22 mm/s) and two doublets, D_1 (δ = 0.56 mm/s, ΔE_Q = 0.68 mm/s) and D_2 (δ = 1.03 mm/s, ΔE_Q = 1.08 mm/s) attributed to isolated Fe^{3+} with three and four nearest N neighbours, respectively.

CEMS studies of ^{57}Fe implanted GaN at different temperatures with fluence between 1×10^{16} and 1×10^{17} ions/cm^2 were published by Talut *et al.* [96,110,111]. The authors adapted a similar analysis model employed by Borowski *et al.* [109] for AlN. Their spectrum was characterised by a single line (δ = -0.05 mm/s) and two doublets; D_{III} (δ = 0.42 mm/s, ΔE_Q = 0.48 mm/s) and D_{IV} (δ = 0.59 mm/s,

ΔE_Q = 0.71 mm/s). The single line was assigned to either superparamagnetic α-Fe or to paramagnetic γ-Fe, while the doublets were assigned/attributed to Fe^{3+} with three and four nearest N neighbours, respectively. The authors reported that approximately 24% of the Fe atoms were found in substitutional Ga sites (D_{IV}) and the remainder distributed either on interstitial locations or as small precipitates. In GaN the spectral components D_{IV} and D_2 disappeared after annealing at 1123 K while in AlN this effect occurred at 1073 K. In AlN, small increases in the population of both S and D_1 were observed after annealing at 1073 K, while in GaN a very strong magnetic signal assigned to ferromagnetic α-Fe dominated the spectra (~86%) after annealing at 1123 K.

RBS/C results presented by Lorenz *et al.* [112] showed that implanted Hf atoms in AlN occupied Al substitutional sites. Recently, Miranda *et al.* [113,114] and Kessler *et al.* [115], reported on investigations of Cd and Ag implanted AlN and GaN, respectively with fluences ranging from 1×10^{13} at./cm^2 to 1.7×10^{15} at./cm^2 with 150 keV ion energy using RBS/C, HR-XRD and PAC. The authors observed the incorporation of Cd on substitutional III sites in both materials, while Ag is slightly displaced from a substitutional site. The implantation induced damage is partially removed for high fluences while the lattice is fully recovered for lower fluences after annealing at 1223 K in flowing nitrogen.

B. Lattice site location and charge states of TM ions in ZnO

Potzger *et al.* [116] reported CEMS measurements after implantation of ^{57}Fe with an energy of 180 keV at an angle of 7° into a ZnO single crystal held at 623 K to a fluence of 4×10^{16} cm^{-2}. The spectrum obtained at room temperature was analysed with four spectral components; a single line with δ = 0.53 mm/s, two quadrupole split doublets, an inner doublet with parameters δ = 0.69 mm/s and ΔE_Q = 0.6 mm/s, and an outer doublet with parameters δ = 0.78 mm/s and ΔE_Q = 1.3 mm/s and a magnetic sextet assigned to α-Fe metallic nanoparticles. The single line was assigned to Fe^{3+} while the two doublets were attributed to Fe^{2+}. Annealing the sample at 823 K for 15 minutes favoured the growth of Fe particles while increasing the temperature to 1023 K and annealing for 3.5 hours resulted in formation of $ZnFe_2O_4$ nanoparticles [117]. In a follow-up experiment [118], the formation of these

secondary phases was suppressed when the ZnO sample was annealed at 1273 K in O_2 or under high vacuum before implantation with Fe.

Monteiro *et al.* [119] conducted PIXE measurements on ZnO after implantation of ^{56}Fe with a fluence of up to 10^{16} ions/cm^2 at 100 keV and observed that ~56% of the Fe atoms in the as-implanted sample were located along the *c*-axis of ZnO which increased to ~73% after annealing at 1323 K. In addition, the same group also performed EC studies [120] on ZnO single crystals implanted at room temperature with 60 keV $^{59}Mn/^{59}Fe$ a fluence of 2×10^{13} ions/cm^2 and showed that approximately 95% of the Fe atoms occupied substitutional Zn sites with no evidence of Fe on substitutional O or interstitial sites.

1.3.4. Magnetism in transition metal doped ZnO and III-nitrides

Dietl and co-authors [19] suggested that DMS materials such as *p*-type GaN and ZnO doped with concentration in the order of 3×10^{20} cm^{-3} of Mn ions could exhibit Curie temperatures above room temperature. The ferromagnetic ordering among the spins of isolated Mn atoms is proposed to be mediated by itinerant holes. The theoretical calculations ignited a flurry of intense experimental search for TM doped metal oxides and III-nitrides as potential DMS's.

A. Magnetism in TM doped III-Nitrides

There have been several studies of magnetic behaviour in III-nitrides implanted with TM ions. Room temperature ferromagnetism (RTFM) has been reported in GaN samples implanted at 623 K with ^{57}Fe ions to fluences between 4×10^{16} and 1.6×10^{17} ions/cm^2 [96]. Ferromagnetic-like ordering was evident at 5 K and up to 320 K in Co and Cr implanted GaN samples, while paramagnetic behaviour was observed for Vanadium (V) implanted samples [93] over the whole temperature range. In contrast, Pereira and co-authors [121], reported strong antiferromagnetic interactions between Cr atoms implanted in GaN with concentrations up to 35%, while the uncompensated Cr atoms showed paramagnetic behaviour. GaN films implanted with 80 keV, 3×10^{16} ions/cm^2 of Co^- ions at 623 K and annealed at 973 K showed superparamagnetic features [94]. Kim *et al.* [95] conducted magnetisation measurements at 5 K, using a superconducting quantum interference device (SQUID) magnetometer and observed a distinct ferromagnetic

behaviour in Co implanted GaN but the effect disappeared at room temperature even within the resolution limits of the measurements. Bonanni *et al.* [122], performed electron paramagnetic resonance (EPR) and photoluminescence (PL) measurements on metalorganic chemical vapour deposition (MOCVD) grown GaN:Fe and found the existence of Fe in the isolated $3d^5$(Fe^{3+}) state. Furthermore, their SQUID measurements showed that in addition to Curie paramagnetism due to Fe^{3+}, a temperature independent contribution exists which the authors have tentatively attributed to van Vleck paramagnetism of Fe in the Fe^{2+} state.

The properties of AlN layer grown by MOCVD on sapphire implanted with 3×10^{16} ions/cm^2 of Co^+, Cr^+ and Mn^+ at 250 keV were reported by Frazier *et al.* [123]. AlN implanted with Co+ and Cr+ showed ferromagnetic ordering at 300 K after annealing at 1223 K for 2 minutes in N_2. The ferromagnetism was evidenced by the presence of a hysteresis loop in *M* versus *H* measurements while Mn^+ implanted samples showed distinct hysteresis loops up to ~100 K. The authors suggested that this contribution could be increased by annealing the sample to higher temperatures.

Belabbes *et al.* [124] carried out theoretical density functional studies of Cr doped InN and showed that ferromagnetism originates from the coupling between the Cr *d* and the N *p* states, while Xie *et al.* [125] claimed that virgin InN exhibits RTFM, with a Curie temperature of ~297 K originating from In vacancy defects.

B. Magnetic properties of TM doped ZnO

Ferromagnetic behaviour has been reported in ZnO implanted with Fe [116,117,118,126] and Co [127,128,129], and attributed to the presence of metallic nanoparticles/clusters and/or secondary phases. In Fe implanted ZnO, even though Fe is present in the Fe^{2+} and Fe^{3+} charge states, their separation distance is quite large and prohibits ferromagnetic coupling due to the lack of *p*-type carriers [130]. Matei *et al.* [131], have reported the observation of RTFM for electrochemically grown ZnO:Co with 5 at.% Co concentration. The origin of the ferromagnetism could not be established; however the authors suggested it could be related to Co_3O_4 complexes, Zn interstitials and/or oxygen vacancies. Similar results of intrinsic ferromagnetism in Co implanted ZnO were reported by Zhang and co-authors [132] but no ferromagnetism was observed with Fe-doped samples. Micro-Raman and XRD

studies of Mn, Ni, Co and Fe implanted ZnO with concentrations of 4-16 at.% were reported by Schumm *et al*. [133]. After annealing the samples with concentrations ≥ 8 at.%. at 973 K, the authors observed secondary phases of the form $ZnTM_xO_y$ for Mn and Co implantations and Zn-TM-O complexes for Mn and Fe.

Amidst the different findings concerning the origin and nature of magnetic behaviour in doped semiconductors, ferromagnetism has been reported based on hysteresis loops obtained from high sensitivity magnetometry measurements, however, careful handling of specimens was required. Pereira *et al.* [134], reported practical guidelines to eliminate contamination during sample preparation and handling prior to using such measurements, which could result in artificial ferromagnetic hysteresis loops.

1.3.5. Exchange interactions

Several mechanisms have been proposed to explain magnetism in TM doped semiconductors. In (Ga,Mn)As, Dietl *et al*. [19], proposed the mean-field Zener model to explain the predicted high T_c in this material. This model is a combination of the Zener model [135] for metals and the Ruderman-Kittel-Kasuya-Yosida (RKKY) interactions initially proposed by Ruderman and Kittel [136] and later extended separately by Kasuya [137] and Yosida [138]. In Zener's theory, the direct interaction between the *d* shells of TM atoms (*superexchange*) leads to antiferromagnetic coupling of the *d* shell spin for atoms with half-filled *d* shells. However, in the same system, ferromagnetic configuration is possible through *indirect coupling* of the spins because the conduction electrons tend to align the spins in the incomplete *d* shells. The RKKY interaction is based on the indirect coupling between the magnetic ion and the conduction electrons due to the Coulomb exchange, where the conduction electrons in the neighbourhood of the magnetic ion are polarized depending on the distance between interacting atoms [20]. As a result, this coupling may be ferromagnetic or anti-ferromagnetic depending on whether the magnetic moments are parallel or antiparallel, respectively.

The mean field Zener model accounts for the anisotropy of the carrier mediated exchange interaction linked with spin-orbit coupling in the semiconductor material. Moreover, to explain ferromagnetism in TM doped ZnO, Sato and Katayama-

Yoshida [34] proposed the *double exchange* mechanism, where the magnetic ion in different charge states couple by virtual hopping of extra electrons between ions through interaction with the *p*-orbitals.

In addition, ferromagnetic ordering in DMS materials has been explained by the formation of the *bound magnetic polaron* [139] (BMP). The BMPs result from the alignment of spins in many TM ions together with weakly bound carriers within a polaron radius [80]. The localised charge carriers (i.e. holes) in the polaron act on the impurity atoms in their vicinity producing an effective magnetic field which aligns all spins. Ferromagnetic ordering is evident when neighbouring magnetic polarons overlap and interact through magnetic dopants forming clusters of polarons comparable to the sample size.

Moreover, other studies suggested vacancy related magnetism [140,141,142]. However, the condition for, and the origin of, magnetism is not well understood. Coey *et al*. [143], suggested that the role of introducing transition-impurity atoms is to enable the local charge transfer required to bring the Fermi level up to a maximum in the density of states, and stimulate exchange splitting of the density of states. Thus, two different states of the cation should exist. In this scenario, the TM dopant atom acts as a charge reservoir from which electrons are transferred to local defect states. The authors proposed that different states exist at or near the particle surface, and that it is the capability of the TM impurity cations to exhibit mixed valence states as opposed to their possession of a localised moment that is central to magnetic effects. Furthermore, the free carrier behaviour is affected by the presence of magnetic ions through the *sp-d* exchange interaction between the spins of the itinerant carriers and the localised magnetic moments [20]. More importantly, for practical application in spintronics, the DMS material should show ferromagnetism with a T_c > RT. In addition, for some device applications, it is necessary that the magnetism be carrier mediated ferromagnetism, so that the magnetic properties of the DMS material can be controlled externally.

1.3.6. Overview of literature review

In this chapter, several aspects pertaining to the behaviour and properties of III-nitrides (AlN, GaN and InN) and ZnO semiconductors after doping by ion

implantation with different transition metals (with more emphasis on Fe) have been discussed. The discussion is based on theoretical and experimental reports published in the literature by different research groups. GaN, ZnO, and AlN have been studied extensively mainly due to the ease with which crystal growth has developed over the years, while there are few reports on ion-solid interaction on InN. Debates, controversies, and contradiction of results are summarised below:

- Firstly, there exist inconsistent reports of displacement energy values in ZnO and III-Nitrides predicted by theoretical models and extracted from experimental observations.
- Several authors agree that AlN and GaN are radiation hard materials and resistant to amorphisation where fluences in the order of $10^{16\text{-}17}$ ion/cm^2 are required to destroy the crystal structure. On the other hand, reports show that InN which is relatively sensitive to radiation damage is amorphised with fluences of ~10^{12} ion/cm^2. Implantation induced damage has been observed in the form of defects and dislocation loops at high fluences ($10^{16\text{-}17}$ ion/cm^2) in GaN. In addition metallic cluster formation has also been observed after high temperature (~1000 K) annealing using different structural characterisation techniques such as XRD, SADP, TEM, and XPS. In ZnO, implantation induced damage was also evident at similar high implantation fluences.
- As highlighted earlier, the lattice site location and the chemical nature of dopants are very important in determining the properties of newly fabricated materials. For GaN and AlN, approximately 80-90% of the TM atoms are substititutionally incorporated on the III sublattice, while heavier elements such as ^{111}In and ^{89}Sr and rare earth elements are slightly displaced about this site. This has been confirmed by different hyperfine interaction techniques such as emission channelling, perturbed angular correlation, Mössbauer spectroscopy as well as ion beam analysis methods such as PIXE and RBS/C. Isolated Fe^{3+} ions surrounded by three and four nearest N atoms have been observed in CEMS measurements in AlN and GaN while coexistence of the 3+ and 2+ charge states in GaN have been proposed from a combination of EPR, PL and SQUID measurements. The Fe^{3+} state was responsible for Curie paramagnetism while van Vleck paramagnetic was attributed to the presence

of Fe^{2+}. As in the case of GaN, both charge states of Fe have also been observed in ZnO with the majority of probe atoms located on substitutional Zn sites (~95%) in EC studies for extremely dilute systems (~10^{12} ions/cm^2). For higher fluences (~10^{16} ions/cm^2), PIXE studies reveal that ~73% of Fe are substitutionally incorporated after high temperature (1323 K) annealing.

- At these high fluences the formation of nanoparticles of transition metal elements, different zinc complexes and/or secondary phases have been reported by various authors/research groups. These complexes/phases accounted for the observed hysteresis loops determined from magnetometry measurements, however, conflicting reports of room temperature ferromagnetism in doped semiconductors have been published.

1.4. A summary of emission Mössbauer studies in oxides

Experimentally, a number of controversial results have been reported for ZnO and GaN based on different types of magnetism and mixed understanding of their origin. Currently, a clear consensus has not been reached [24,25,26]. Some authors have suggested unintentional precipitation of 3*d*-metal impurities and secondary phases to be the source of magnetism [144,145], while other groups suggest defect mediated magnetism [146,147,148,149].

Recently, emission Mössbauer spectroscopy studies following low fluence (~10^{12} cm^{-2}) $^{57}Mn^{*}$ implantation in metal oxides [150,151,152,153] (ZnO, α-Al_2O_3 and MgO), have shown the presence of slow relaxing paramagnetic Fe^{3+}, as opposed to ordered ferromagnetism. In ZnO [153], the relaxation rate (τ^{-1}) was observed to have a T^9 temperature dependence while, in MgO and α-Al_2O_3 [151,152], the relaxation rate was characteristic of a two-phonon Raman process with $\tau^{-1} \alpha T^2$.

A. ZnO

Temperature dependent Mössbauer measurements of Fe in ZnO following Mn^{*} implantation in the absence of an external magnetic field showed magnetic ordering in the local surrounding of substitutional Fe^{3+} at temperatures below 600 K [154]. This behaviour was associated with the formation of complexes with Zn vacancies created during the implantation process. These magnetic complexes were stable around 600 K, even though the nature of the magnetism could not be established,

ferromagnetism was favoured. Furthermore, temperature and dose dependence investigations [154] suggested that the formation of impurity-vacancy complexes is related to the implanted dose and the rate of formation as temperature increases. On the other hand, in our recent experiments [151], the Mössbauer spectra of $^{57}Mn^{*}$/Fe implanted ZnO single crystal in an external field was dominated by sextets whose angular dependence ruled out ordered magnetic effects, such as ferromagnetism which was previously suggested. The observed magnetic structure is attributed to substitutional paramagnetic Fe^{3+} ions with long spin lattice relaxation times (> 20 ns). This effect may be associated with the weak coupling of the Fe^{3+} to the lattice [151]. Paramagnetism was favoured because the relative intensities of the six lines do not follow the angular dependence behaviour expected in ordered magnetism i.e., 3:0:1:1:0:3 for the sextet lines in the θ = 0° measurement. In addition, the results obtained from offline eMS measurements following ^{57}Co/Fe implantation [155] in ZnO with relatively high fluence Fe (>10^{14} ions/cm^2) are consistent with the angular dependence of Fe atoms in crystalline sites (Fe_C). The isomer-shift of the Fe_C component, δ = 0.905(6) mm/s, is practically identical with the value of δ = 0.91(1) mm/s obtained for substitutional Fe^{2+} from $^{57}Mn^{*}$ implantation into virgin ZnO.

B. α-Al_2O_3

The Mössbauer spectra for α-Al_2O_3 [152] at 110 K are dominated by Fe^{2+} in amorphous regions owing to implantation damage while some Fe atoms are located in cubic environments possibly due to nano-precipitates of η-Al_2O_3. This contribution is negligible at temperatures above 500 K. At T < 500 K, incomplete annealing of the implantation damage initially results in the probe atoms in Fe^{3+} state, and above room temperature most likely as Fe^{4+}. The sub-spectrum for Fe^{3+} is masked by slow paramagnetic relaxations typical of a two-phonon Raman process [152].

C. MgO

The Mössbauer spectra of MgO [150] implanted with $^{57}Mn^{*}$ showed similar paramagnetic features as observed for ZnO [151]. The temperature dependent spin relaxation time of Fe^{3+} in MgO is found to decrease to ~10 ns at 647 K by assuming

a relaxation time of $\tau > 1$ μs at 77 K. These results are in agreement with those obtained by electron paramagnetic resonance (EPR) [156], demonstrating the ability to extract spin-lattice relaxation rates for dilute Fe^{3+} from emission Mössbauer spectroscopy using $^{57}Mn^{*}$/Fe-implanted in semiconducting materials. Spin relaxations can occur either due to spin-lattice interactions or spin-spin interactions. The low concentration of implanted Mn/Fe atoms are utilised in our experiments (>100 atomic lattice constants between Mn/Fe atoms), consequently spin-spin relaxations are negligible. The observed long spin-lattice relaxation times (or fast relaxation rates) results from weak interaction between the lattice and Fe^{3+} caused by its spherical ^{6}S ground state [157].

1.5. Paramagnetic relaxation

The electronic spin relaxation of a probe ion incorporated in a lattice proceeds via two processes viz. (i) the spin-lattice relaxation mechanism and (ii) dipolar spin-spin interaction between a pair of paramagnetic ions.

1.5.1. Spin-lattice relaxation

The underlying theory of spin-lattice relaxation and associated processes have been described in detail in texts [158,159] and review articles [160,161,162]. Spin-lattice relaxation between a paramagnetic ion and a crystal lattice occurs when energy transfer takes place between the electronic spin of the ion and phonons of the lattice vibrations which are responsible for a fluctuating crystalline electric field generated by neighbouring ligands at a central paramagnetic ion.

Three basic processes contribute to spin-lattice relaxations. These are schematically illustrated in Figure 1.3 and described briefly below.

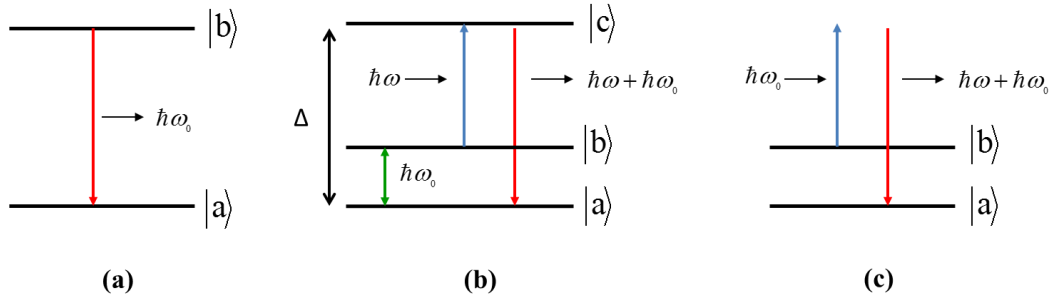


Figure 1.3: Processes that contribute to spin-lattice relaxations: (a) Direct process, (b) Orbach process and (c) Raman Process [163].

a) A direct process is the simplest spin-lattice relaxation process, where a spin transition is associated with the creation or total destruction of a single phonon. As a result the electron spin transition energy is exchanged by the phonon energy, and a linear temperature dependence of the relaxation rate is observed.

b) An Orbach process involves the creation and annihilation of two phonons via population of an excited state, |c>, where the energy difference between the events equals the splitting of participating states, |a> and |b> [164].

c) A Raman process is also a two phonon process similar to the Orbach process, but with excitation to a *virtual level* by the first phonon and de-excitation to the spin ground state by the second phonon [165]. Direct and Orbach processes are relevant at low temperature while at higher temperatures the two-phonon Raman process begins to dominate. In the case of a Kramer ion, such as Fe^{3+}, the relaxation rate, (τ^{-1}) resulting from a Raman process can be described by the equation [158,166],

$$\tau^{-1} = K\int_0^{\omega_m} \frac{\omega^8 \exp\left(\hbar\omega / k_B T\right)}{\left[\exp\left(\hbar\omega / k_B T\right)-1\right]^2} d\omega, \qquad (1.1)$$

which can be simplified to

$$\tau^{-1} = K\left(\frac{k_B T}{\hbar}\right)^9 \int_0^{\theta_D/T} \frac{x^8 e^x}{\left[e^x-1\right]^2} dx, \qquad (1.2)$$

where, K is a constant determined by the interaction between the lattice vibrations and the magnetic ions (Fe^{3+}), ω is the phonon frequency, ω_m is the maximum phonon frequency corresponding to the Debye temperature, $\hbar$ is the reduced Planck's constant, k_B is the Boltzmann constant and T is the temperature.

At $T << \theta_D$, the upper limit can be considered as infinity resulting in a constant value for the integral and a temperature dependence given by $\tau^{-1} \propto T^9$. However, at $T \geq \theta_D$, the integral show temperature dependence as opposed to the low temperature scenario. Consequently, the equation 1.2 can be rewritten as

$$\tau^{-1} = CT^9 \bullet f\left(\frac{\theta_D}{T}\right), \text{ where } f\left(\frac{T}{\theta_D}\right) = \frac{1}{8!}\int_0^{\theta_D/T} \frac{x^8 e^x}{\left[e^x-1\right]^2} dx \qquad (1.3)$$

and C is a constant. Thus, when θ_D/T approaches infinity, the integral approaches 8! and $f(\theta_D/T)$ approaches 1 resulting in a T^9 temperature dependence. On the other hand, when θ_D/T approaches 0, the integrand approximates to x^6 ($x << 0$) and the spin-lattice relaxation rate is expected to follow at T^2 dependence. The spin-lattice relaxation rate for Kramer systems can take either a T^2 or T^9 dependence depending on the temperature region. The lack of high frequency phonons in the Raman process at high temperatures causes a T^2 dependence because the distribution of phonon frequency has an upper limit corresponding to the Debye temperature [166].

1.5.2. Spin-spin relaxation

Spin-spin relaxation involves energy transfer between neighbouring spins through magnetic dipole and/or exchange interactions. The exchange interaction can be expressed in terms of the Hamiltonian for an arrangement of atoms on the lattice as

$$H_{spin} = -J\sum_{j,m} S_j \bullet S_{j+m}, \qquad (1.4)$$

where the subscripts, j, $j+m$ represent the position of the two spins and J is the exchange integral responsible for the spin-spin interaction [167].

This spin-spin interaction is influenced by the distance between the ions and hence depends on the concentration of paramagnetic ions in the sample. For very low concentration of Fe ions ($<10^{-4}$ at.%) the spin-spin relaxation is negligible since the ions are widely spaced. This spin flip mechanism is largely temperature independent.

1.6. Aims and Objectives

The broad aim of the project is to investigate magnetic phenomenon in Fe and/or Co implanted ZnO and III-nitride semiconductors from experimental investigations as a function of implantation fluence, γ-emission angles (θ_γ), measuring temperature (T_m), annealing temperature (T_A) and external magnetic field (H_0). As highlighted in the introduction, Mössbauer spectroscopy was employed in two approaches namely: (i) emission Mössbauer spectroscopy (eMS) at ISOLDE/CERN and (ii) conversion electron Mössbauer spectroscopy (CEMS) at iThemba LABS, Cape Town. In addition, to CEMS, vibrating sample

magnetometer (VSM) measurements were performed to investigate the magnetic properties of ZnO samples.

The specific objectives of this research project are to:

a) Ascertain the nature and origin of magnetism in extremely dilute III-nitride system (~10^{-4} at. %) and compare with previous studies within the fluence range predicted by Dietl [19] of ~5 at.% and also between nitrides and oxides in two fluence regions. Several studies both using ^{57}Fe with concentration in the order of that assumed in Dietl's calculation have been reported in GaN [96,110,111,168] and in ZnO [116,118,169,117,130], and in extremely dilute systems mainly in oxides (ZnO, MgO, and α-Al_2O_3) [150,151,152,153].
b) Determine the lattice site location and charge state of dopants. The resulting properties of doped semiconducting materials are determined not only by the chemical nature of the incorporated dopants but also their lattice location and bonding mechanism in the semiconductor crystal structure. Furthermore, this study will evaluate potential correlation between the charge states and the observed magnetic properties in light of charge-transfer based dilute ferromagnetic ordering suggested by Coey and co-workers [170,171].
c) Investigate the effects of fluence and relative population of dopants in different lattice sites with respect to the possible magnetic properties.
d) Monitor the annealing behaviour of radiation induced damage and formation of nanoclusters/precipitates with respect to implantation fluence and temperature.
e) Establish if vacancies/interstitials/complexes created during the implantation process play a role in the expected/predicted magnetism.
f) Compare the annealing behaviour and lattice location of Fe atoms in wurtzite III-Ns under study with cubic III-Vs from previous studies [172,173] and relate the resulting trends to different crystal structures and physical properties.

These studies were conducted utilising online eMS measurements at ISOLDE, CERN within experiment IS501 with the Mössbauer Collaboration using short-lived radioactive ^{57}Mn* ($t_{1/2}$ = 1.5 min) with extremely low fluences of ~3×10^{12} ions/cm^2 (~10^{-4} at.%) implanted in III-nitrides and ^{56}Fe pre-implanted ZnO. Temperature and angle dependent eMS were carried out in the temperature range

of 100-800 K, and γ-emission angles (θ_γ) of 60º and 0º relative to the *c*-axis of the specimen, respectively. Pre-implantation and/or preparation of samples with stable isotopes (^{57}Fe, ^{56}Fe, and ^{59}Co) were conducted by Dr S. Geburt at the Institute of Solid State Physics, University of Jena, Germany, while CEMS and VSM measurements on as-implanted and annealed samples were carried out at the iThemba LABS, Cape Town, under the guidance of Professor K. Bharuth-Ram and Professor T.B. Doyle, respectively.

Chapter 2

Mössbauer Effect and Hyperfine Parameters

The phenomenon of recoil-free emission and resonant absorption of gamma (γ) rays in nuclei without the loss of energy due to recoil and thermal broadening is known as the Mössbauer effect [174,175]. This effect provides a means of probing the local environments of particular atoms in amorphous or crystalline solids. Comprehensive information on the electronic, magnetic and geometric structure of an impurity atom environment can be extracted from the parameters that characterise the Mössbauer spectrum resulting from hyperfine interactions namely the electric monopole, electric quadrupole and magnetic dipole interactions [176].

2.1. The Mössbauer effect

A free excited nucleus of mass m (with Z protons and N neutrons) recoils to conserve momentum as it decays to the ground state by emitting a γ-ray of energy, E_γ. As a result, the energy carried by the γ-ray is equal to the transition energy, E_o, minus the recoil energy, E_r which prohibits subsequent resonant absorption of the γ-ray by another nucleus of the same kind (Z protons and N neutrons) as illustrated in Figure 2.1.

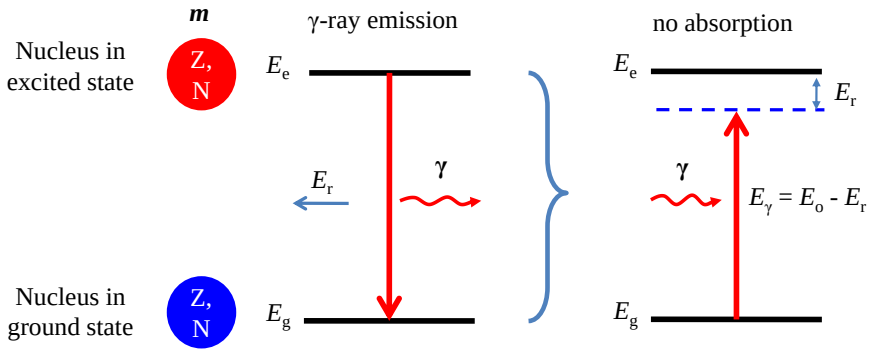


Figure 2.1: Non-resonant γ-ray absorption due to loss in energy to recoil [177].

On the other hand, if the nucleus is bound in a solid matrix with a relatively very large mass $\boldsymbol{M}$ ($>> m$), such that the loss in energy due to recoil becomes infinitesimally small, as a result *recoil free emission* of the γ-ray is possible. This is the core principle of the Mössbauer effect. Thus, the energy of the γ-ray equals the

transition energy between the ground state and the excited state then resonant emission and absorption by another nucleus of the same kind (also bound in a crystal lattice) is a possibility (see Figure 2.2). This discovery earned Rudolf Mössbauer the Nobel Prize in Physics [178] in 1961. De-excitation of the nucleus back to the ground state can proceed either by emission of fluorescent photons or by emission of conversion electrons. The use of conversion electrons in Mössbauer spectroscopy is discussed in section 3.5.

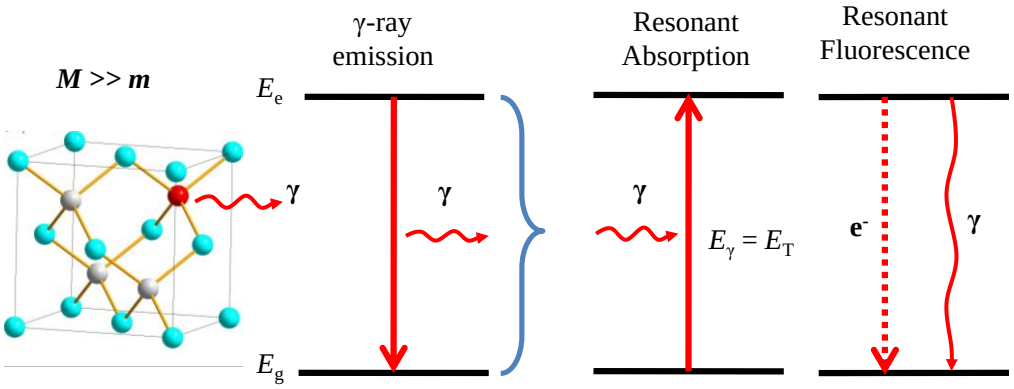


Figure 2.2: Resonant emission and absorption of γ-photon between nuclei, and resonance fluorescence and conversion electrons.

2.2. Recoil free fraction

When the nucleus of γ-ray emitting (or absorbing) atoms is bound in the lattice, the recoil energy is transferred to lattice vibrations in the vicinity of the probe atoms and then dissipated as heat [179]. There are $3N$ (N is the number of atoms) vibration modes in an Einstein model each having the same frequency $\boldsymbol{\omega_E}$, such that the transfer of integral multiples of quantised phonon energy of 0, $\pm\hbar\omega_E$, $\pm 2\hbar\omega_E$,... to the lattice accompanies the emission and absorption of a γ-ray [180]. As a result, for $\boldsymbol{E_r} << \boldsymbol{\hbar\omega_E}$, there exist a probability, of *zero-phonon transitions*, that is, transitions which take place without excitation of lattice vibrations known as the *recoil-free fraction* (f) [178], given by

$$f = \exp-\left[k^2\left\langle x^2\right\rangle\right], \qquad (2.1)$$

where $\left\langle x^2\right\rangle$ is the mean square vibrational amplitude of the nucleus along the direction of the emitted γ-ray wave vector (k).

On the contrary, the Debye model is not limited to the notion of single vibration frequency of lattice atoms, but encompasses a continuum of oscillator frequencies. As a result, the recoil-free fraction also known as the *Debye-Waller factor* or *Mössbauer-Lamb factor* is parameterised using the Debye approximations and leads to an expression for *f*, given by the equation;

$$f = \exp\left\{-\frac{3}{2}\frac{E_\gamma}{k_B\theta_D}\left[1+4\left(\frac{T}{\theta_D}\right)^2\int_0^{\theta_D/T}\frac{x}{e^x\text{-}1}dx\right]\right\}, \tag{2.2}$$

where k_B is the Boltzmann constant and θ_D is the characteristic Debye temperature given by the expression;

$$\theta_D = \frac{\hbar\omega_D}{k_B}. \tag{2.3}$$

For $T << \theta_D$, equation (2.2) reduces to:

$$f = \exp\left[-\frac{E_r}{k_B\theta_D}\left(\frac{3}{2}+\frac{\pi^2T^2}{\theta_D}\right)\right], \tag{2.4}$$

and at absolute zero

$$f=\exp\left(-\frac{3E_r}{2k_B\theta_D}\right). \tag{2.5}$$

In the high temperature limit, for $T > \theta_D$, f approximates to:

$$f=\exp\left(-\frac{6E_rT}{k_B\theta_D}\right). \tag{2.6}$$

The Debye temperature is a measure of the bond strength between the Mössbauer probe atoms and the nearest neighbouring atoms in the crystal lattice [179].

2.3. Spectral line shape and natural linewidth

The experimental observation of resonance in Mössbauer spectroscopy for a particular nuclide is determined by the mean lifetime (τ_N) of the excited state and the transition energy (E_0). The energy distribution about E_0 is given by the Breit-Wigner formula [179],

$$I(E) = \frac{(\Gamma/2)^2}{(E - E_0)^2 + (\Gamma/2)^2}, \tag{2.7}$$

which gives a Lorentzian distribution as shown in Figure 2.3.

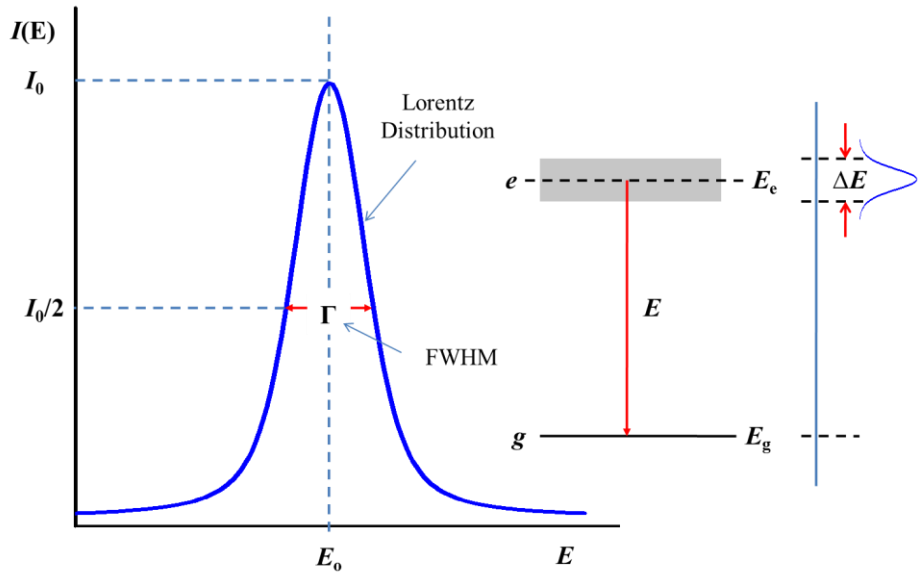


Figure 2.3: Intensity distribution for γ-ray emission as a function of transition energy E_0 [179] where *e* and *g* are excited and ground states, respectively.

According to Heisenberg Uncertainty Principle, a nuclear level with a mean lifetime (τ_N) has an energy uncertainty (Γ) given by

$$\Gamma = \frac{\hbar}{\tau_N}, \tag{2.8}$$

where Γ is the *natural line width* which represents the *full width at half maximum* (FWHM) of the Lorentzian line shape.

2.4. Mössbauer isotope: ^{57}Fe

The first recoil free resonant emission and absorption was observed in the 129 keV γ-photon transition of ^{191}Ir in 1957 [178]. Since then, several elements in the periodic table have been used as Mössbauer isotopes, among which ^{57}Fe is the most exploited isotope. First reports of the Mössbauer effect in ^{57}Fe were published in 1959 by independent groups of Schiffer and Marshall [181] and Pound and Rebka [182]. In this study, the ^{57}Fe Mössbauer isotope was utilised. Its first excited state has an energy of 14.4 keV and a mean lifetime of 141 ns, resulting in a natural linewidth of ~ 4.67×10^{-9} eV and an energy resolution, $E_\gamma / \Gamma \sim 3.1 \times 10^{12}$. Thus, variations in

the nuclear levels as small as 1 part in 10^{12} can be detected [183], implying that Mössbauer spectroscopy has undeniably the best energy resolution as compared to other spectroscopic techniques.

In the present study, radioactive $^{57}Mn^{*}$ and a standard $^{57}Co^{*}$ source were employed as precursor isotopes for ^{57}Fe; their respective decay schemes are shown in Figure 2.4.

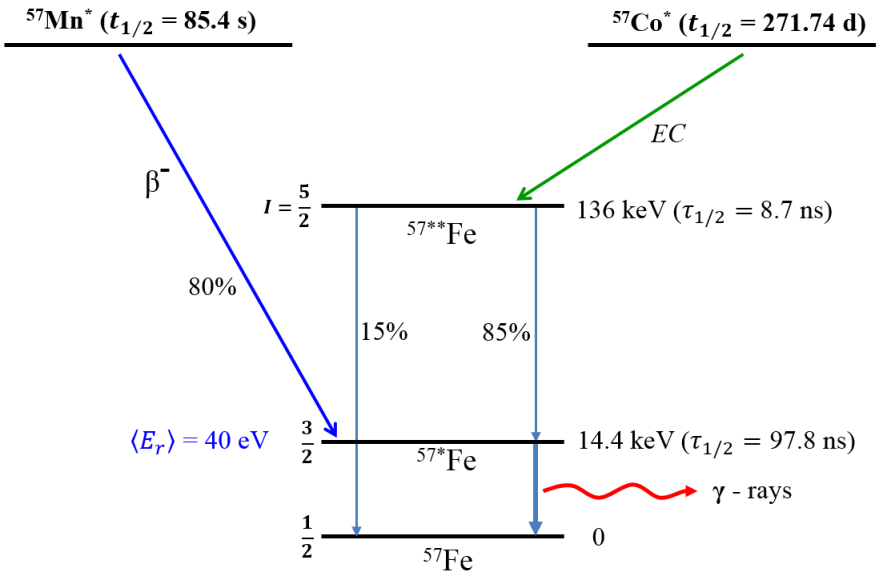


Figure 2.4: Decay schemes for $^{57}Mn^{*}$, $^{57}Co^{*}$ and ^{57}Fe

$^{57}Mn^{*}$ beta decays directly to the 14.4 keV state of ^{57}Fe with 80% probability imparting a mean recoil energy of 40 eV to the Fe atoms, while $^{57}Co^{*}$ decays by electron capture (*EC*) yielding the 136 keV excited state of ^{57}Fe. The 136 keV state undergoes a transition with a half-life of 8.7 ns, to the ground state either by direct emission of 136 keV γ-rays (15%) or by first emission of a 122 keV photon to the 14.4 keV Mössbauer excited state.

2.5. Mössbauer spectrum

A Mössbauer spectrum is recorded by detecting the resonant absorption of the γ-radiation emitted in the transition to the ground state of the radioactive probe nucleus in the source by a stable nucleus of the isotope in a suitable absorber material [184]. The resonance absorption is detected by an increase or decrease in the counts at the resonant velocities in backscattering geometry or transmission geometry, respectively. A γ-ray with variable energy is required to observe

resonance between the source and the absorber. This is achieved by vibrating the absorber (detector) relative to a stationary source (sample) thus modulating the γ-ray energy by the Doppler effect in emission Mössbauer spectroscopy. The level of resonant absorption at each velocity is determined by how much of the shifted absorption energy profile overlaps with the relatively stationary emission energy profile spectrum as shown in Figure 2.5 (a). The greater the overlap, the higher the intensity of the resonant absorption line as illustrated in Figure 2.5 (b) which shows the progress in the development of an emission Mössbauer spectrum as the absorber (detector) is moving from negative to positive velocities relative to a stationary source (sample).

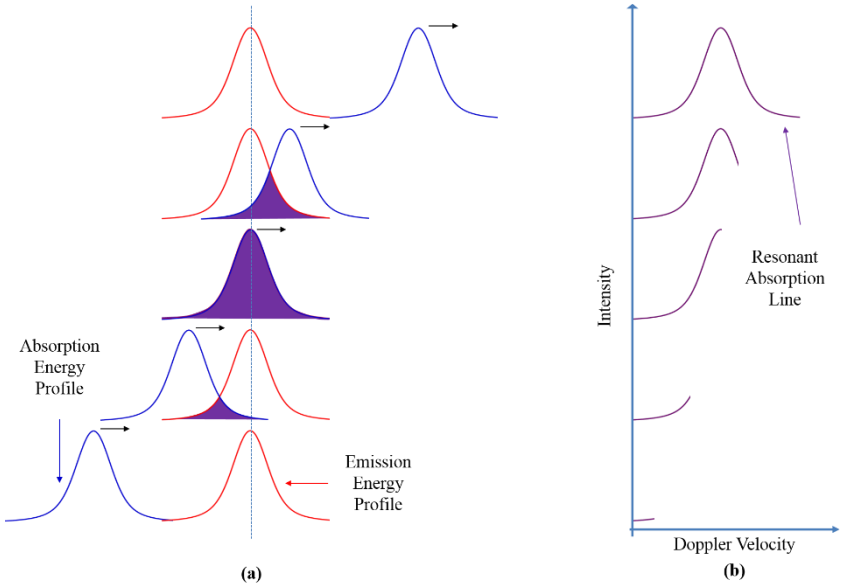


Figure 2.5: Progress in the development of an emission Mössbauer spectrum [177].

The velocities for resonant absorption and the overall shape of the spectrum are determined by the combined effect of the hyperfine interactions which depend on the environments of the Mössbauer atoms. *Hyperfine interactions* are interactions between the nucleus and its surrounding electrons which cause nuclear energy levels changes of the order of 10^{-7}-10^{-8} eV [185]. Mössbauer effect connects the nucleus with its nearest neighbours through hyperfine interactions.

2.6. Hyperfine interaction parameters

The hyperfine interactions give a direct measure of these very small perturbations of the nuclear energy levels. These energy fluctuations are sensitive to changes in

the structure, whether crystalline or amorphous, lattice periodicity and probe nucleus-complexes. In addition, variations in the oxidation state of the probe nucleus in a compound, coordination, magnetic ordering, and the effects of ligands, as well as the diffusion and relaxation effects of ions in a solid can be explored using Mössbauer spectroscopy [179,185] through the information obtained from hyperfine parameters of fitted spectral components.

2.6.1. Isomer Shift: Electric Monopole Interaction

The isomer shift is due to electrostatic interaction between the charge distribution of the nucleus and *s*-electrons which cause shifts in the nuclear energy levels of the absorber and the source nuclei [186]. As a result, the nuclear ground state and excited state levels are affected in different extents as illustrated in Figure 2.6 (a) depending on their respective bonding mechanism with neighbouring atoms.

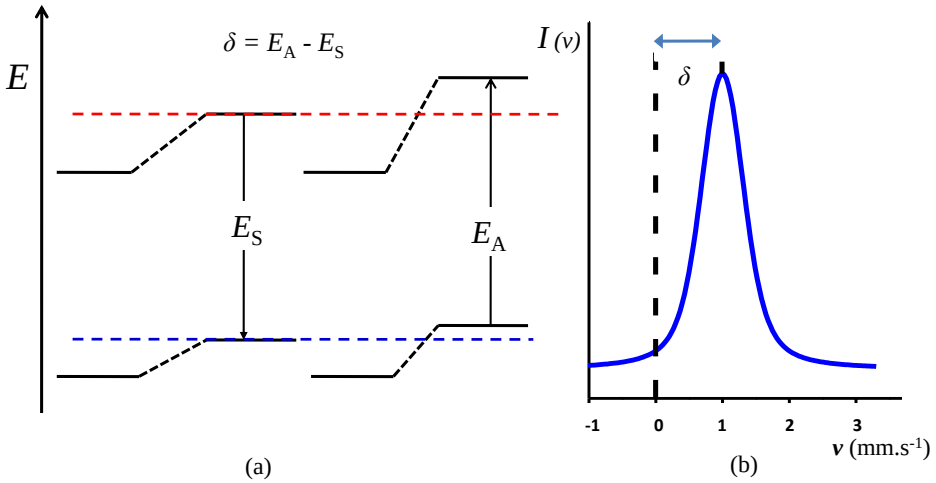


Figure 2.6: The nuclear energy levels shifts in the source and absorber due to the electric monopole interaction (a) resulting in the Mössbauer isomer shift [177] shown in (b).

The transition energies in the source and absorber nuclei are given by the equations [179];

$$E_A = \frac{2}{3}\pi Z e^2 |\psi(0)|_A^2 \left[\left\langle r_e^2 \right\rangle - \left\langle r_g^2 \right\rangle\right], \tag{2.9}$$

and

$$E_S = \frac{2}{3}\pi Z e^2 |\psi(0)|_S^2 \left[\left\langle r_e^2 \right\rangle - \left\langle r_g^2 \right\rangle\right], \tag{2.10}$$

where $\langle r^2 \rangle$ the expectation is value for the square of the nucleus radius and $|\psi(0)|^2$ is the corresponding probability density.

When the nuclei are in different local environments, the electron densities at the nuclei in the source and the absorber will be different. Consequently, the Mössbauer transition energy will vary slightly between the two nuclei, such that to observe resonant absorption, a γ-ray with variable energy within the limits of the shift of the nuclear energy levels is required. Experimentally, this is achieved by vibrating the source or detector along the direction of propagation of the γ-ray for absorption or emission experiments, respectively. Thus, a shift in the position of the absorption or emission peak from zero velocity is evident on the spectrum (Figure 2.6 (b)) and this shift is known as the *isomer shift* (δ). On the other hand, when the nuclei are in the same local neighbourhoods in both the source and absorber, their transition energies are equal and hence Mössbauer resonance absorption will occur at zero velocity.

In terms of spectra, the isomer shift resembles the velocity at which maximum resonant absorption occurs, while the difference in the relative energy levels between the source and the absorber, ΔE, is equal to the shift caused by the Doppler effect at this particular velocity. Thus, the isomer shift, can be written as

$$\delta_{IS} = E_A - E_S, \tag{2.11}$$

which is given by the expression [179],

$$\delta_{IS} = \frac{2}{5}\pi Ze\left(\rho_a - \rho_s\right)\left(R_e^2 - R_g^2\right), \tag{2.12}$$

where Z is the atomic number, e is the electronic charge. R_e and R_g are the radii of the excited and ground state nuclei, respectively. The isomer shift is hence proportional to the difference in the electron densities at the probe nuclei in the source (ρ_s) and absorber (ρ_a). It is solely dependent on the *s*-electron density which is affected by the presence of overlapping *p*, *d*, and *f* orbitals because the spatial distribution of the *s*-electrons is shielded or screened from the nucleus by *p*, *d*, and *f* electrons through inter-electronic repulsion. A gradual increase in the number of 3*d* electrons causes a reduction in the *s*-electron density, resulting in the isomer shift of Fe^{2+} ($3d^6$) shifting more towards positive velocity than Fe^{3+} ($3d^5$) [186]. The isomer shift is therefore sensitive to the charge density distribution caused by the environments around the nucleus, that is, any factor that affects the number and/or

distribution of valence electrons [186]. This gives information on the oxidation state, coordination number, electronegativity of ligands, bond character and spin state of the iron atoms. Figure 2.7 presents a summary of isomer shift values observed in ^{57}Fe compounds for different charge and spin states for Fe [179].

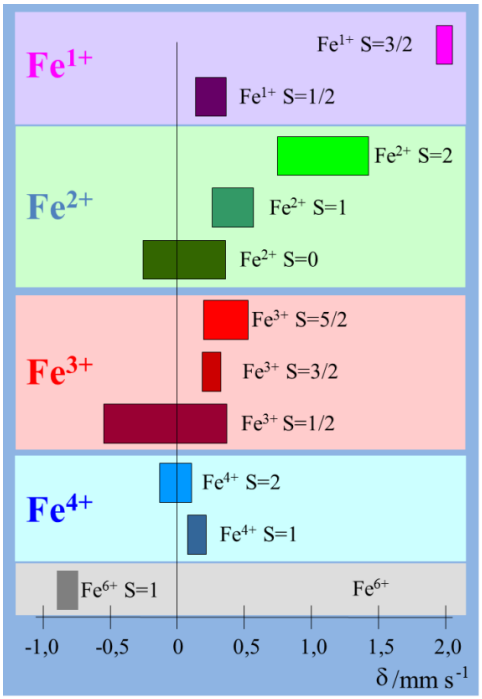


Figure 2.7: Isomer shift values observed for ^{57}Fe compounds measured relative to α-Fe at room temperature.[Adapted from Gütlich [179]]

2.6.2. Quadrupole Splitting: Electric Quadrupole Interaction

The quadrupole splitting originates from the electric quadrupole interactions and relates to rotational structural arrangements that a non-spherical nucleus experiences in a non-homogenous electric field generated by a non-cubic charge distribution of the surrounding electrons. A nucleus with, $I > 1/2$ has a non-spherical charge distribution and this creates a nuclear quadrupole moment which is a (3 × 3) second-rank tensor and may be expressed as

$$Q = \frac{1}{e}\int \rho(\boldsymbol{r})(3z^2 - \boldsymbol{r}^2)\mathrm{d}\boldsymbol{r}\,, \qquad (2.13)$$

in the principal axis system [187]. The nuclear quadrupole moment is a measure of deviations of the nuclear charge distribution from spherical symmetry. The quadrupole moment interacts with the electric field gradient (EFG) around the nucleus, which is generated whenever the nuclear environment has a charge

distribution lower than cubic symmetry. The EFG is defined as the second spatial derivative of the electric potential $V(r)$ at $r = 0$ (acting at the nucleus), such that

$$V_{ij} = \frac{\partial^2 V}{\partial x_i \partial x_j} \text{ (where } i, j = x, y, z), \tag{2.14}$$

are nine components of a 3 × 3 second rank EFG tensor and it contains information on the symmetry and orientation of the charge distribution with respect to the crystal lattice [179]. Thus, to investigate the electric quadrupole interaction, the electric quadrupole Hamiltonian may be written in the form [187],

$$H_Q = \frac{eQV_{zz}}{4I(2I-1)}\left[3\hat{I}_z^2 - \hat{I} + \eta\left(\hat{I}_x^2 - \hat{I}_y^2\right)\right], \tag{2.15}$$

where e is the electron charge, Q is the nuclear quadrupole moment, V_{zz} is the principal axis component of the EFG interacting with the quadrupole and η is an asymmetry parameter of the electric field given by,

$$\eta = \frac{V_{XX} - V_{YY}}{V_{ZZ}}, \tag{2.16}$$

and must satisfy the condition, $0 \leq \eta \leq 1$. The asymmetry parameter is a measure of the deviation of the EFG from axial symmetry; in the presence of axial symmetry at a specific lattice site, $\eta = 0$ [187]. The EFG is essentially a measure of the inhomogeneity of the electric field. The electric charges distributed around a Mössbauer nucleus can contribute to the EFG only when their symmetry is non-cubic. This situation also exists in the presence of defects in the vicinity of the Mössbauer atom.

The interaction between the nuclear quadrupole moment and the EFG splits the nuclear energy levels into sub-states with spin I, $(I - 1)$, $(I - 2)$,.., $-(I - 2)$,$-(I - 1)$, $- I$ without removing the degeneracy between the states having the same spin quantum number I [188,189]. The degree of splitting of these lines is a measure of the energy difference between the sub-states and depends on the orientation and magnitude of the EFG, and the nuclear quadrupole moment. The quadrupole moment for a given nucleus is known, but the EFG may arise from charges on the neighbouring ion or ligands surrounding the Mössbauer atom and charges in partially filled orbitals of

the Mössbauer atom [185]. If lattice sites have a point group symmetry less than cubic then the line splitting will occur if the nuclear states have finite quadrupole moments. The energy difference between the two sublevels equals the separation between the two resonance lines (*a doublet*) on the Mössbauer spectrum and is known as the *quadrupole splitting* given by the expression,

$$\Delta E_{\mathrm{Q}} = \pm \frac{eQV_{zz}}{2}\left(1+\frac{\eta^2}{3}\right)^{1/2}. \qquad (2.17)$$

The quadrupole splitting can either be positive or negative depending on the sign of Q and V_{zz}. In the case of ^{57}Fe, $Q > 0$ and the sign of the quadrupole splitting is solely dependent by the sign of V_{zz}. The determination of the sign of the quadrupole splitting is possible in a single crystal where the orientation of the crystal symmetry axis is the same over the whole crystal volume, but not in powder and polycrystalline samples because the crystal axes are randomly oriented. Consequently, in the latter two cases the lines of the symmetric quadrupole doublet obtained cannot be assigned to either of the $\pi(\pm 1/2 \rightarrow \pm 3/2)$ and $\sigma(\pm 1/2 \rightarrow \pm 1/2)$ transitions [179,185]. An external magnetic field is required to further split the lines in polycrystalline and powder samples [190].

In ^{57}Fe, the ground state has a spin $I = 1/2$ while the 14.4 keV excited state, a spin, $I = 3/2$. The quadrupole moment is zero for spin 1/2 and the presence of an EFG does not affect the ground state but splits the excited state into $m_{\mathrm{I}} = \pm 3/2$ and $m_{\mathrm{I}} = \pm 1/2$ sublevels. Thus two transitions from the ground state are possible, resulting in two lines in the Mössbauer spectrum as depicted in Figure 2.8.

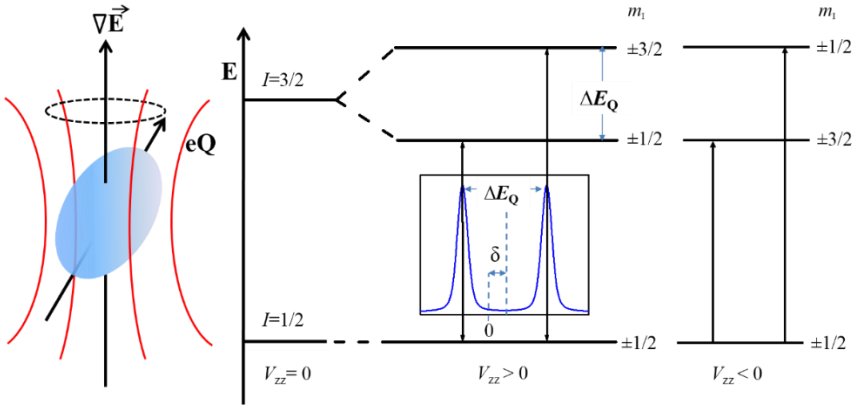


Figure 2.8: Splitting of the energy level in the ^{57}Fe state with I=3/2 resulting in quadrupole splitting of the resulting Mössbauer spectrum.

Thus, the lattice symmetry reflecting the effect of coordinating atoms, and the clustering of the atoms can be studied by measuring the quadrupole splitting. There are two fundamental sources that contribute to the electric field gradient which are given by,

$$\left(V_{zz}\right)_{total} = \left(V_{zz}\right)_{Lat} + \left(V_{zz}\right)_{Val}, \qquad (2.18)$$

in the principal axis system with $\eta = 0$ [179,185]. The lattice (ligand) contribution $(V_{zz})_{Lat}$ results from the charges on the neighbouring ions or ligands surrounding the Mössbauer atom. The second source is known as the valence electron contribution $(V_{zz})_{Val}$ which arise as a result of the changes in the partially filled valence orbitals of the Mössbauer atom. The valence contribution results from $(V_{zz})_{CF}$ due to the aspherical population of the *d*-orbitals caused by the crystal field and $(V_{zz})_{MO}$ due anisotropic molecular bonding [185].

2.6.3. Magnetic Splitting: Magnetic Dipole Interaction

A nucleus may be associated with a characteristic angular momentum (I), which is accompanied by a magnetic dipole moment. A magnetic dipole interaction is evident when the nuclear states involves a magnetic dipole moment, and in the presence of a magnetic field ($\boldsymbol{B}$) at the nucleus, either produced by the surrounding electrons or ions present or applied externally. This interaction leads to a precession of the magnetic moment about the field direction, which results in the splitting of energy levels into $2I+1$ sub-states characterised by the magnetic spin quantum number, m_I. The splitting of the nuclear energy levels, equivalent in principle to the Zeeman effect in atoms in optical spectroscopy is known as *magnetic splitting* or the *nuclear Zeeman effect*.

A nuclear state with $I > 0$ possesses a magnetic dipole moment, and for ^{57}Fe, there exists magnetic dipole moments for both the ground state and the first excited state. This effect leads to a complete removal of the degeneracy of the nuclear levels, and the ground state with $I = 1/2$ splits into two sub-states and the excited state with $I = 3/2$ into four sub-states as depicted in Figure 2.9. The selection rules for the magnetic dipole transition ($\Delta m_I = 0, \pm 1$) allow for γ transitions between the sublevels six possible transitions resulting in six absorption lines (*sextet*) in the

Mössbauer spectrum. The energies of the sublevels are given by first order perturbation theory,

$$E_M(m_I) = -g_N \mu_N \boldsymbol{B} m_I, \tag{2.19}$$

where g_N is the nuclear Landé factor and μ_N is the nuclear Bohr magneton.

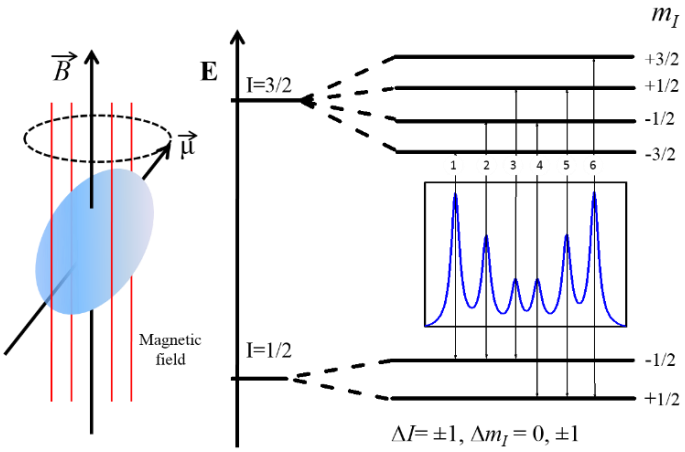


Figure 2.9: Magnetic dipole interaction resulting in the nuclear Zeeman splitting of the energy levels and the Mössbauer spectrum showing a sextet [177].

The magnetic hyperfine splitting allows for the determination of the magnitude and direction of the effective magnetic field ($\boldsymbol{B}_{eff}$) acting at the nucleus. The effective magnetic field is given by the sum of the local magnetic field $\boldsymbol{B}_{loc}$ at the Mössbauer nucleus by the lattice and the hyperfine magnetic field $\boldsymbol{B}_{hf}$ of the Mössbauer atom's own electrons:

$$\boldsymbol{B}_{eff} = \boldsymbol{B}_{loc} + \boldsymbol{B}_{hf}. \tag{2.20}$$

The local magnetic field may result from the material's own magnetic ordering, and/or by an externally applied field or both. $\boldsymbol{B}_{loc}$ may have the following contributions [185]:

$$\boldsymbol{B}_{loc} = \boldsymbol{B}_{ext} - \boldsymbol{D}_{\mathbf{M}} + \frac{4\pi}{3}\boldsymbol{M}_m, \tag{2.21}$$

where $\boldsymbol{B}_{ext}$ is an external field, $\boldsymbol{M}_m$ is the magnetisation, $\boldsymbol{D}_{\mathbf{M}}$ represents the demagnetisation field, and the $4\pi/3(\boldsymbol{M}_m)$ represents the Lorentz field.

Many materials can also create their own magnetic hyperfine field ($\boldsymbol{B}_{hf}$) which has three contributions [179,185];

$$\boldsymbol{B}_{hf} = \boldsymbol{B}_F + \boldsymbol{B}_L + \boldsymbol{B}_D. \tag{2.22}$$

$\boldsymbol{B}_F$ is Fermi contact field which arises from the *s*-electron spin density and $\boldsymbol{B}_L$ is called the orbital field due to the orbital motion of unpaired electrons around the nucleus. Finally, the third term $\boldsymbol{B}_D$ is the dipole field at the nucleus stemming from the total spin magnetic moment of the valence electrons.

2.6.4. Combined magnetic and quadrupole interactions

Often both the magnetic and the quadrupole splitting are present and the combined effect yields an asymmetric sextet. In order to obtain the eigenvalues and eigenvectors of the combined nuclear Hamiltonian, and in turn the transition energies and relative line intensities, transformation from one axial frame to another is necessary since the quantisation *z*-axes of the magnetic dipole and electric quadrupole do not always coincide [187]. However, the quadrupole interaction is usually much smaller than the magnetic hyperfine interaction and may be treated as a perturbation on the magnetic effect. Thus, in the case of $\eta = 0$, the eigenvalues are given by

$$E_{Q,m} = -g_n \mu_N B m_I + (-1)^{|m_I|+\frac{1}{2}} \frac{eQV_{zz}}{8}(3\cos^2\beta - 1), \qquad (2.23)$$

where β is the angle between the principal axis of the EFG tensor and the hyperfine field, while the last term gives the *quadrupole shift* (ϵ_Q) [179]. As a result the shape of the Mössbauer spectrum depends not only on the relative strengths of the two interactions but also the relative orientation of the EFG principal axis, the magnetic field and the incident γ-ray [179,185,187].

2.6.5. Angular dependence of hyperfine parameters

2.6.5.1. Quadrupole splitting

For $\eta = 0$, the angular dependence of the quadrupole split doublet is governed by the ratio of the intensities between the $\pi_{(\pm1/2\rightarrow\pm3/2)}$ and $\sigma_{(\pm1/2\rightarrow\pm1/2)}$ transitions given by

$$f(\theta) = \frac{I_\pi}{I_\sigma} = \frac{3(1+\cos^2\theta)}{5-3\cos^2\theta}, \qquad (2.24)$$

where θ is the angle between the γ-ray direction and the V_{zz} direction with values of 0.6 and 3.0, for $\theta = 90^o$ and $\theta = 0^o$, respectively. However, at $\theta = 54.7^o$, known as the *magic angle*, $f(\theta) = 1$; the two peaks have equal intensities. The sign for the

quadrupole splitting is governed by the sign of the principal component (V_{zz}) of the EFG, which is either positive or negative depending on whether the $m_I = \pm 3/2$ energy level is higher or lower than the $m_I = \pm 1/2$ energy level. The sign of the EFG and geometry of the experimental set-up determines which leg of the asymmetric doublet is more intense. If $\Delta E_Q > 0$, the left leg is more intense at small angles in emission geometry, while the right leg is more intense at small angles in transmission geometry. The reverse is true when $\Delta E_Q < 0$.

2.6.5.2. Magnetic splitting

The intensities of the six lines are different but their linewidths are in principle equal. The intensity ratio of each line is found as the matrix element represented by the Clebsch-Gordon coefficients multiplied by the appropriate angle (θ) between the direction of the γ-radiation and that of the magnetic hyperfine field [184,187]. The observed relative line intensities are in the form 3:*R*:1:1:*R*:3 for the energy transition, $I = 1/2 \rightarrow 3/2$ in ^{57}Fe where,

$$R = \frac{4\sin^2\theta}{1+\cos^2\theta}. \tag{2.25}$$

For a thin absorber, the recoil-free fraction *f* is isotropic, and when the angle between ***B*** and the γ-ray is $\theta = 0^o$, $R = 0$, and the lines 2 and 5 of the sextet disappears completely when $\theta = 90^o$, $R = 4$. However, if the magnetic field vectors at the nuclei are randomly oriented such as in a powder, then the intensity ratio is 3:2:1:1:2:3.

2.6.6. Temperature dependence of hyperfine parameters

2.6.6.1. Thermal vibrations: Second order Doppler Shift

The thermal motion of the Mössbauer nuclei in addition to the aforementioned electric monopole interactions also contributes to the changes in the nuclear energy levels. These temperature dependent thermal vibrations cause a further shift in the energy levels called the *second-order Doppler shift* (δ_{SOD}) or *temperature shift* which is related to the mean-square velocity of lattice vibrations in the direction of the γ-ray propagation by the expression:

$$\delta_{SOD} = \Delta E_{SOD}\frac{c}{E_0} = -\frac{\langle v^2\rangle}{2c^2}E_0\frac{c}{E_0} = -\frac{\langle v^2\rangle}{2c}. \tag{2.26}$$

Thus, an increase $\langle v^2 \rangle$ with increasing temperature moves the resonance signal to more negative velocities. As a result, the total experimental shift of the entire Mössbauer spectrum is known as the center shift (δ_C), which is given by the sum of the isomer shift (δ_{IS}) and the second-order Doppler shift (δ_{SOD}). The shift of the energy levels due to the thermal vibrations can be approximated in a Debye model as follows;

$$\delta_{SOD} = -\frac{3}{2}\frac{k_B \theta_D}{mc}\left[\frac{3}{8} + 3\left(\frac{T}{\theta_D}\right)^4 \int_0^{\theta_D/T} \frac{x^3}{e^x - 1} dx\right], \qquad (2.27)$$

where the terms carry conventional meanings defined earlier.

2.6.6.2. Quadrupole Splitting

The quadrupole splitting decreases with increasing temperature and stems mainly from the temperature dependence of the different valence electron levels of the Mössbauer atom. This arises from the temperature dependence of the EFG created by both the surrounding lattice and valence electrons with the assumption that the valence contribution is not negligible [179,191]. The temperature dependence is mainly due to thermal expansion of the crystal lattice and the influence of the created phonons on the conduction electrons [188,192]. The temperature dependence of the EFG expressed in terms of the principal component can be described by the empirical equation [193,194],

$$V_{zz}(T) = V_{zz}(0)\left(1 - B \cdot T^{3/2}\right), \qquad (2.28)$$

which is most applicable for cubic system, where B is a fitting parameter. However, from equation 2.18, the total V_{zz} is the sum of $(V_{zz})_{Lat}$ and $(V_{zz})_{Val}$, where the latter is a combination of $(V_{zz})_{CF}$ and $(V_{zz})_{MO}$. The $(V_{zz})_{Lat}$ and $(V_{zz})_{MO}$ are least affected by temperature while the $(V_{zz})_{CF}$ has strong temperature dependence. In distorted environments, the degeneracy of orbitals may be completely removed such that in the case of Fe^{2+}, with increasing temperature the sixth electron has a higher probability of being promoted to a high-energy state [185]. This increases the symmetry of electron population causing a decrease in the quadrupole splitting which can be calculated from Ingalls [191] by

$$\Delta E_Q = \Delta E_{Q,0} \times \left\{1 - \exp(-E_0 / k_B T)\right\} / \left\{1 + 2\exp(-E_0 / k_B T)\right\}, \qquad (2.29)$$

where $\Delta E_{Q,0}$ is the quadrupole splitting at 0 K and E_0 is the splitting energy between the z^2 and x^2-y^2 orbitals. However, in the case of Fe^{3+}, the quadrupole splitting is not affected by removing the orbital degeneracy and is temperature independent [185].

2.6.7. Relaxation in Mössbauer Spectroscopy

The magnetic hyperfine field experienced at the nucleus of a magnetic ion stems from the electron spin of the ion via core polarisation [195]. The electron spins in a material are coupled to the lattice via spin lattice interactions [196], such that any disturbance in the electron spin propagates through the entire lattice because of exchange interactions. As a result, changes in the spin of an ion produces fluctuations in the field sensed by the nucleus and if the lifetime of these time dependent fluctuations (i.e. relaxation time, τ_r) is comparable to the nuclear Larmor precession time (τ_l), then relaxation effects are observable [179,187]. The Larmor precession time gives the minimum time required for the nucleus to sense the hyperfine field and is defined as the time taken for a nuclear spin state, I to split into $(2I+1)$ sub-states under the influence of the hyperfine field. However, as a prerequisite, the lifetime of the Mössbauer event should be much greater than τ_l such that the hyperfine fields are detectable in Mössbauer spectroscopy.

Thus, the effect of relaxation effects on the Mössbauer spectra is governed by the relaxation time with respect to the Larmor precession time:

a) for very slow relaxation, ($\tau_r \gg \tau_l$), the hyperfine field is static during a Larmor precession period and the nucleus senses each spin state separately resulting in narrow spectral line which has Lorentzian lineshape.
b) for very fast relaxation, ($\tau_r \ll \tau_l$) the nucleus senses a zero time average of the electron spin, as a result no magnetic interaction is observed.
c) when the spin relaxation is neither too long nor too short compared to the precession time, ($\tau_r \approx \tau_l$), complex spectra with broadened line shapes are observed.

As highlighted earlier in Chapter 1, the electron spin flip processes (relaxation) of a probe ions incorporated in a lattice proceeds either through spin-spin or spin-lattice interaction.

Chapter 3

Materials Modification and Experimental Details

This chapter describes the sample preparation by ion implantation as the preferred method for material modification by incorporating foreign transition metal atoms in semiconductor materials with the aim to synthesise dilute magnetic semiconductors (DMS). The theory behind ion implantation and its application in semiconductor research and technology are detailed in several texts [60,197] , book chapters [198,199], review articles [200,201,202,203] and a previous research report [177]. In addition, two experimental techniques utilised for investigating magnetic properties are presented. The main technique is Mössbauer spectroscopy, employed as: (i) emission Mössbauer spectroscopy (eMS) using short-lived radioactive isotopes at ISOLDE/CERN and (ii) conversion electron Mössbauer spectroscopy (CEMS), on ^{57}Fe implanted samples using a standard 50 mCi ^{57}Co(Rh) source. In light of the vast applications [204] in industry and research, several books [198,179,185,180] on Mössbauer spectroscopy have been published since its discovery. In this chapter, a summary of Mössbauer spectroscopy is presented. In addition, a vibrating sample magnetometer (VSM) was used as a complementary technique to investigate the magnetic properties of potential DMS materials. A brief introduction of the principle of operation of a VSM system is discussed. More importantly, also included are specific experimental details of the measurements undertaken on different samples.

3.1. Description of samples

Single crystal and thin film growth can be achieved by a number of different methods which include, MBE, MOCVD, pulsed laser deposition (PLD), metalorganic vapour phase epitaxy (MOVPE), sputtering, hydrothermal and hydride vapour phase epitaxy (HVPE) [205]. Commercially available undoped ZnO single crystals and nitride films with a hexagonal (wurtzite) crystal structure and (0001) plane with surface areas of 10 mm × 10 mm were used in this study. Table 3.1 gives a summary of the suppliers, film thicknesses, substrates used and growth methods.

Table 3.1: Details of samples used in this study.

Material	Supplier	Film thickness	Substrate	Growth mechanism
ZnO	Crystec, Germany	0.5 mm	Single Crystal	Hydrothermal
AlN	MTI Corporation, USA	0.1 µm	Sapphire	HVPE
GaN	MTI Corporation, USA	0.5 µm	Sapphire	HVPE
InN	TDI – Oxford Instruments -USA	0.1 µm	GaN/Sapphire	HVPE

In order to check the crystallinity of the materials, X-ray diffraction (XRD) measurements were performed on all the samples using a Phillips PW1820 diffractometer. The XRD patterns for the nitride films and ZnO single crystal samples are displayed in Figures 3.1-3.3 and 3.4, respectively, with the peak assignments guided by the results in the literature for the corresponding materials; AlN [206,207], GaN [208,209,210], InN [210,211,212] and ZnO [133,144]. As reflected in Figures 3.1-3.3, additional peaks corresponding to the substrates are observed, mainly the 0006 plane for α-Al_2O_3 in all nitride films. Similarly, the 0002 and 0004 planes for GaN are also observed in InN.

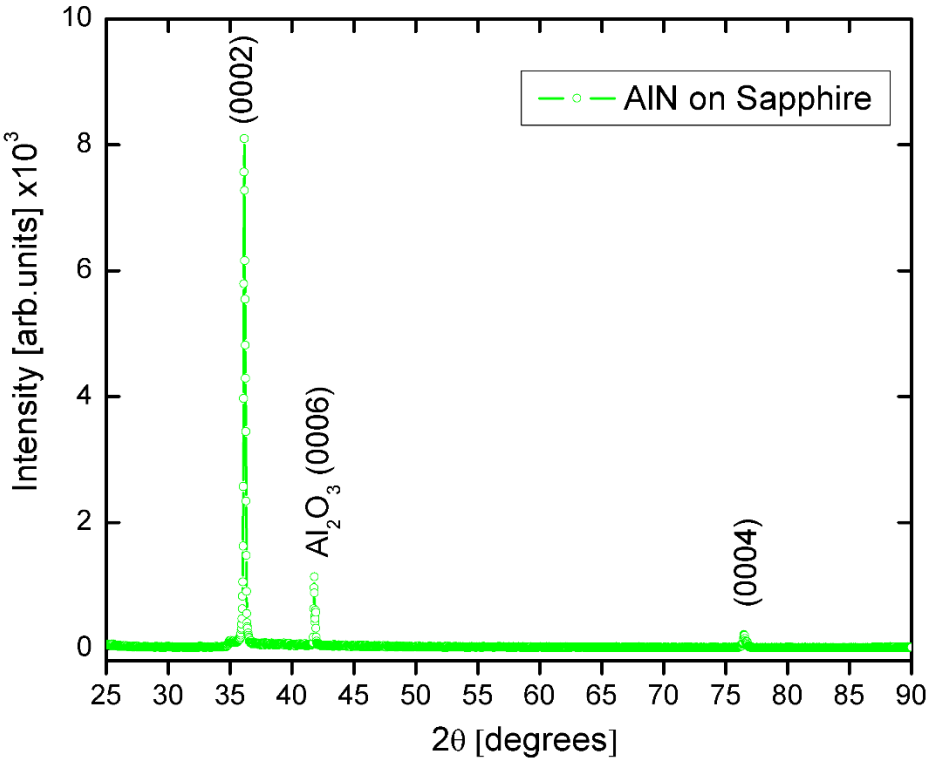


Figure 3.1: XRD pattern for AlN film on a Sapphire substrate.

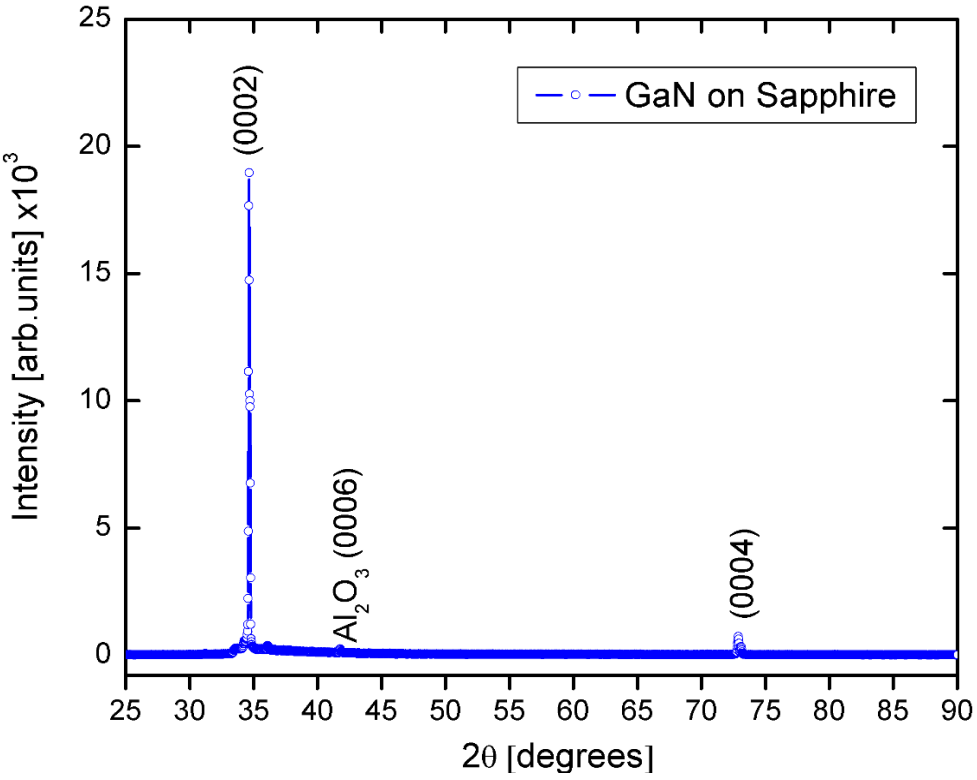


Figure 3.2: XRD pattern for GaN film on a Sapphire substrate.

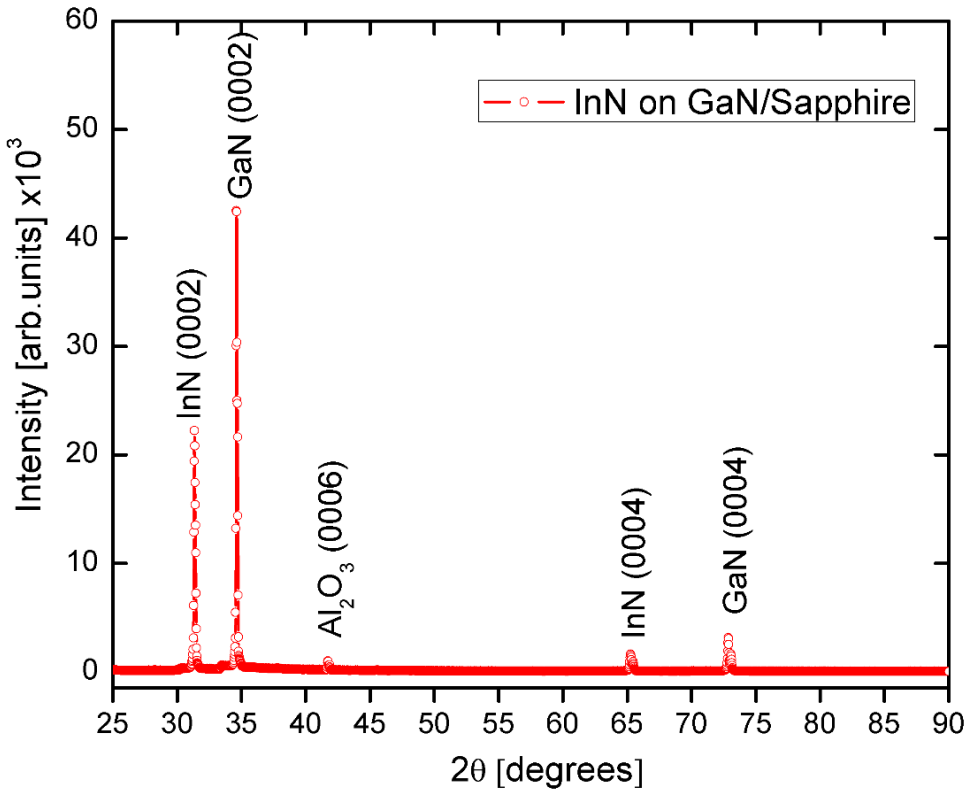


Figure 3.3: XRD pattern for InN film on GaN/Sapphire substrates.

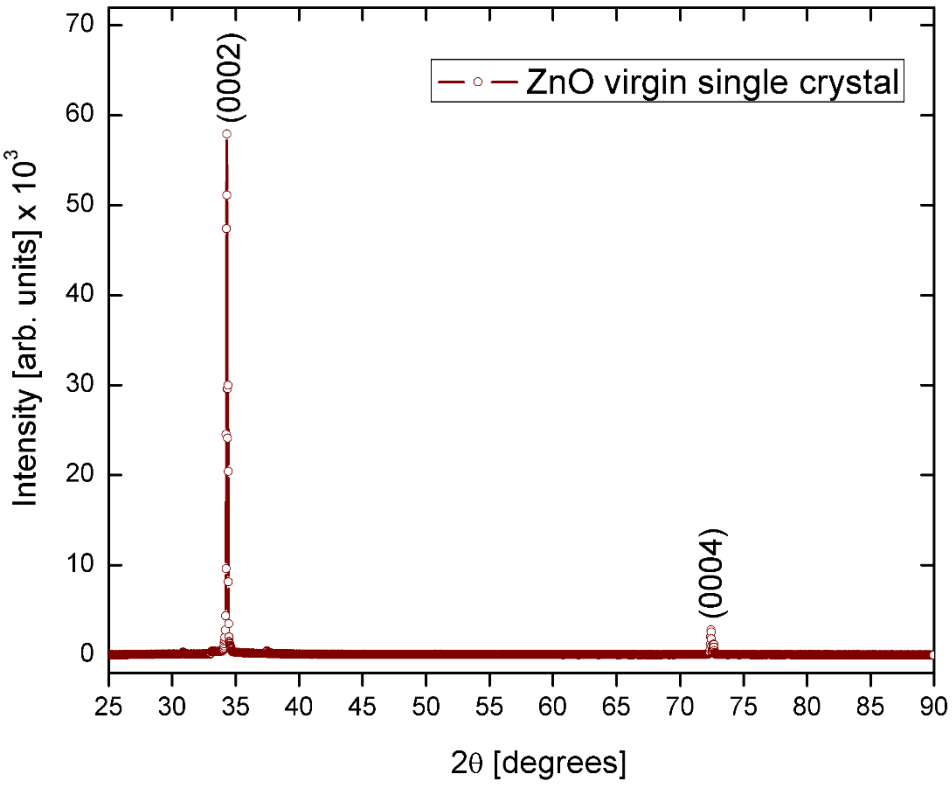


Figure 3.4: XRD patterns for ZnO single crystal.

In the case of single crystal ZnO, the 0002 and 0004 reflections are observed in the XRD pattern.

3.2. Material modification by ion implantation

Over the last few decades, ion implantation has proved to be a key processing step in material modification, in particular for its application in silicon integrated circuit (IC) technology. Most of the successes arise from its ability to circumvent solubility and diffusion limits compared with the conventional diffusion technique. Moreover, ion implantation is an attractive option for material fabrication because nearly all elements can be incorporated in a semiconductor matrix with precise control of concentration and depth distribution by varying the fluence and ion beam energy, respectively.

Radioactive $^{57}Mn^{*}$ implantations were carried out prior to on-line emission Mössbauer spectroscopy measurements at ISOLDE, CERN. Implantation energies of 50-60 keV were used on III-nitrides (AlN, GaN, InN) and ^{56}Fe pre-implanted ZnO samples with fluences in the order of 3.0×10^{12} ions/cm^2 at an implantation

angle (θ_i) of 60° relative to the crystal's surface determined by the experimental configuration at ISOLDE.

The implantation of stable ^{57}Fe, ^{56}Fe and ^{59}Co atoms on hydrothermally grown ZnO single crystals were carried out using the ROMEO implanter at the University of Jena. The stable implantations were performed at room temperature in an implantation chamber under vacuum with a pressure < 3×10^{-6} mbar with the samples tilted at an angle of 7° with respect to the direction of the ion beam to prevent channelling effects.

3.3. Implantation profiles, parameters and fluences

The implantation profiles were simulated with the Monte-Carlo method using 200 000 ions. SRIM-2011 which uses the stopping power version released in 2008 was employed in the calculation [69]. The implantation profiles, parameters and fluences are described in detail below.

3.3.1. $^{57}Mn^*$ in Nitrides and ZnO

The simulated implantation profiles for $^{57}Mn^*$ implanted in nitrides and ZnO at an implantation angle of 60° are shown in Figure 3.5.

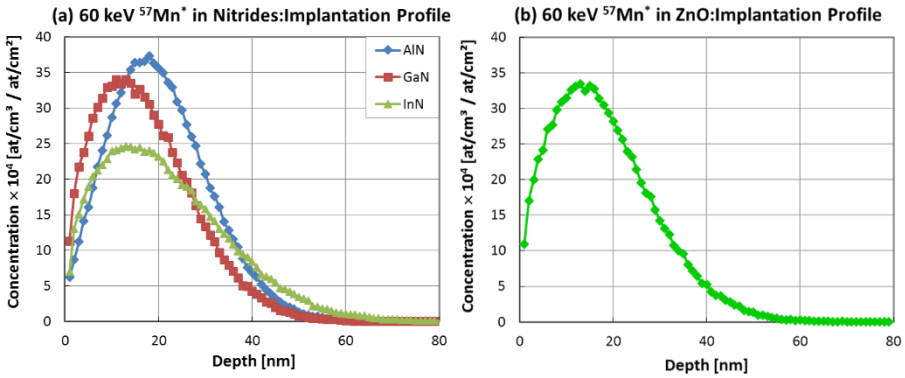


Figure 3.5: Implantation profile for $^{57}Mn^*$ in (a) nitrides and (b) ZnO at θ_i =60°.

The Gaussian profile for AlN shows a peak concentration of Mn ions at a depth of ~17 nm with a half width at half maximum (HWHM) linewidth of ~9 nm, while in GaN most Mn are expected to be located at ~14 nm from the surface of the sample with a profile linewidth of ~10 nm. For InN, a Gaussian profile with peak concentration of ions (P_c) expected at a penetration depth of ~15 nm and HWHM linewidth of ~12 nm. Mn dopants in the nitride films are located within a depth of

approximately less than 60 nm, which is within the thickness of the films of nitride sample used. A summary of other simulation results are presented in Table 3.2.

Table 3.2: Implantation simulation results from $^{57}Mn^{*}$ in III-nitrides and ZnO.

Material	Range (nm)			Straggling (nm)			P_c (nm)
	Average	Lateral	Radial	Average	Lateral	Radial	
AlN	19.9	33.4	34.9	10.4	35.7	12.5	~17
GaN	16.9	25.0	27.7	10.4	28.2	12.6	~14
InN	21.2	28.2	32.8	13.4	32.6	16.1	~15
ZnO	17.7	26.5	29.1	10.8	29.7	13.3	~15

3.3.2. ^{56}Fe pre-implanted ZnO samples

The implantation profile for ^{56}Fe with 60 keV ion energy is presented in Figure 3.6. The resulting Gaussian profile has a peak concentration at an implantation depth of ~27 nm and linewidth of ~20 nm. The implantation energy was chosen to match the energy used for $^{57}Mn^{*}$ implantation.

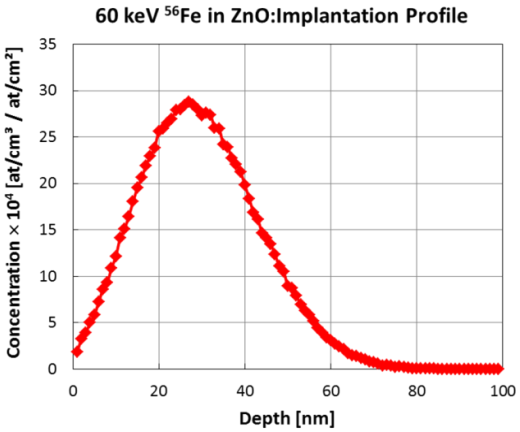


Figure 3.6: Implantation profile for ZnO implanted with ^{56}Fe.

3.3.3. "Box" Profile Samples

Two ZnO samples implanted with box profiles of ^{56}Fe and ^{59}Co samples were obtained by multiple implantations at different energies and lastly ^{57}Fe close to the surface in order to perform conversion electron Mössbauer spectroscopy. Thus, the implantation profiles were filled with ^{56}Fe and ^{59}Co at higher energies to obtain homogeneous doping up to 200 nm. This was followed by ^{57}Fe ions with an energy of 60 keV near the surface of the sample, with a peak concentration at ~27 nm from the sample surface, a depth within the detection limits of CEMS. In addition, the two different transition metals, Fe and Co were employed as dopants to investigate their effect on the expected magnetic properties.

3.3.3.1. ZnO:^{56}Fe+^{57}Fe

The simulated implantation profile for ZnO:^{56}Fe+^{57}Fe with different implantation energies for the respective isotopes are shown in Figure 3.7.

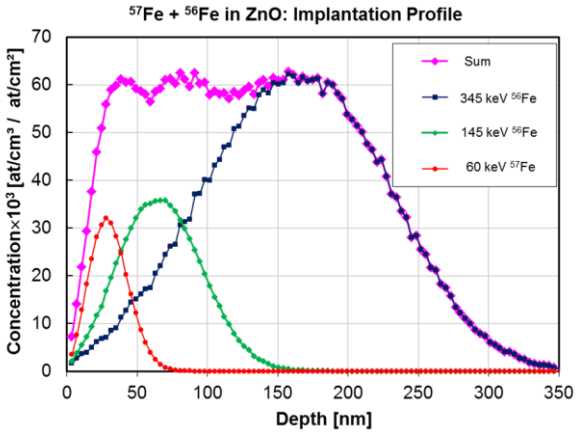


Figure 3.7: Implantation profile of ^{57}Fe and ^{56}Fe in ZnO.

The fluences were calculated to have 5×10^{15} ions/cm^2 of ^{57}Fe close to the surface and 4.58×10^{16} ion/cm^2 of ^{56}Fe resulting in an overall Fe fluence of 5.08×10^{16} ions/cm^2 but keeping the peak concentration below Dietl and co-workers' [19] prediction of ~ 5 at.%. The percentage atomic concentration is given by the expression,

$$C_{\text{at.\%}} = \frac{P_c \times \phi}{N_{\text{at.}}} \times 100\%, \qquad (3.1)$$

where P_c is the concentration in at./cm^3 obtained directly from the peak value of the implantation profile in Figure 3.7, ϕ is the implanted fluence in at./cm^2 and $N_{\text{at.}}$ is the number of atoms per unit volume. A final concentration of ~2.5 at.% was calculated using $N_{\text{at.}} = 8.3\times10^{22}$ at./cm^3 for ZnO.

3.3.3.2. ZnO:^{59}Co+^{57}Fe

Motivated by reports of ferromagnetism in Co implanted ZnO [127,128,129] and also to investigate the effect of a different transition metal, a sample with ^{59}Co instead of ^{56}Fe was prepared in a similar box profile and matching concentration of both dopants. The simulated implantation profile for ZnO:^{59}Co+^{57}Fe with different implantation energies for the respective isotopes are shown in Figure 3.8 (a) and the Fe/Co ratio as a function of implantation depth is shown in Figure 3.8 (b).

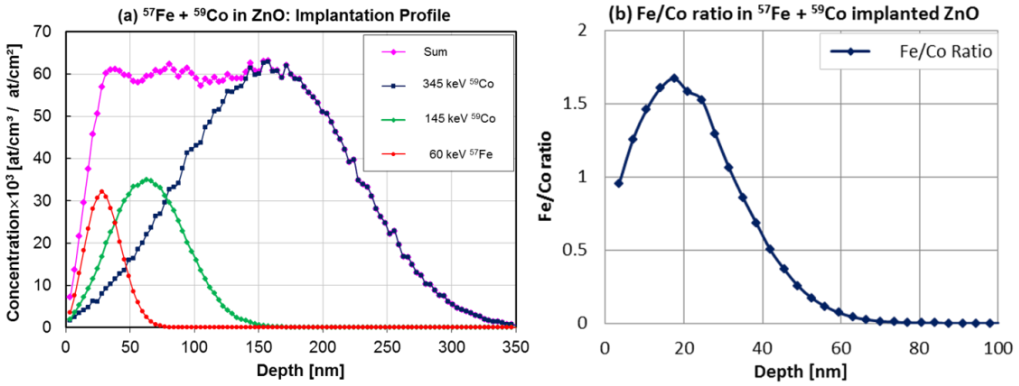


Figure 3.8: (a) Implantation profile for ^{57}Fe and ^{59}Co in ZnO and (b) Fe/Co ratio as a function of depth.

3.4. Mössbauer Spectroscopy

The Mössbauer effect can be used to study the properties of an absorbing nucleus and emitting nucleus. As a results, several Mössbauer spectroscopy approaches/techniques are employed depending on materials under investigation and application. The unique feature of Mössbauer spectroscopy is its ability to probe the location environment at an atomic scale, and in turn provide reliable information on the lattice sites, symmetry, charge states and magnetic interactions of the Mössbauer isotopes. In this study, conversion electron Mössbauer spectroscopy (CEMS) and emission Mössbauer spectroscopy (eMS) were employed and are discussed in detail in the following sections.

3.5. Conversion Electron Mössbauer Spectroscopy

CEMS is the most developed among scattering Mössbauer techniques because it provides a unique way for surface characterisation of solid materials. In this technique, the resonant absorption of the γ-rays occurs in the sample under study. The excited nuclei can de-excite back to the ground state by either emission of fluorescent photons or by emission of conversion electrons [179]. These conversion electrons have energies of a few keV resulting in a penetration depth of up to 100 nm and the depth information obtained in CEMS measurements depends on the energy of the electron detected. The emitted energy corresponds to the difference between the photon energy and the electron binding energy. The electron conversion process competes with the re-emission of γ-rays, and the ratio of their rates yields the conversion coefficient given by $\alpha_c = N_e/N_\gamma$, where N_e and N_γ are the numbers of the emitted electrons and photons, respectively. The larger the value of α_c (8.21 for ^{57}Fe and 5.1 for ^{119}Sn), the more effective the electron emission process [213].

The nuclear decay for ^{57}Co to ^{57}Fe and other several backscattering processes for the ^{57}Fe following resonant absorption of an incident gamma ray is shown in Figure 3.9. The K, L, M…core levels have distinct probabilities to contribute to internal conversion, but it is most likely to be prominent in the innermost (K) level because of the overlap between the electronic and nuclear wavefuctions. In the case of ^{57}Fe, the ejected K-conversion electron has a kinetic energy of 7.3 keV and leaves

behind a vacancy (hole) in the K level, which is then filled by an electron from a higher shell resulting in energy released either as X-rays or an Auger electron (i.e. a third electron being emitted for the same atom).

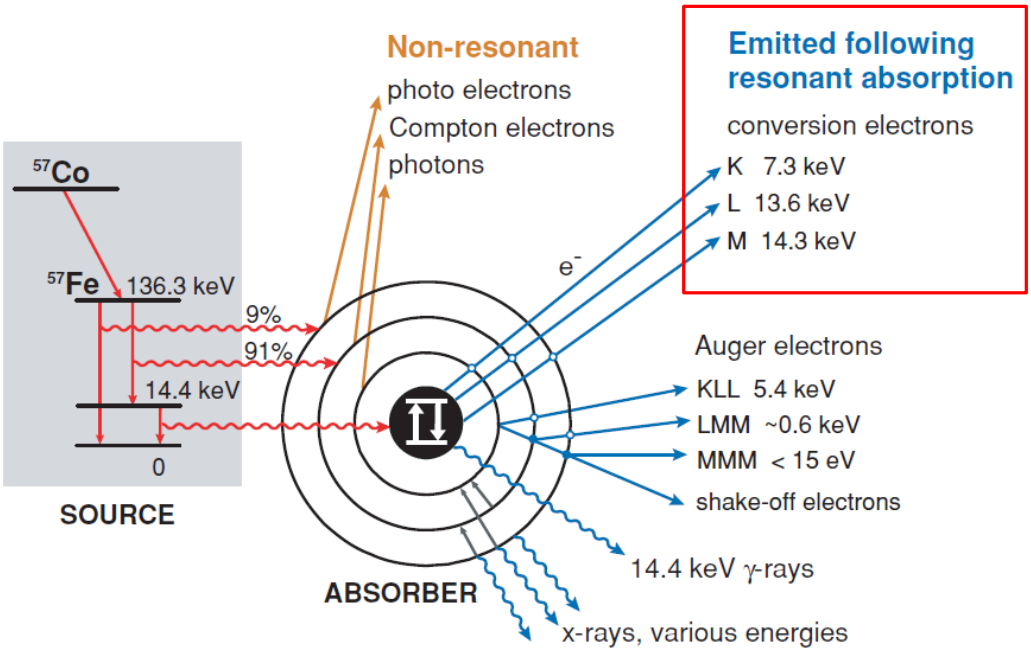


Figure 3.9: Decay scheme for ^{57}Co to ^{57}Fe and different backscattering processes for ^{57}Fe following resonant absorption of an incident γ-ray. [Adopted from Dyar *et al.* [189]]

3.5.1. CEMS Measurements and annealing conditions

Room temperature CEMS measurements using a standard ^{57}Co(Rh) source were carried out on the as-implanted ZnO:^{57}Fe+^{56}Fe and ZnO:^{57}Fe+^{59}Co samples and after annealing at temperatures of 773 K and 973 K. These samples were annealed for 30 minutes in a vacuum (with pressure < 10^{-6} mbar).

3.6. Emission Mössbauer Spectroscopy at ISOLDE

Emission Mössbauer spectroscopy utilizing radioactive precursor isotope ^{57}Mn* ($t_{½}$ = 1.5 min) produced at the ISOLDE, CERN as implantation probe atoms, which decays to ^{57}Fe have been used for studying magnetic properties, lattice locations and charge states of dopants in nitrides (GaN, AlN and InN) and ^{56}Fe pre-implanted ZnO crystal samples fluences of 2×10^{13}, 5×10^{13} and 8×10^{13} ions/cm^2. Use of short-lived radioactive isotopes presents a novel method where the sample under study act as a source of γ-rays after implantation.

3.6.1. Beam production

Radioactive $^{57}Mn^{*}$ beams are produced at the ISOLDE Facility, using a 1.4 GeV proton-induced nuclear fission in a uranium carbide (UC_2) target. $^{57}Mn^{*}$ atoms are subsequently ionised by a multi-frequency element specific laser irradiation system [214,215] (see Figure 3.10) and at the same time ^{57}Fe contaminants of up to 10^{10} ions/s in the beam are removed. The singly charged ions are then accelerated to energy of 50-60 keV before they are mass separated by magnets to produce pure radioactive $^{57}Mn^{*}$ ion beams with intensities $\geq 10^{8}$ s^{-1}, which are then directed to the implantation chamber. A beam spot area of 0.3 cm^2 corresponds to a flux of ~6.2×10^{8} $^{57}Mn^{*}/(cm^2\cdot s)$.

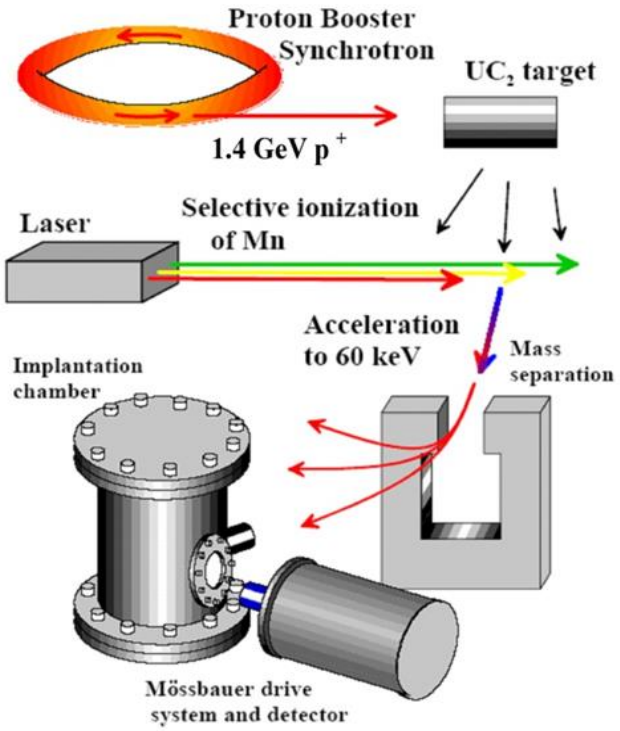


Figure 3.10: Beam production at ISOLDE.

3.6.2. Experimental set-up

The high vacuum implantation chamber, as illustrated in Figure 3.10, is connected by soft bellows to the $^{57}Mn^{*}$ beam-line system and is pumped to 10^{-6} mbar. A liquid N_2 cryostat system is connected to the implantation chamber for low temperature (77-300 K) measurements using a single position sample holder. A four position sample holder is used for high temperature measurements (300 – 700 K) to enable a series of measurements without breaking the vacuum. In the initial measurements, two sample holder positions were allocated for beam alignment, current optimisation and calibration purposes with an α-Fe foil. A beam of $^{57}Mn^{*}$ is directed through an empty sample position towards a Faraday cup to optimise the beam current which is achieved by varying the beam steering parameters on the ISOLDE

console. Figure 3.11 shows a picture of the experimental set-up and schematic view showing the beam direction, sample and detector arrangement with an emission angle of 60° relative to the normal of the crystal's *c*-axis.

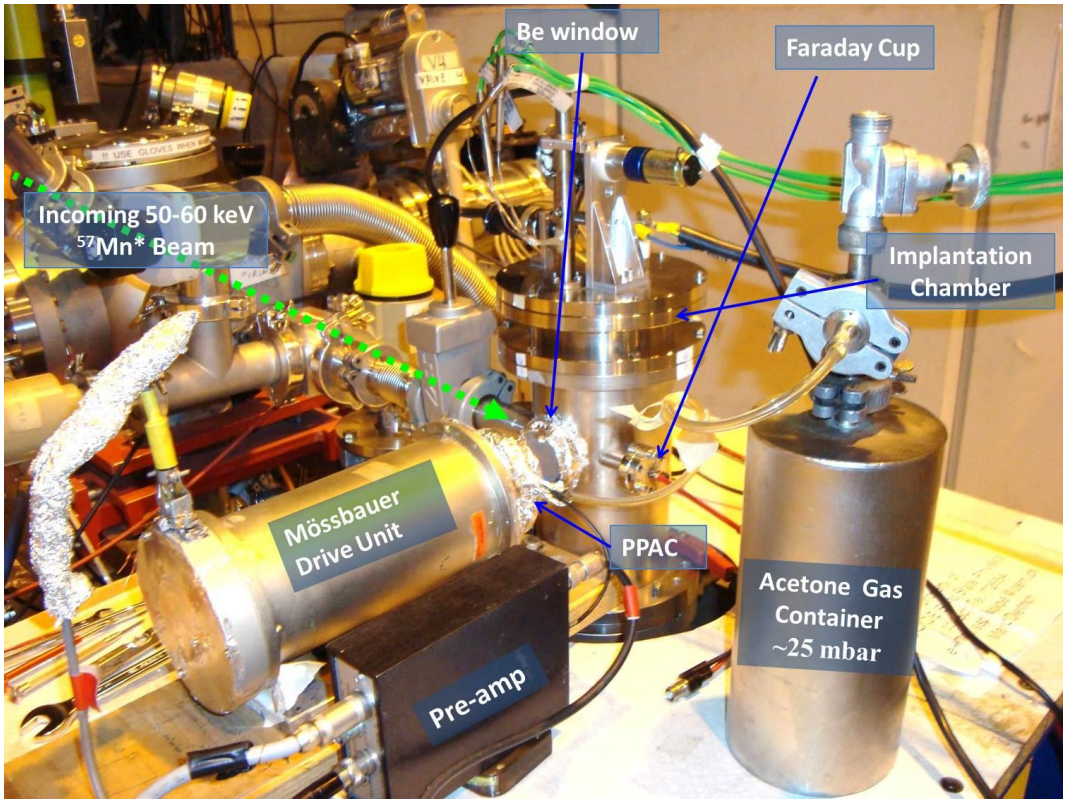


Figure 3.11: Pictorial image of the experimental set-up for emission Mössbauer spectroscopy at ISOLDE.

The Faraday cup is designed to collect charged particles, hence the number of $^{57}Mn^{*}$ ions striking the cup were used to determine the beam current. The second empty position is used for calibration; all hyperfine parameters are determined relative to an α-Fe spectrum measured at room temperature. An Osram halogen photo-optic lamp (15 V, 150 W) incorporated in the implantation chamber provides a rapid thermal annealing system with a temperature range up to approximately 800 K. A beryllium window is placed on the UHV implantation chamber facing the detector and acts as a filter for any radiation other than the 14.4 keV γ-rays. The parallel-plate avalanche counter [216] (PPAC) detector is mounted on the Mössbauer drive unit providing the Doppler velocity to record Mössbauer spectra of the emitted γ-radiation.

3.6.3. Resonance detectors

The resonance detectors utilised in this study makes use of the conversion electrons emitted from the surface of the absorbing material following the de-excitation of excited nuclei after resonant absorption of γ-rays. In CEMS, the sample under study is the absorber while in eMS, the sample is the source of γ-radiation and a single line absorber material is utilized in the detector.

3.6.3.1. ^{57}Fe enriched stainless steel detector

A. Design

A cross-sectional view of a PPAC is shown in Figure 3.12. The detector housing was made of Perspex; however, any material with a low atomic number such as aluminum may be used.

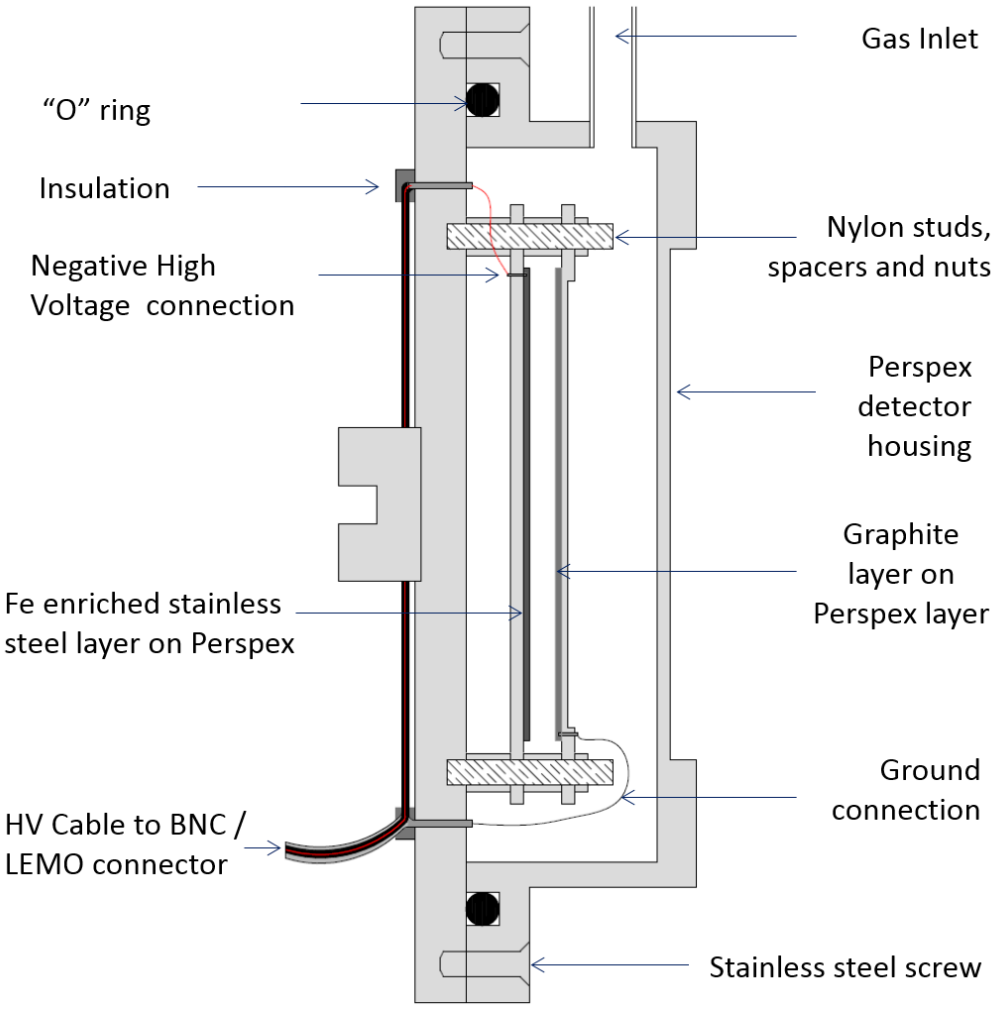


Figure 3.12: A cross-sectional view of a typical PPAC.

Inside the detector, two conductive parallel plates where a bias high voltage is applied to create a homogeneous electric field are incorporated. The electrical conductivity on the inner surfaces is achieved by spraying Perspex with graphite spray on one plate while on the other a single line resonance absorber material such as ^{57}Fe enriched stainless steel. The detector is connected to a gas reservoir usually containing acetone via a long thin plastic tube connected to the inlet. The light weight detector is driven by the Mossbauer drive during measurements and together with its accessories it is covered with an Al foil which reduces the cross-section for photo-electron production and shielding from external radio-frequency interference.

B. Principle of Operation

A bias voltage applied between the parallel plates results in a uniform electric field that repels the conversion electrons from the surface following the de-excitation of the excited nuclei. These conversion electrons ionises the gas atoms between the parallel plates causing the formation of *avalanches* - a shower of ionised particles. The resulting ionisations lead to further formation of more electrons and ions which in themselves cause further ionisations. Due to the presence of the electric field, cations will move towards the cathode while the electrons are attracted to the anode and counted. The beam current of ^{57}Mn* is relatively low compared to stable beams, hence these efficient PPAC detectors are used in data acquisition. These are fast and insensitive to γ- or X-ray background radiation, i.e. the signal to background ratio is high [217]. In addition, PPAC detectors have a relatively high time resolution in the order of nanoseconds (10^{-9} s), thus high count rates can be tolerated. The detector is an acetone gas-filled (pressure of 25 mbar) resonance counter equipped with enriched stainless steel. In the ^{57}Fe enriched stainless steel, ~ 90% of the γ-radiation is transmitted and this motivated the development of a new detector based on multiple plates of FeAl deposited on a beryllium substrate to increase the detection efficiency. The development of the FeAl detector, preliminary tests, and future work are discussed in Appendix B.

3.6.3.2. CEMS Detector

A CEMS detector is also gas operated, similar in design and principle as a PPAC. The only difference is that the sample under study is incorporated inside the detector, mounted on an aluminised Mylar foil which replaces the single line absorber. The acetone vapour was pumped to pressures of ~40 mbar and operating voltages in the range of ~600-800 V were used. A combination of 10%CH_4:90%He can also be used as a counting gas.

3.6.4. Mössbauer electronics

The experimental set-up and the electronics for Mössbauer spectroscopy at ISOLDE are shown in Figure 3.13.

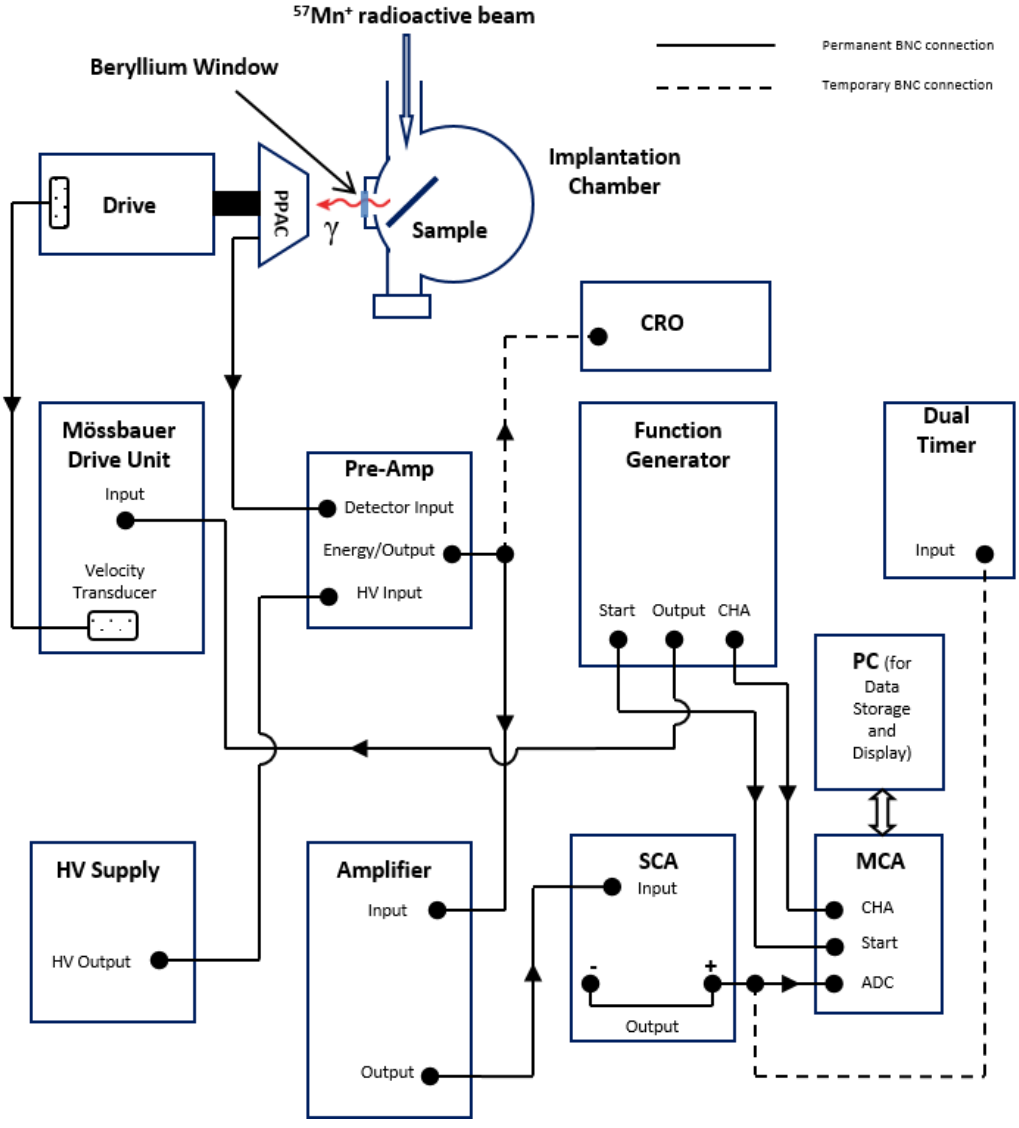


Figure 3.13: Schematic diagram of the experimental set-up and electronics [177] at ISOLDE.

The pulses from the detector are pre-amplified, then amplified and sent through a single channel analyser (SCA) or discriminator which cuts out the non-resonant background radiation and detector/pre-amplifier noise. The selected pulses are finally fed into a multichannel analyser (MCA) operating in multichannel scaling (MCS) mode where several hundreds of channels are synchronised with the velocity of the Mössbauer drive unit (MDU) making use of the feedback control system through the function generator (FG). The FG supplies a reference signal which determines the waveform of the source. Apart from the analogue signal, the FG also provides two digital control pulses (*Start* and *Channel Advance – CHA*), which are utilised to synchronise the MCA. The *Start* pulse resets the MCA and opens the first data register to accept counts. Pulses from the SCA which arrive while the register is open are accumulated to the current contents. The current register closes and the next one opens every time each successive *CHA* pulse arrives [187]. Thus, the arriving pulses are collected and placed in a register that corresponds to a particular drive velocity. When a complete waveform has been generated (usually 512 channels), a new *Start* pulse is sent and the process is repeated. The MCA can be a separate module or a card incorporated inside a computer, which provides data storage and spectra display.

3.6.5. eMS measurements

The beam-sample-detector geometry shown in Figure 3.13 was used for eMS measurements. The sample was mounted on a holder placed at an angle of 30º with respect to the beam line, resulting in γ-ray emission angle (θ_γ) of 60º with crystal's *c*-axis.

$^{57}Mn^{*}$ ions of 50-60 keV energy were implanted at ambient temperatures with fluences up to 10^{12} ions/cm^2 into the materials under study. Following implantation, low temperature (77 K) measurements and measurements during an annealing sequence (300-700 K) were then performed on a wide velocity scale of ±12 mm/s to obtain information from the 'wings' of the spectra. The low fluences were employed to ensure that precipitation and overlapping damage cascades are effectively ruled out. The half-life of $^{57}Mn^{*}$ (1.5 min) is sufficient to allow for the annealing of the radiation damage to occur at increasing temperatures, before Mn

decay and subsequent measurement of the ^{57}Fe Mössbauer spectra. The excited ^{57}Mn* state decays directly to the 14.4 keV state of ^{57}Fe with 80% probability. A mean recoil energy of 40 eV is imparted to the ^{57}Fe atoms [218].

Angular dependent measurements were carried out with the spectra collected at $\theta\gamma = 0^{o}$ and 60^{o}. For measurements at $\theta_{\gamma} = 0°$, the samples were first implanted for 4 minutes at $\theta_{I} = 60°$ with respect to the sample's surface, and thereafter rotated to face the detector and a new spectrum was recorded during the decay of ^{57}Mn* for 4 minutes after the implantation. This process was repeated several times to obtain data with sufficient statistics. A narrow velocity scale of ~ ± 4.5 mm/s was selected to investigate any anisotropy effects in the central region of the spectra and to perform more detailed analysis in order to determine the nature of the lattice sites of the probe ions. The measurements discussed in this report were performed using a ^{57}Fe-enriched stainless steel detector.

3.6.6. Comparison of strengths and weaknesses of Mössbauer spectroscopic approaches

The advantages of online eMS over CEMS, conventional transmission Mössbauer spectroscopy (TMS) and in-beam Mössbauer spectroscopy (IBMS) were discussed in a previous research report [177]. Emission Mössbauer spectroscopy presents a novel technique of using the sample under study as the source of γ-radiation offering high sensitivity to the atomic information in the vicinity of the probe atoms. Furthermore, the advantage of the eMS technique when short-lived radioactive isotopes are utilised allows for a spectrum to be recorded in 5 to10 minutes as compared to ~24-36 hours necessary when the IBMS method is applied. A spectrum collected by the CEMS approach requires an average of 10 days. These three techniques and the time required for data acquisition depends on the sample being measured. Moreover, eMS allows for studies in extremely dilute systems (10^{12} ions/cm^{2}), while fluences above 10^{15} ions/cm^{2} are required for CEMS measurements with a 50 mCi source. As a result, these approaches have been chosen systematically for different investigations in the fluence regimes within this project. On the other hand, CEMS allows effective standalone studies of fluence dependence and offline annealing in implanted samples without increasing the

concentration in the sample as compared to online eMS measurements. In addition, a very important aspect of $^{57}Mn^{*} \rightarrow {}^{57}Fe$ eMS experiments is the half-life of 1.5 minutes for the $^{57}Mn^{*}$ state which allows effective annealing of the lattice and diffusion to occur before the Mössbauer decay unlike in IBMS where the effective time for thermal treatment is the lifetime of the 14.4 keV Mössbauer state (100 ns). Furthermore in online eMS, radiation damage created during implantation can be annealed during the measurement.

3.7. Vibrating Sample Magnetometer

The magnetisation of ferromagnetic materials can be investigated in a number of ways. These include, techniques based on the detection of the dipole field, the force method, or the induction method. In dilute magnetism studies, techniques such as superconducting quantum interference device (SQUID), vibrating sample magnetometer (VSM) and recently X-ray magnetic circular dichroism (XMCD) a synchrotron based technique are utilised. In the current study, VSM, a simple and effective system pioneered in the late 1950s by S. Foner [219] serves as an excellent tool for exploring magnetic properties of doped semiconductor materials. It is used to measure the magnetic moment and hence the magnetic dipole moment in the presence of a slowly changing or static magnetic field [220].

3.7.1. Principle of operation

VSM is based on Faraday's Law of induction in which an electromotive force (*emf*) is induced in a conducting material by a time varying magnetic flux. The principle lies on the detection of induced *emf* in a coil wire given by the relation:

$$\varepsilon = -N\frac{d}{dt}\left(BA\cos\theta\right), \tag{3.2}$$

where, N is the number of turns in the coil, A - the coil turn area and θ - the angle between the direction normal to the surface the applied magnetic field (B).

A sample under investigation is placed at the lower end of a long rigid rod which is mechanically driven such that it oscillates vertically by a transducer identical in design to a loudspeaker. The rod is positioned between the pole pieces of an electromagnet to which detection coils are mounted. Thus the sample is vibrated at

small fixed amplitudes with respect to stationary pick-up coils in a homogenous external magnetic field produced by an electromagnet. The pick-up coils measure the induced magnetic flux and a resulting variable signal is proportional to the magnetic moment of the material under study and also to the vibration frequency and amplitude. The induced signals are fed to a differential amplifier to compensate for variations in amplitude and frequency of oscillations [221,222]. In addition, a lock-in amplifier with phase-sensitive detection (synchronous detector) coupled to a low pass filter generates a direct current output signal that purely depends on the induced magnetic moment from the specimen [220]. Figure 3.14 shows a cross-section of a typical vibrating sample magnetometer.

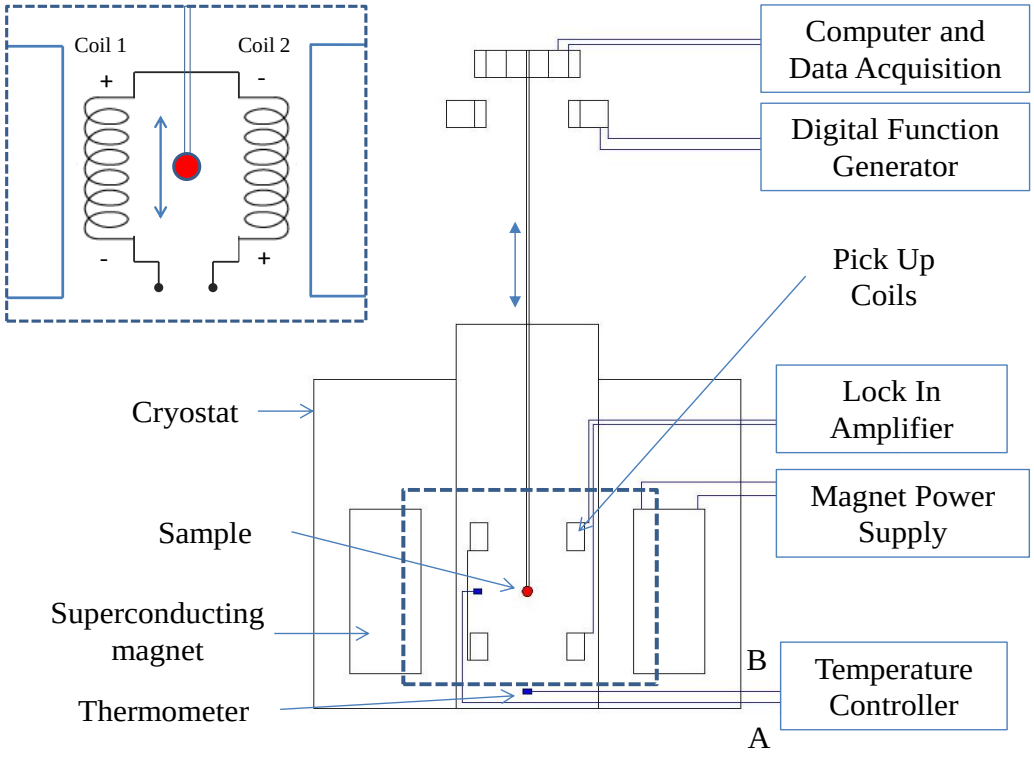


Figure 3.14: Cross-sectional view of a VSM system with insert showing the working principle.

The pick-up coils are matched and connected in opposite sense (see insert in Figure 3.14), such that in the absence of a sample the overall induced voltage is zero. This is because the external magnetic field is induced in equal and opposite directions. When the sample is in upward motion, it causes an increase in the flux through the upper pick-up coils and a decrease in the flux through the pick-up coils. The reverse is consistent with the downward motion of the specimen. As a result,

the overall voltage induced when the sample is oscillating is proportional to twice the divergence of the ***B*** field.

3.7.2. VSM measurements

In this report, the VSM system was used to investigate the magnetic properties of implanted ZnO samples as function of measuring temperature (T_m) at 4 K and 293 K after heat treatment in a vacuum for 30 minutes at an annealing temperatures of T_A = 973 K. In addition, magnetisation curves of a virgin ZnO sample were also measured at both measuring temperatures and used for subtracting the diamagnetic component form the data.

3.8. Summary of measurements

Several Mössbauer spectroscopy studies have been reported mainly in GaN [96,104,110,111] and ZnO [116,118,169,117,130] using ^{57}Fe, covering the range of fluences of 1-8 at.%. As a result different approaches were employed in preparing samples to investigate the magnetic properties with the aim of not repeating similar experiments as reported in literature. In the current study, stable elements and radioactive precursor isotopes of transition metals mainly ^{57}Fe, ^{56}Fe and ^{59}Co implantations were carried out on ZnO and/or nitrides semiconductors for different studies and for specific experimental techniques. Three different approaches were employed to investigate the effect of dopants with respect to the possible magnetic properties in doped ZnO and/or nitrides:

a) Radioactive pre-cursor isotope ^{57}Mn* which β-decays to ^{57}Fe for online emission Mössbauer spectroscopy measurements at ISOLDE, CERN was mainly utilised for III-nitrides. The fluence range is of the order of ~3×10^{12} ions/cm^2 resulting in extremely dilute systems with a concentration of ~10^{-4} at.%, eliminating the possibility of precipitation/clustering.

   Online eMS measurements were carried out as a function of temperature to investigate the lattice sites, annealing behaviour and relaxation effects of the paramagnetic Fe^{3+} ions. The results were also compared with stable ^{57}Fe implantation in similar materials, mainly GaN and a comparison of relaxation rates in oxides from similar studies.

b) Stable ^{57}Fe implantation and co-doping with ^{56}Fe and ^{59}Co in ZnO for CEMS and VSM experiments. The implantations were carried out with different ion energies to achieve homogenous concentrations of transition metal elements in the sample. ^{56}Fe was used to increase the concentration of iron in the sample and to investigate the effect of fluence on the magnetic properties, while co-doping with ^{59}Co was used to study the effect of introducing a different transition metal motivated by reports on ferromagnetic behaviour in Co implanted ZnO [127,128,129]. CEMS measurements were performed on the as-implanted and annealing up to 973 K. Magnetisation measurements were performed on the annealed samples at low temperature (~4 K) and close to room temperature (~293 K).

c) The third approach utilised both stable and radioactive isotopes; three ZnO samples were initially modified by pre-implantation of ^{56}Fe with different fluences (2×10^{13}, 5×10^{13} and 8×10^{13} ions/cm^2), followed by eMS measurements after implantation of radioactive ^{57}Mn*. The objective was to investigate the effect of Fe concentration on the relaxation rates, the fractional contribution of paramagnetic Fe^{3+} to the Mössbauer spectra and to correlate the results with similar studies in virgin and other pre-implanted ZnO samples.

The details of the samples prepared by ion implantation are listed in Table 3.3 while the analysis of the data obtained from eMS, CEMS and VSM measurements and the results are presented in the next chapter.

Table 3.3: List of samples prepared by ion implantation and measurements conducted.

	Material	Implanted Species	Fluence (ions/cm^2)	Implantation Energy (keV)	Implantation Angle (^{o})	Temperature (K)	Sample Name/Identifier	Measurements performed
1	**GaN**	$^{57}Mn^*$	~3×10^{12}	50	60	100-800K	**GaN**	Online eMS measurements as a function of temperature and angle.
2	**AlN**						**AlN**	
3	**InN**						**InN**	
4	**ZnO**	^{56}Fe	3.6×10^{16}	345	7	RT	**ZnO:^{57}Fe+^{56}Fe**	CEMS as-implanted samples and after annealing and VSM.
		^{56}Fe	1.0×10^{16}	155				
		^{57}Fe	5.0×10^{15}	60				
5	**ZnO**	^{59}Co	4.1×10^{16}	345	7	RT	**ZnO:^{57}Fe+^{59}Co**	CEMS on as-implanted and after annealing and VSM.
		^{59}Co	1.2×10^{16}	145				
		^{57}Fe	5.0×10^{15}	60				
6	**ZnO**	^{56}Fe	2.0×10^{13}	60	7	RT	**ZnO:^{56}Fe2**	Online eMS as a function of temperature.
		$^{57}Mn^*$	~3×10^{12}	50	60	300-800K		
7	**ZnO**	^{56}Fe	5.0×10^{13}	60	7	RT	**ZnO:^{56}Fe3**	Online eMS as a function of temperature.
		$^{57}Mn^*$	~3×10^{12}	50	60	300-800K		
8	**ZnO**	^{56}Fe	8.0×10^{13}	60	7	RT	**ZnO:^{56}Fe8**	Online eMS as a function of temperature.
		$^{57}Mn^*$	~3×10^{12}	50	60	300-800K		

NB:

- Radioactive $^{57}Mn^*$ was implanted during online eMS measurements, while stable isotopes were separately pre-implanted before CEMS and VSM measurements.
- Implantation angles are measured relative to the implanted sample surface (not the crystal's *c*-axis as in emission angles).

Chapter 4

Analysis, Results and Discussion

This chapter focuses on the analysis and interpretation of the data obtained from the following measurements:

a) Online emission Mössbauer spectroscopy (eMS) on nitrides (GaN, AlN and InN) films and ^{56}Fe pre-implanted ZnO single crystals following ^{57}Mn* implantation at ISOLDE/CERN. Measurements were performed as a function of temperature and emission angles.

b) ^{57}Fe conversion electron Mössbauer spectroscopy (CEMS) on two ZnO samples implanted with ^{57}Fe and box profiles of ^{56}Fe and ^{59}Co: (i) ZnO:^{57}Fe+^{56}Fe and (ii) ZnO:^{57}Fe+^{59}Co. The experiments were performed on as-implanted samples and after annealing at 773 K and 973 K for 30 minutes in a vacuum.

c) Vibrating sample magnetometer (VSM) measurements on ZnO single crystals implanted with stable isotopes to investigate any magnetic properties on the bulk samples after annealing. Measurements were carried out as a function of applied magnetic field of ±1 T at measuring temperatures (T_m) of 4 K and 293 K.

4.1. eMS measurements on nitrides

This section describes the analysis procedures and results eMS data collected on GaN, AlN and InN samples. Measurements were undertaken at a γ-emission angle (θ_γ) of 60^o relative to the sample's *c*-axis as a function of temperature over a velocity range of ±12 mm/s. In addition room temperature data were collected in a narrow velocity scale of ±4.5 mm/s[a] to investigate any angular dependence in the central region of the spectra.

[a] "mm/s" is the convenient Mössbauer unit and for ^{57}Fe, 1 mm/s = 4.8×10^{-8} eV

4.1.1. Analysis and Results: GaN

The emission Mössbauer spectrum obtained at 300 K for the GaN film grown on a sapphire substrate following $^{57}Mn^{*}$ implantation is shown in Figure 4.1 (a). The central region of the spectrum was analysed with three doublets labelled D1, D2 and D3. In addition, the spectrum revealed magnetic structure in the 'wings' the spectrum, a zoomed in view is shown in Figure 4.1 (b). The magnetic structure was analysed in terms of two sextets labelled BT1 and BT2. The choice of these spectral components and fitting procedure are discussed below.

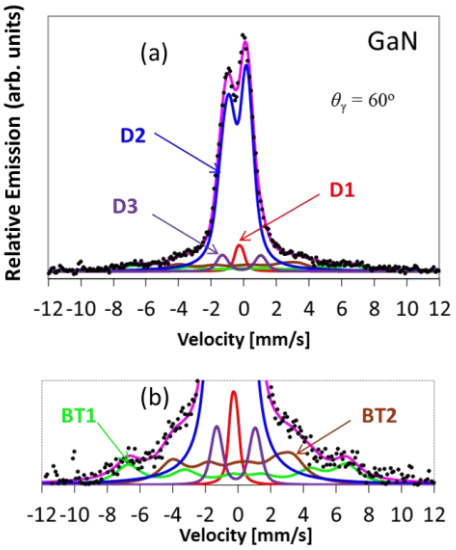


Figure 4.1: (a) Emission Mössbauer spectrum of GaN obtained at 300 K and at an emission angle of 60° and (b) zoomed-in view of the two BT sextets used to analyse the magnetic structure in (a).

Angle dependence measurements were carried out on a narrow velocity scale of ±4.5 mm/s to ascertain the nature of the site location of the dopants. Room temperature spectra recorded at emission angles of 60° and 0° are presented in Figure 4.2.

The change in the relative intensities of the two legs of the spectra at the measured emission angles indicates that the probe ions are located on regular crystalline sites. This observation is in disagreement with the results obtained for cubic III-V's [172,173] where Fe in isolated damaged regions dominated the spectra below room temperature, attesting to the radiation hardness of GaN. The central region of the GaN spectra was initially fitted using two

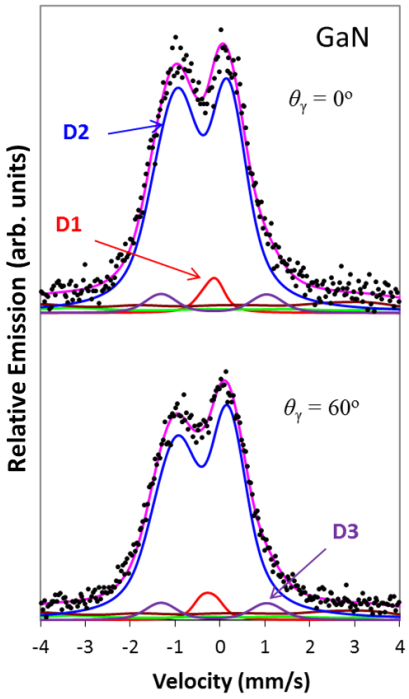


Figure 4.2: Room temperature ^{57}Fe emission Mössbauer spectra obtained after implantation of $^{57}Mn^{*}$ into GaN at emission angles of 0° and 60° relative to the sample *c*-axis.

asymmetric quadrupole split doublets, D1 and D2 as guided by the observed angular dependence. A description of the analysis strategy for the two components is given below:

- An asymmetric doublet (D1) with intensity ratio (I_π/I_σ) = 0.88 and 3.0 for $\pi_{(\pm1/2\rightarrow\pm3/2)}$ and $\sigma_{(\pm1/2\rightarrow\pm1/2)}$ transitions is given by equation 2.24 for an emission angle of 60^o and 0^o.
- A two segment quadrupole split doublet/distribution which allows for free coupling between the isomer shift and quadrupole splitting was used in the analysis of D2. The variables are related by the expression:

$$\delta = \delta_0 + \delta_1 \cdot \Delta E_Q, \tag{4.1}$$

where δ_0 was fitted as a free parameter while δ_1 as a global parameter and ΔE_Q is the average quadrupole splitting. A global parameter is a temperature independent variable which is applied in data analysis. The sign and direction of V_{zz} determines which 'leg' of the asymmetric quadrupole doublet is more intense. A scaled dependence, $f_{obs}(\theta)$, is observed for the two segment quadrupole distribution irrespective of how the electric field gradient (EFG) crystal symmetry axes are related. The scaled dependence is described by the equation:

$$f_{obs}(\theta) = Q \cdot [f(\theta) - 1] + 1, \tag{4.2}$$

where, $f(\theta)$ is ratio of the intensities the two legs of a typical asymmetric doublet between the $\pi_{(\pm1/2\rightarrow\pm3/2)}$ and $\sigma_{(\pm1/2\rightarrow\pm1/2)}$ given by the equation 2.24. Q is a fitting parameter which represents a scaling factor for the observed angle dependence of the two-segment quadrupole spilt doublet, with values ranging from 0 to 1 and gives a measure of the asymmetry of this doublet. Q = 0 results in the polycrystalline case whereas Q = 1 yields a single crystalline case with full polarisation. A Q value of 0.08(1) was determined from the analysis of the GaN spectra.

In addition, a third asymmetric doublet (D3) was required to fit the data in the final analysis. This spectral component showed no angular dependence and its physical significance will be discussed in subsequent sections in this chapter.

The magnetic feature observed in the wings of the spectra for GaN is similar to results obtained in oxides [150,151,152,153] characteristic of paramagnetic Fe^{3+} (S=5/2) showing long spin-lattice relaxation times. In a non-cubic crystal field, the ^6S ground state of Fe^{3+} splits into three Kramers doublets with S_z = ±5/2, ±3/2, and ±1/2 and each of the three doublets produces its own unique Mössbauer sextet with the resultant effect yielding a complicated summed spectrum [162,223,224]. In this study, the magnetic structure was analysed using a semi-empirical relaxation model utilizing Blume-Tjon (BT), where, the number of sextets required to fit a spectrum is a measure of the 'sharpness' of the spectral features and information on the strength of the magnetic hyperfine field (B_{hf}) [150] is obtained. The BT line shape contains six lines with intensities given by the ratio 3:2:1:1:2:3 and a constant experimental linewidth determined by the intrinsic linewidth of the detector and geometrical broadening resulting from the experimental set-up. Moreover, it has an additional line broadening (ΔΓ) with units of mm/s describing the relaxation effects. According to Blume and Tjon [225], the line broadening for Mössbauer spectra showing relaxation effects can be approximately determined from the equation,

$$\Delta\Gamma = \frac{2\hbar c}{E_0}\tau^{-1}, \qquad (4.3)$$

where E_0 is the Mössbauer transition energy, $\hbar$ is the reduced Planck's constant, and c is the speed of light. As a result, with increasing temperature and in turn the increase in the line broadening from which the spin-lattice relaxation rates can be determined. A simulation of the relaxation spectra with the indicated relaxation times assuming a hyperfine field of ±50T is shown in Figure 4.3. As the relaxation rate increases, the sextets

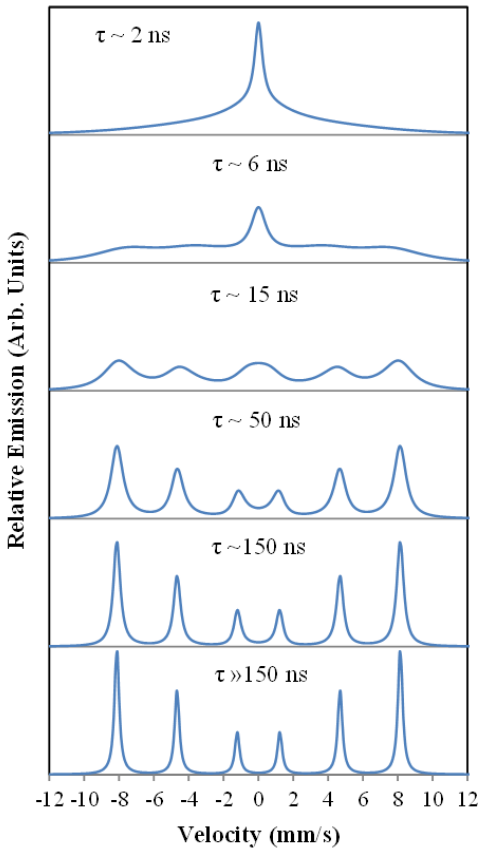


Figure 4.3: ^{57}Fe Mössbauer spectra simulated with Blume-Tjon model using hyperfine field of ±50 T at relaxation time indicated.

start to collapse in pairs beginning with the inner most lines. This is because the Larmor precession time for the outer lines is shorter than that for the inner lines, since (τ_l) is proportional to the energy difference between spectral lines.

The final spectral fitting was performed simultaneously using a set of macros in Vinda [226] in an iterative procedure taking advantage of the temperature dependent appearance and disappearance of fitted spectral components for their unequivocal identification in addition to the observed anisotropy of the central region and magnetic features on the wings.

The isomer shift of D1 showed a temperature dependence consistent with the second-order Doppler shift was restricted to follow this trend with temperature while the quadrupole splitting showed a minor variation with temperature and was fitted as a global parameter, (fitted a constant parameter on individual data sets linked to a program file in Vinda) over the measured temperature range. For the D1 spectral component a Voigt line shape with a fixed Lorentzian linewidth was utilised in the analysis with a Gaussian broadening fitted as a global parameter since no temperature dependence of the Gaussian broadening was observed. The complex Voigt model was applied to investigate the possibility of line broadening and effectively to determine any temperature dependence of various hyperfine interaction parameters in order to properly assign them to their Fe lattice position or configuration.

The hyperfine parameters of D2 and D3 and the area contribution of all the central components were fitted as free parameters to effectively monitor their temperature dependence.

In light of the semi-empirical model describe above, the magnetic structure on the wings of the spectra for GaN was analysed with two Blume-Tjon (BT1 and BT2) sextets. The isomer shifts of the two sextets were restricted to follow the second order Doppler shift with temperature while the quadrupole shifts (ϵ_Q) were fitted simultaneously as a global parameter based on the non-temperature dependence of high spin Fe^{3+}. The total area of the BT sextets was fitted as a free parameter, but the relative area ratios of the sextets were fitted as global variables. The temperature

dependence of the line broadening of the BT sextets was also set as a free parameter, from which the relaxation rates were calculated according to equation 4.3. A complete temperature series spectra for GaN measured at temperatures between 100 K and 730 K and at emission angles of θ_γ = 60° is presented in Figure 4.4 together with fitted components. The temperature dependence of the magnetic structure observed in the spectra over the measured temperature is discussed later in this section.

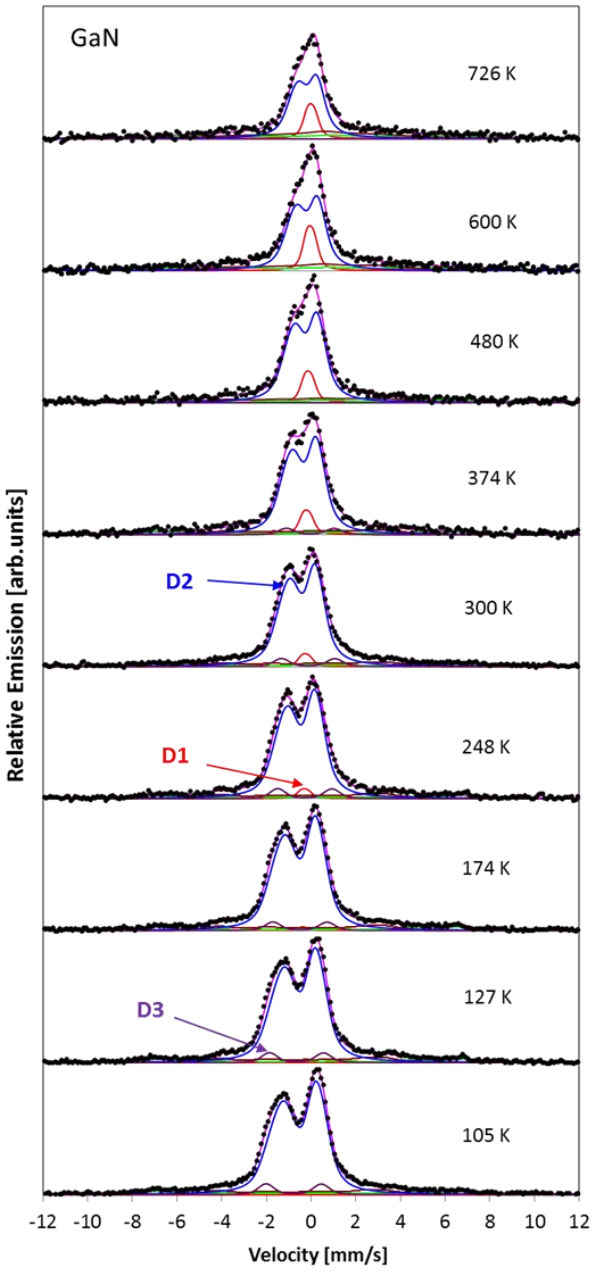


Figure 4.4: **^{57}Fe emission Mössbauer spectra obtained after implantation of ^{57}Mn* into GaN at the temperatures indicated and θ_γ = 60°.**

The extracted hyperfine parameters for the fitted spectral components extracted at room temperature are presented in Table 4.1.

Table 4.1: Room temperature hyperfine parameters obtained for Fe implanted in GaN.

	D1	D2	D3	BT1	BT2
B_{hf} [T]	-	-	-	41.2(2)	22.8(3)
δ (mm/s)	0.25(2)	0.41(1)	0.14(2)	-0.18(3)	0.02(4)
ΔE_Q / ϵ_Q (mm/s)	-0.30(3)	1.21(2)	2.35(3)	0.62(3)	
Γ (mm/s)	0.34	0.68	0.38(3)	1.51(4)	
$\sigma_L(\delta)$ (mm/s)	0.12(3)	-	0.26(2)	-	-
$\sigma_R(\delta)$ (mm/s)	-	-	0.27(1)	-	-

In the Blume-Tjon sextets, the linewidth of 1.51(4) mm/s shows appreciable broadening relative to the experimental linewidth of ~0.50 mm/s, which may be attributed to the inhomogeneity of the environment of the Fe probe atoms in the sample and/or due to a distribution of hyperfine fields. It has been observed that when the spin relaxation rate is in the range, $10^6 \leq \tau^{-1} \leq 10^9$ s^{-1}, the observed Mössbauer line width increases compared to the experimental linewidth [162].

4.1.1.1. Lattice site assignments

The spectral component, D1 is characterised by isomer shift and quadrupole splitting values of δ = 0.25(2) mm/s and ΔE_Q = -0.30(3) mm/s, which is at variance with transmission Mössbauer spectroscopy results of Alves *et al.* [104] who obtained respective values of 0.12 mm/s and 0.52 mm/s. The authors assigned this component to Fe atoms on substitutional Ga sites. Moreover, as highlighted earlier, the as-implanted CEMS spectra for Fe implanted reported by Talut *et al.* [110] was analysed with two doublets; D_{III} (δ = 0.42 mm/s, ΔE_Q = 0.48 mm/s) and D_{IV} (δ = 0.59 mm/s, ΔE_Q = 0.71 mm/s) and a single line (δ = -0.05 mm/s). The single line was assigned to either superparamagnetic α-Fe or to paramagnetic γ-Fe, while the doublets were assigned/attributed to Fe^{3+} with three and four nearest N neighbours, respectively. In light of the observed angular dependence in the central region of the spectra collected at room temperature, in this study, different analysis models were employed. As a result, different hyperfine parameters from studies reported by Alves *et al.* [104] and Talut *et al.* [110] were obtained and consequently

different interpretation of the lattice location and/or chemical nature of spectral components were given. The isomer shift of 0.25(2) mm/s for D1 suggest Fe(III).

The quadrupole splitting for this component has been determined to be -0.30 mm/s. In emission geometry, $\Delta E_Q < 0$, suggests that the right 'side' of an asymmetric doublet is more intense than the left at small angles ($\theta_\gamma < 54.7^o$). This is consistent with the differences in the intensity ratios of 3.0 and 0.88 obtained at the measured angles of 0^o and 60^o, respectively obtained from equation 2.24. However, from visual inspection of the GaN spectra, the spectral components are not easily distinguishable because of the small quadrupole splitting value. The observed negative quadrupole splitting may be explained by a more negative valence contribution compared to the lattice contribution, since the principal axis originates from both charges on partially filled valence orbitals and the neighbouring ions of the probe atom. The angular dependence observed in the AlN spectra described in the next section clearly shows this effect. A relatively small quadrupole splitting value of -0.30 mm/s is expected in a wurtzite structure (space group $P6_3mc$); where the site point symmetry is lower than cubic. According to the observed anisotropy and hyperfine parameters, D1 is tentatively assigned to covalently bonded Fe(III) residing on a Ga site (Fe_S), tetrahedrally coordinated to 4N atoms.

The hyperfine parameters of $\delta = 0.41(1)$ mm/s and $\Delta E_Q = 1.21(2)$ mm/s have been extracted for the spectral component, D2. The isomer shift is more positive compared to the Fe_S, $\delta = 0.25(2)$ mm/s which corresponds to a decrease in the *s*-electron density at the probe nucleus. This suggests some relaxation of the bonding between the Fe ions and the surrounding lattice atoms. Furthermore, a relatively high quadrupole splitting with respect to Fe_S reflects a loss of tetrahedral symmetry around the Fe probe atom. In addition, because of the observed angular dependence, it is assigned to Fe atoms on regular crystalline sites (Fe_C) associated with vacancy type defects. However, the isomer-shift is consistent with Fe^{2+} (S=0, S=1), Fe^{1+} (S=1/2) or Fe^{3+} (S=5/2). The Fe^{3+} high spin state is the only state that can be excluded from describing the central part of the spectra based on the temperature dependence of the quadrupole splitting. Moreover, depending on the orbitals, Fe^{2+} (S=0) could also be excluded. Bonanni *et al.* [227,228] reported EPR and

SQUID magnetisation results which revealed the coexistence of both Fe^{2+} and Fe^{3+} charge states in Fe ion implanted GaN. In the present study the latter is observed as a paramagnetic contribution resembled by components BT1 and BT2 with slow relaxation and will be discussed later, while the former is assigned to D2.

The third doublet (D3) is characterised by a relatively high quadrupole splitting of ~2.35(3) mm/s, an isomer shift of ~0.14(2) mm/s and a slightly broadened line shape with a linewidth of ~0.38(3) mm/s. The asymmetry of D3 is attributed to correlated distribution of isomer shifts and quadrupole splittings of Fe impurity atoms stemming from the probe atoms being located in isolated amorphous regions as observed in cubic III-V [172,173] and group IV [229,230,231] semiconductors following $^{57}Mn^{*}$ implantation. In GaAs and GaP, spatially isolated damage zones have been observed by TEM [232] following implantation of 50 keV Xe^{+} ions with fluences $\leq 2 \times 10^{10}$ ions/cm^2.

4.1.1.2. Temperature dependence of hyperfine parameters in GaN

A. Isomer Shift

The variation of the isomer shift values for Fe_S and Fe_C with temperature are shown in Figure 4.5. The isomer shift showed a temperature dependence close to second order Doppler (SOD) shift (as discussed in section 2.6.6.1) and was restricted to follow this behaviour in the final simultaneous analysis of the data. On the other hand, the isomer shift for Fe_C was fitted as a free parameter and shows a trend close to the second order Doppler shift with increasing temperature.

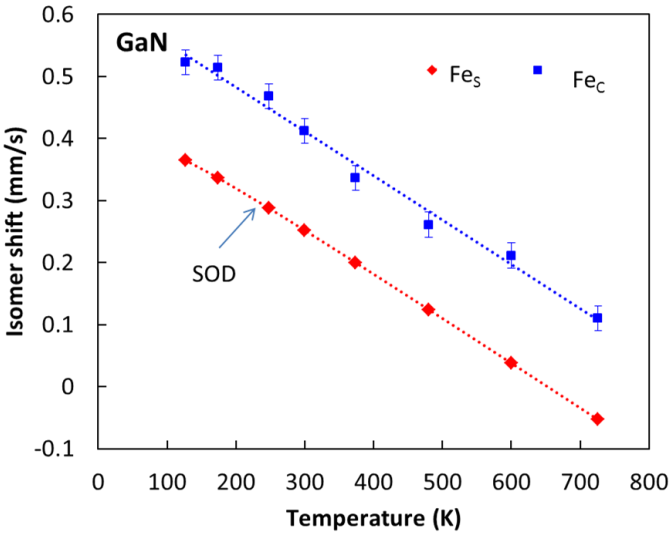


Figure 4.5: Temperature dependence of isomer shifts observed in the Mössbauer spectra for Fe implanted GaN. (The dotted line is to guide the eye)

B. Quadrupole splitting

As highlighted in the discussion of the analysis procedure, the quadrupole splitting of the Fe_S component showed minor changes with increasing temperature and was maintained to follow this constant behaviour. On the other hand, the average quadrupole splitting of Fe_C was fitted as a free parameter and follows an exponential decrease with increasing temperature as shown in Figure 4.6. The assignment of Fe_C due to Fe^{2+} implies that the quadrupole splitting is expected to follow a temperature dependence governed by Ingalls' interpretation [191] which is characteristic of Fe^{2+} and results from both lattice and valence ($3d^6$ shell) contributions to the EFG.

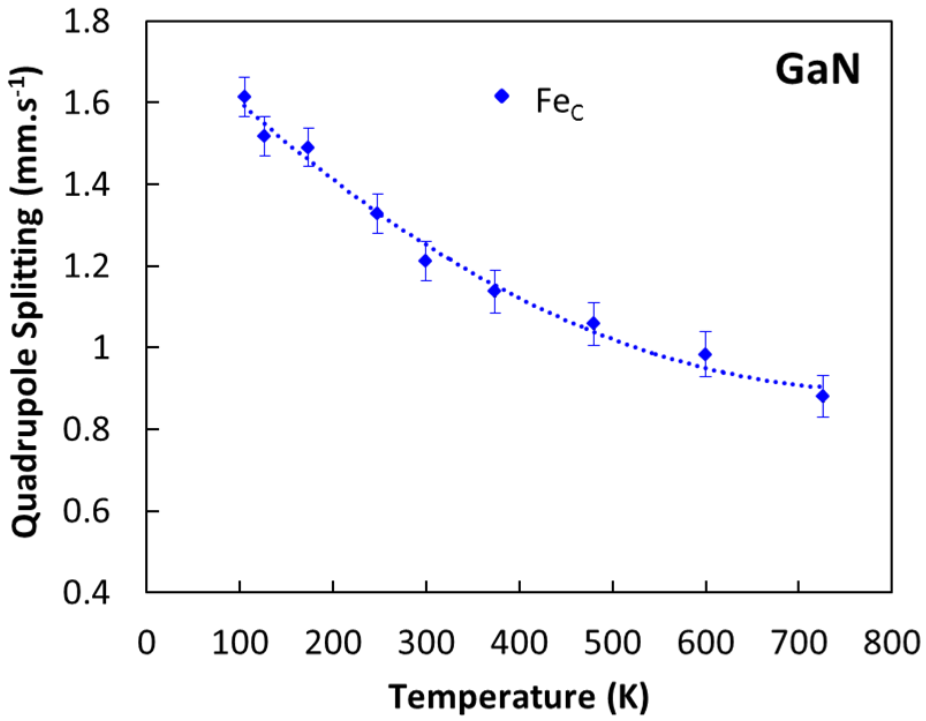


Figure 4.6: Temperature dependence of the quadrupole splitting for Fe_C observed in the Mössbauer spectra for Fe implanted GaN. (The dotted line is to guide the eye)

C. Magnetic relaxation

A zoomed view of the spectra showing the temperature dependence of the two Blume-Tjon sextets and their corresponding sum is illustrated in Figure 4.7 which also shows the collapsing of the sextet lines with increasing relaxation rate. The observed changes in the magnetic features of the spectra with increase in temperature could be explained by spin-lattice relaxation of high spin Fe^{3+} weakly

coupled to the lattice as observed in oxides [150,151,152,153]. As discussed earlier, spin-spin relaxation is ruled out due to the very low concentration of Fe ions (<10^{-4} at.%).

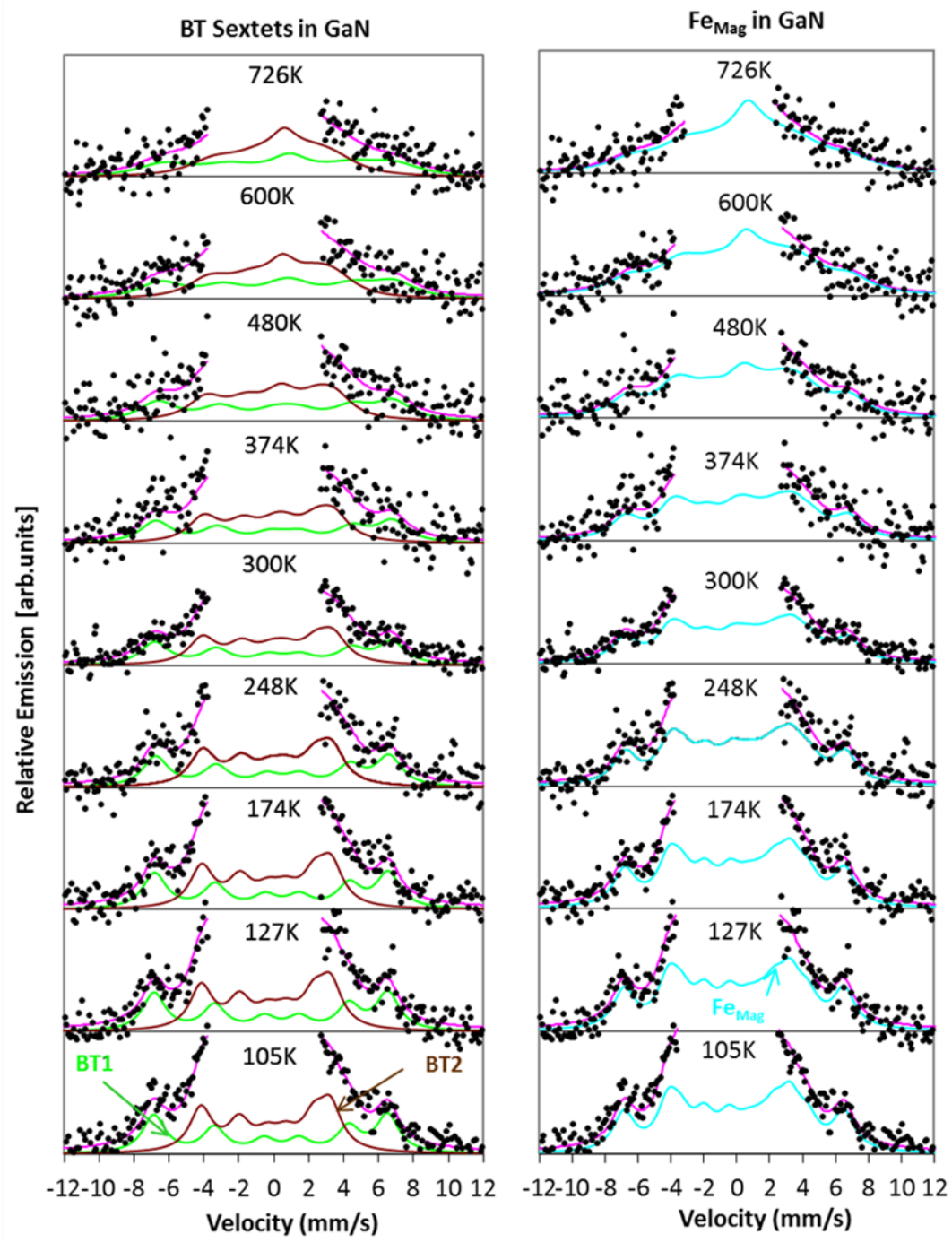


Figure 4.7: Two Blume-Tjon sextets and their sum, Fe_{Mag}, (in blue) shown in the central region of the emission Mössbauer spectra of $^{57}Mn^{*}$ implanted GaN at temperatures indicated.

In general, the spin-lattice relaxation for Kramers' ions can be expressed as $\tau^{-1} \propto T^{n}$ where n = 1, 2, 5, 7, or 9 in distinct temperature regions [162].

Consequently, any one of the temperature dependences are expected in our case for Fe^{3+} with a $3d^5$ electric configuration. In an initial analysis, the variation of the relaxation rate with temperature was set as a free parameter and was observed to follow a T^2 dependence over the measured temperature range. It was restricted to follow this behaviour in the final analysis. The variation of the relaxation rate with temperature obtained in a simultaneous analysis of the data is presented in Figure 4.8. The relaxation rates of Fe^{3+} were calculated using equation 4.3 and determined to be ~1.79×10^6 s^{-1} at 105 K and found to increase with temperature up to ~8.57×10^7 s^{-1} at 726 K. The T^2 dependence of the paramagnetic relaxation is characteristic of a two-phonon Raman process which dominates at high temperatures.

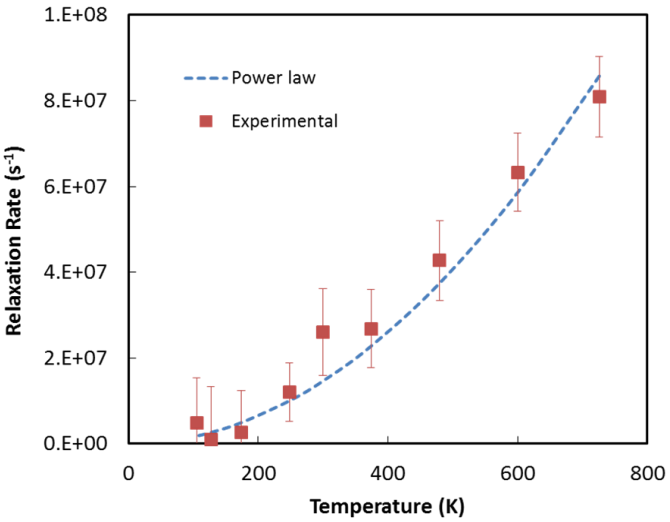


Figure 4.8: The temperature dependence of the spin-lattice relaxation rate of the Fe^{3+} paramagnetic state in GaN.

Figure 4.9 shows a plot of the trends in relaxation rates as a function of temperature obtained for GaN compared with those determined for α-Al_2O_3 and ZnO [151,153]. The temperature dependence of the relaxation rates in GaN was close to the behaviour observed in

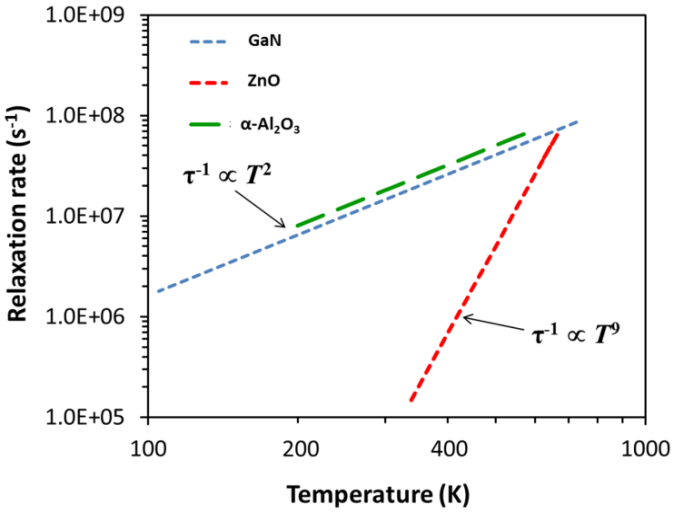


Figure 4.9: A plot of relaxation rates as a function of temperature obtained for GaN compared with data from previous studies of oxides [153].

α-Al_2O_3, while ZnO clearly showed an unexpected T^9 dependence in the measured temperature range [153].

4.1.1.3. Annealing Behaviour

Figure 4.10 shows the variation of the area fractions of the spectral components with temperature.

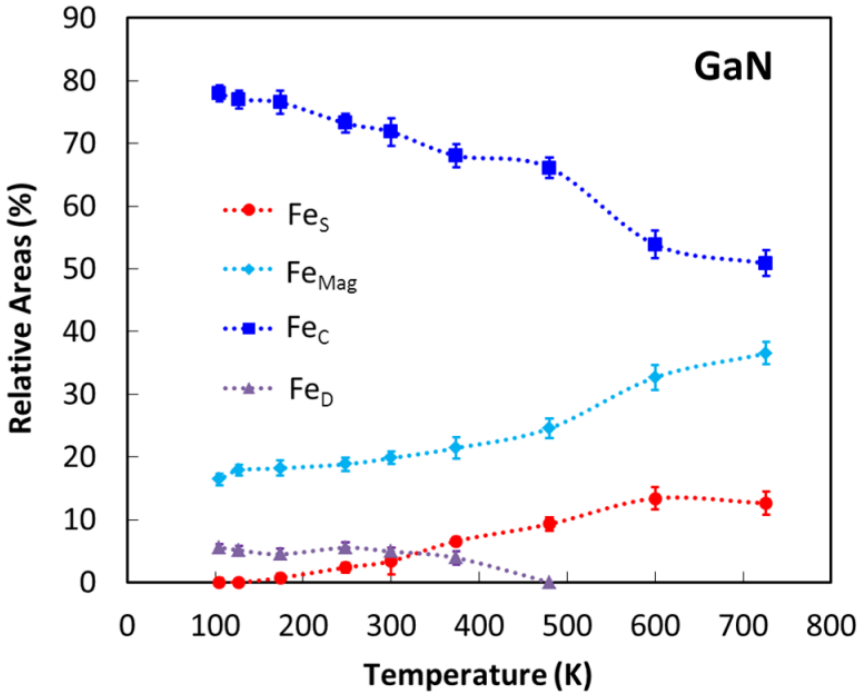


Figure 4.10: Areal fractions of spectral components as a function of temperature, observed in the Mössbauer spectra after implantation of $^{57}Mn^*$ into GaN.

Fe_S shows a steady increase in the area fraction from 0% to ~12% with increasing temperature up to ~600 K and thereafter remains fairly constant up to the highest measured temperature of 726 K. This behaviour is characteristic of Fe probe atoms on substitutional III site (Fe_s), as observed previously [172,173] in other $^{57}Mn^*$ implantation studies.

At the lowest measured temperature of 105 K, the spectrum is dominated by the Fe_C component assigned to Fe on near substitutional sites associated with vacancy related defects. Fe_C contributes ~78(1)% of the total area fraction with 16(1) % from the magnetic components due to high spin Fe^{3+} and the remaining fraction of ~6(1)% from Fe atoms in amorphous zones.

In the temperature range of 100 K-500 K, a steady decrease in the area fractions of Fe_C and Fe_D is observed which is accompanied by a corresponding increase in the substitutional Fe fraction and minor increases in the magnetic contribution. The Fe_D component completely disappears below 500 K, indicating lattice recovery and incorporation of the corresponding Fe atoms at substitutional sites or in paramagnetic complexes. A relatively small contribution of Fe atoms in these isolated amorphous regions is observed in GaN compared to cubic III-V [172,173] where Fe_D dominated the spectra at equivalent temperatures. This result confirms the radiation hardness of GaN. Evidently, implantation with fluences in the order of ~10^{12} ions/cm^2 does not induce intense formation of amorphous pockets in GaN compared with other cubic III-V compounds, such as GaAs, GaP and InP [177,173]. This observation is supported by earlier studies performed by Ronning *et al.* [107], who observed no amorphisation of the lattice structure in GaN and AlN after heavy ion implantation of ^{89}Sr and ^{111}In with fluence in the range (1-3) × 10^{13} at./cm^2. The presence of Fe atoms in amorphous zones is supported by the presence of the so-called 'random sites' observed in emission channelling measurements [105]. These random sites consist of a combination of various unidentifiable lattice site configurations.

A significant decrease in the population of Fe_C is evident in the range ~500-600 K. This agrees with positron annihilation results reported by Saarinen *et al.* [91,92], who attributed this behaviour to long-range mobility of Ga vacancies produced by 2 MeV electron irradiation. The magnetic component shows a gradual increase in the area fraction to ~35 % at the highest measured temperature of 726 K.

4.1.2. Analysis and Results: AlN

This section details the analysis and results of eMS measurement of Mn/Fe implanted AlN grown on a sapphire substrate. The spectra for AlN showed magnetic features on the wings and were fitted using a similar analysis model as GaN, with two sextets (BT1 and BT2) and three doublets (D1, D2 and D3). The central region of the spectra for AlN revealed different features at temperatures above room temperature and also displayed angular dependence in measurements on a narrow velocity scale of ±4.5 mm/s.

The spectra measured at emission angles of 60° and 0° on the narrow velocity scale are presented in Figure 4.11. The spectra were fitted with two quadrupole split doublets which were restricted to follow the angular dependence discussed earlier. A scaling factor for the observed angle dependence of the two-segment quadrupole spilt doublet, Q = 0.25(2) was determined from the analysis based on equation 4.2, which is relatively higher than the value of 0.08(1) obtained for GaN. The increase in the Q valued is indicative of the greater asymmetry of the two segment doublet.

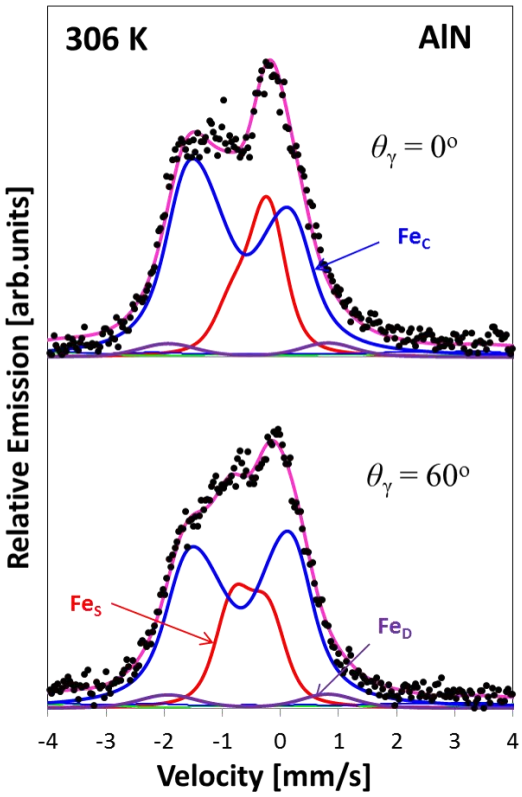


Figure 4.11: ^{57}Fe emission Mössbauer spectra obtained at 306 K after implantation of $^{57}Mn^*$ into AlN at emission angles indicated.

The differences in the structure for the central region of the spectra at the two measured angles are attributed to the angular dependence of both D1 (Fe_S) and D2 (Fe_C) inferred from similar behaviour in GaN. This suggests that the probe ions represented by Fe_C are located on regular crystalline sites, as observed in GaN, however the anisotropy is more pronounced in AlN. Figure 4.12 shows the fitted

spectra for the entire temperature series and Table 4.2 lists the hyperfine parameters extracted for AlN at room temperature.

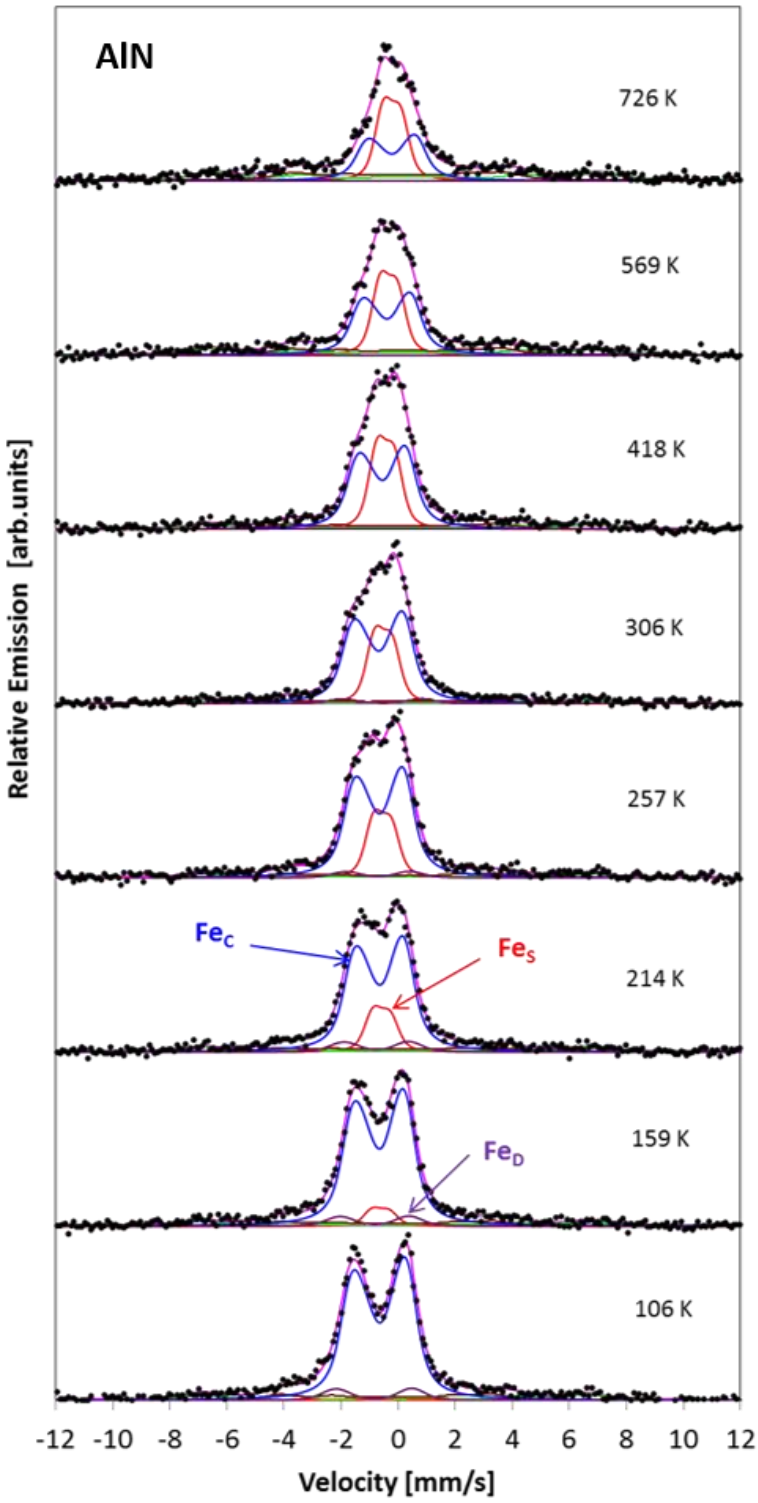


Figure 4.12: ^{57}Fe Mössbauer spectra obtained after ^{57}Mn* implantation into AlN held at the temperatures indicated and θ_γ = 60º.

Table 4.2: Hyperfine parameters for Fe implanted in AlN obtained at room temperature.

	D1 (Fe_S)	D2 (Fe_C)	D3 (Fe_D)	BT1	BT2
B_{hf} [T]	-	-	-	47(2)	23(2)
δ (mm/s)	0.51(2)	0.68(2)	0.56(3)	-0.11(3)	0.18(3)
$\Delta E_Q/\epsilon_Q$ (mm/s)	-0.59(1)	1.53(2)	2.75(4)	0.33(4)	
Γ (mm/s)	0.34	0.68	0.48(3)	1.41(3)	
$\sigma_L(\delta)$ (mm/s)	0.21(1)	-	0.39(2)	-	-
$\sigma_R(\delta)$ (mm/s)	-	-	0.37(2)	-	-

The observed linewidth of ~1.41(3) mm/s for the BT sextets is similar to that obtained for GaN. In addition to the natural linewidth of 0.50 mm/s, the broadened linewidths as in the case of GaN, can be explained in terms of the contributions from the inhomogeneity of the lattice surrounding the Fe probe atom in the sample, and/or Gaussian distribution of hyperfine fields.

4.1.2.1. Lattice site location

The hyperfine parameters of the substitutional component (Fe_S) for AlN were determined as δ = 0.51(2) mm/s and ΔE_Q = -0.59(1) mm/s which are quite different to those obtained for GaN (δ = 0.25(2) mm/s and ΔE_Q = -0.30(3) mm/s). The observed isomer shift of Fe_S for AlN is consistent with the value of 0.56 mm/s obtained for doublet D_1 (ΔE_Q = 0.68 mm/s) by Borowski *et al.* [109], from high fluence (in the order of 12 at.%.) implantation CEMS studies of AlN. These authors assigned D_1 to Fe surrounded by 4N atoms in the hexagonal structure of AlN. This is consistent with our assignment of Fe_S in GaN for Fe atom which is incorporated on a pure substitutional site tetrahedrally coordinated with 4N nearest neighbours. As highlighted earlier in the case of GaN, a negative quadrupole splitting suggest that the right leg of an asymmetrical doublet is more intense than the left side at angles, $\theta_\gamma < 54.7^o$ (i.e. the magic angle). This effect is clearly evident in Figure 4.11 which shows a more intense right leg of the Fe_C component for the spectrum measured at $\theta_\gamma = 0^o$, while a switch over is observed for the spectrum recorded at $\theta_\gamma = 60^o$. This is also apparent in the complete temperature series spectra for AlN presented in Figure 4.12.

4.1.2.2. Temperature dependence of hyperfine parameters in AlN

A. Isomer shift

The isomer shift of Fe_S was restricted to follow the second-order Doppler shift, while the average isomer shift for the distribution is approximately constant below room temperature. Above 306 K, the isomer shift of Fe_S decreases linearly with increasing temperature. The variation of the isomer shift values for the Fe_S and Fe_C components in AlN are depicted in Figure 4.13.

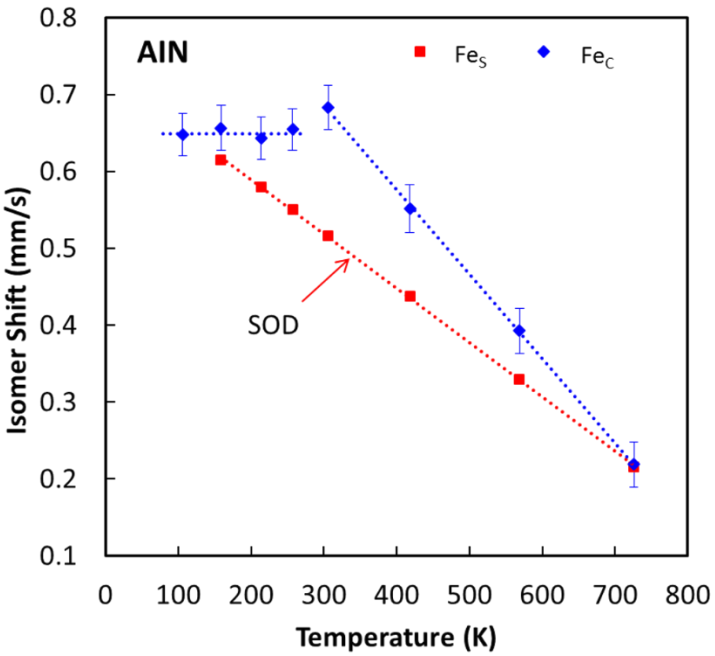


Figure 4.13: Temperature dependence of the isomer shifts for Fe_C and Fe_S observed in the Mössbauer spectra for Fe implanted AlN. (The dotted line is to guide the eye)

The drastic changes in the isomer shift of Fe_C at and above room temperature is indicative of changes in the bonding mechanism of Fe atoms on or near substitutional sites associated with vacancy related defects. This is tentatively attributed to an annealing stage and will be discussed further in this section.

B. Quadrupole splitting

The quadrupole splitting of Fe_C in AlN shows minor variations with increasing temperature compared to GaN as shown in Figure 4.14. At temperatures below 306 K, there is a steady decrease in the quadrupole splitting values, and above 306 K remains fairly constant up to the highest measured temperature of 726 K. Moreover, the steady decrease in the quadrupole splitting below room temperature

for the Fe_C component suggests minor changes in the lattice environment in the vicinity of the probe atoms, while the drastic changes in the isomer shift at and above 306 K suggest a change in the bonding mechanism. The non-varying quadrupole splitting with increasing temperature could be attributed to larger Fe probes occupying smaller Al lattice sites surrounded by neighbouring N atoms in closely packed environments. This is supported by differences in the spectra below and above 306 K (see Figure 4.12).

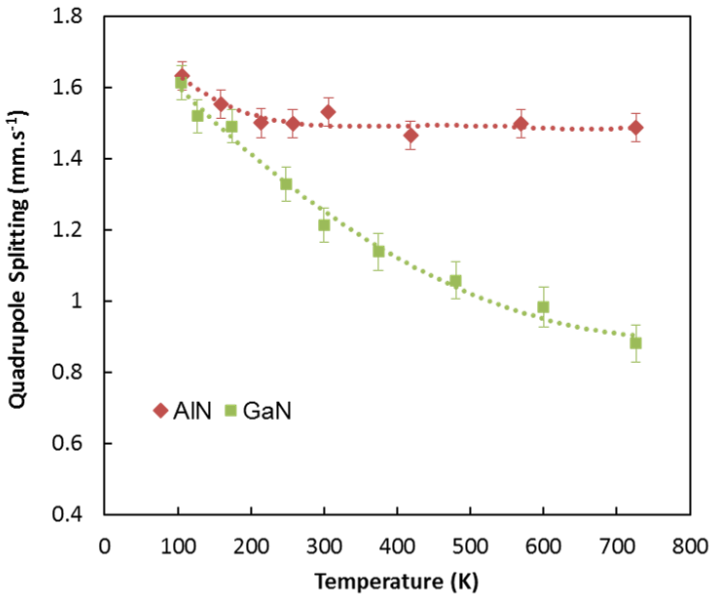


Figure 4.14: Temperature dependence of the quadrupole splitting for Fe_C observed in the Mössbauer spectra for Fe implanted AlN compared with GaN. (The dotted line is to guide the eye).

In AlN, Fe_D is characterised by a relatively high quadrupole splitting of ~2.75(4) mm/s, an isomer shift of ~0.56(3) mm/s and a Voigt line shape with a linewidth of ~0.48(3) mm/s.

C. Relaxation rates in AlN

The semi-empirical model was employed to the analysis of the magnetic structure in AlN with two BT sextets as in GaN. However, during the analysis, allowing line broadening at each measured temperature as a free parameter did not yield meaningful results with physical significance and this was attributed to limited statistics of the AlN data. As a result, spin-lattice relaxation rate were allowed to follow a temperature dependence of $\sim T^n$, where n was fitted as a global parameter.

In the final analysis, a value of $n = 2.1(4)$ was determined suggesting a two phonon Raman process in the measured temperature range. Figure 4.15 shows the zoomed in view of the AlN spectra highlighting the changes in the magnetic structure with increasing temperature.

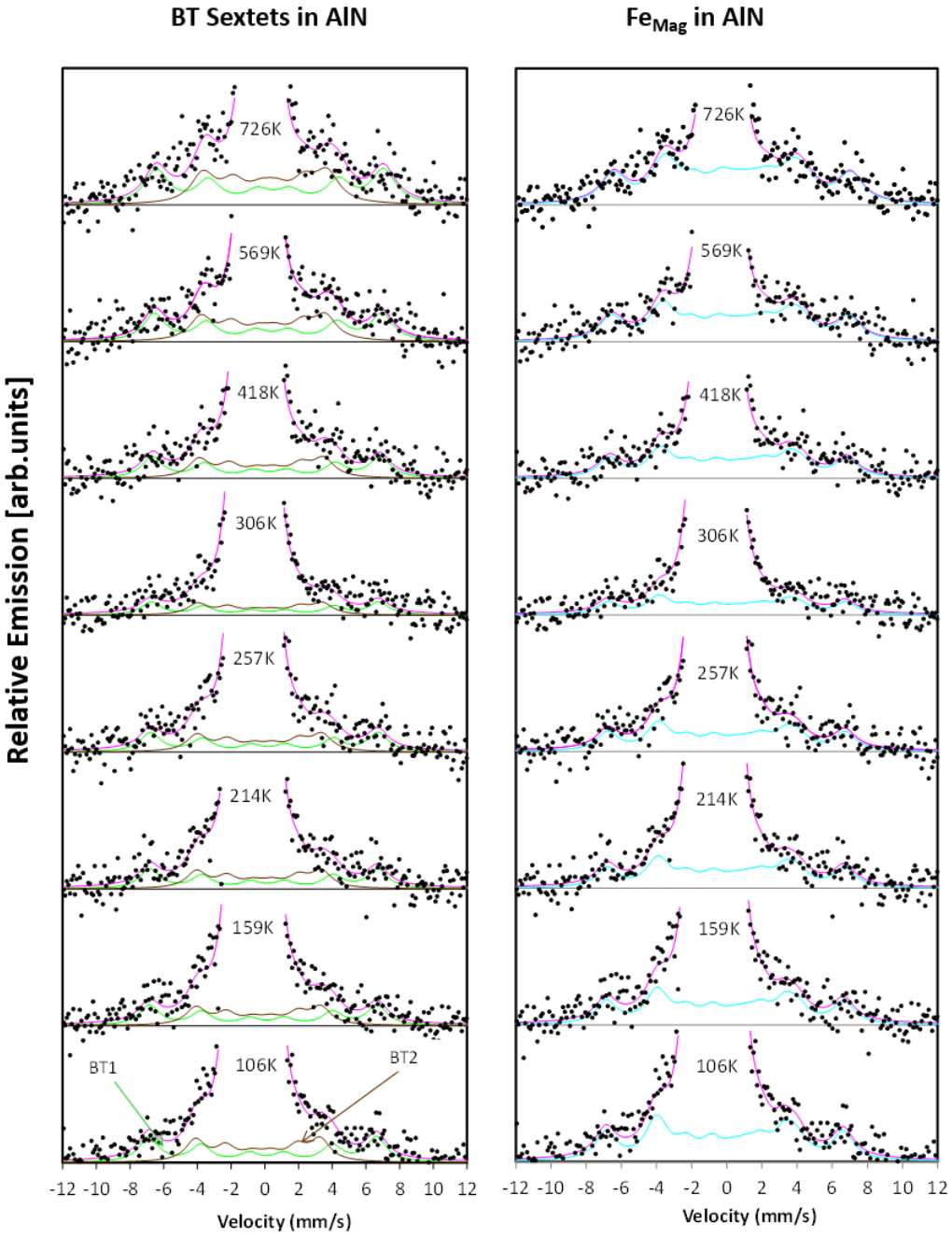


Figure 4.15: Two Blume-Tjon sextets (and their sum) showing the magnetic structure fitted for Fe implanted AlN spectra at the temperatures indicated.

The relaxation rates in AlN range from ~2.5×10^5 s^{-1} at 105 K to ~1.2×10^7 s^{-1} at 726 K and Figure 4.16 shows the T^2 temperature dependence of the spin-lattice relaxation rate of the Fe^{3+} paramagnetic state in AlN compared with trends in GaN, ZnO and α-Al_2O_3.

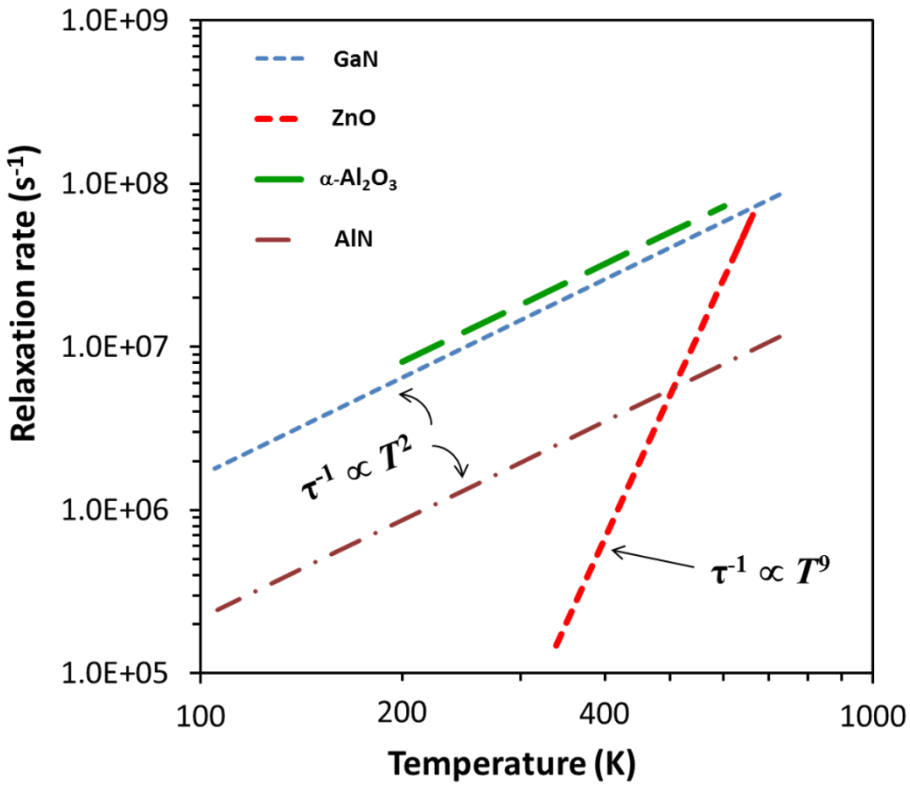


Figure 4.16: A comparison of relaxation rate trends of GaN and AlN with previously studied oxides [153].

The observed relaxation rate for Fe^{3+} in AlN is lower than in GaN, suggesting that the energy transfer between the spin and lattice is much faster in GaN which could be attributed to stronger and shorter bonds in AlN. The relaxation rates for GaN, AlN and Al_2O_3 closely follows the expected T^2 temperature dependence as predicted by literature [158] for a Raman process at high temperatures ($T \geq \theta_D/3$), while ZnO shows an unexpected T^9 dependence which is unusual for a Raman process at these high temperatures, the physics behind this behaviour is still not yet fully understood [153].

4.1.2.3. Area Fractions

The variation of the area fraction with increasing temperature for all spectral components is illustrated in Figure 4.17.

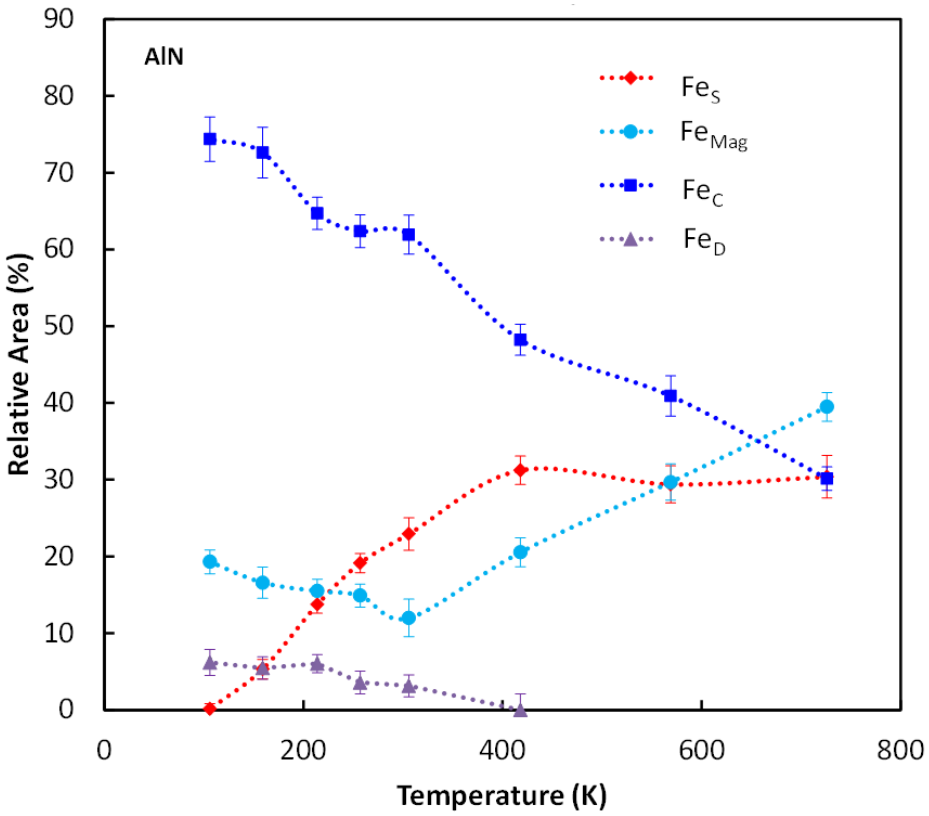


Figure 4.17: Areal fractions of spectral components as a function of temperature, observed in the Mössbauer spectra for AlN after $^{57}Mn^{*}$ implantation

At the lowest measured temperature of ~106 K, the spectra are dominated by Fe_C (~74%) assigned to Fe on near substitutional sites associated with vacancy related defects, with ~20% from the magnetic contribution (Fe_{Mag}) while the remaining fraction of ~6% is due to Fe atoms in isolated amorphous zones (Fe_D).

In the temperature range between 100 K and room temperature (306 K), the substitutional component increases by ~23 %. This increase is accompanied by a significant decrease in the area fractions for Fe_C (~12 %) and Fe_{Mag} (~8 %) and minor changes in the Fe_D component. The increase in the site population of Fe_S is attributed to dissociation of impurity-vacancy complexes associated with Fe_C, mainly marked by an annealing stage at temperatures between 150 K and 260 K. In addition, the small decrease in the quadrupole splitting of Fe_C below room

temperature suggests lattice recovery in the vicinity of Fe probe atoms in regular crystalline sites coupled with vacancy type defects.

At temperatures between 306 K and 420 K, the area fraction of the substitutional component increases by ~31% and then remains fairly constant up to the highest measured temperature of 726 K. The damage component disappears around 420 K while the magnetic contribution gradually increases from ~12% at temperatures above 306 K to ~40%, while an ~32 % decrease in the area fraction of the Fe_C component from ~62 % at room temperature to ~30 % at 726 K is evident. As highlighted earlier for GaN, the magnetic contribution is assigned to high spin Fe^{3+} located on the substitutional Ga site weakly coupled to the lattice, showing relaxation effects. The decrease in the site population of Fe_C is largely attributed to the dissociation of impurity-vacancy complexes coupled with the mobility of the resulting vacancies and Fe atoms moving towards purely substitutional sites. There is limited information in literature of the vacancy dissociation and mobility in AlN. Moreover, the drastic changes in the isomer shift occur with the same temperature range, affirming an annealing stage stemming from the breaking down of vacancy related complexes and motion of the resulting vacancies leading to changes in the bonding with the neighbouring lattice atoms.

4.1.3. Analysis and Results: InN

Emission Mössbauer spectroscopy results obtained after $^{57}Mn^{*}$ implantation into *n*-type InN, layer > 0.1 µm grown on Sapphire/GaN substrate are discussed in this section. The spectra shows no evidence of magnetic structure in the 'wings' on a wide velocity scale compared to GaN and AlN. A spectrum recorded at 304 K on a wide velocity scale is shown in Figure 4.18. The InN spectra were fitted with three doublets (D1, D2, and D3), similar components employed in analysing the central part of GaN and AlN spectra.

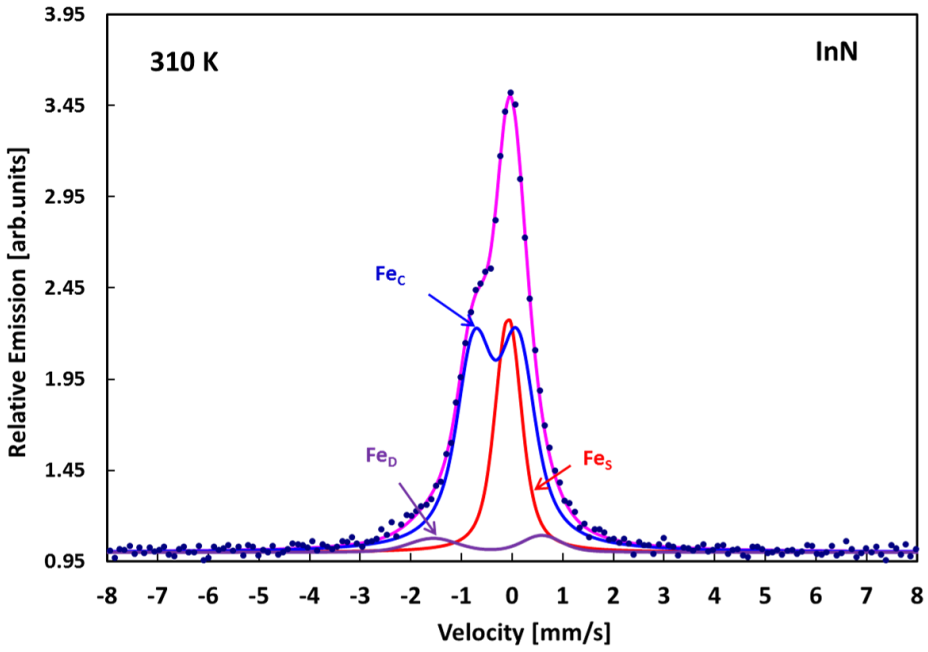


Figure 4.18: ^{57}Fe emission Mössbauer spectrum obtained at 310 K for InN after implantation of $^{57}Mn^{*}$ at θ_γ = 60º.

Similar lattice sites assignments were adopted, two quadrupole split doublets (i) Fe on purely substitutional III sites (Fe_S) and (ii) Fe atoms near substitutional sites but associated with vacancy type defects (Fe_C) and a third quadrupole split doublet assigned to Fe atoms in isolated amorphous zones (Fe_D).

The spectra measured at emission angles of 0º and 60º are shown in Figure 4.19. A clear angular dependence is evident from visual inspection as shown by a slightly more intense left shoulder at 0º than at 60º and is supported by the asymmetry observed for Fe_C at 0º. The analysis yields a Q value of 0.07(1) for InN from equation 4.3 giving the scaled dependence of D2 (Fe_C).

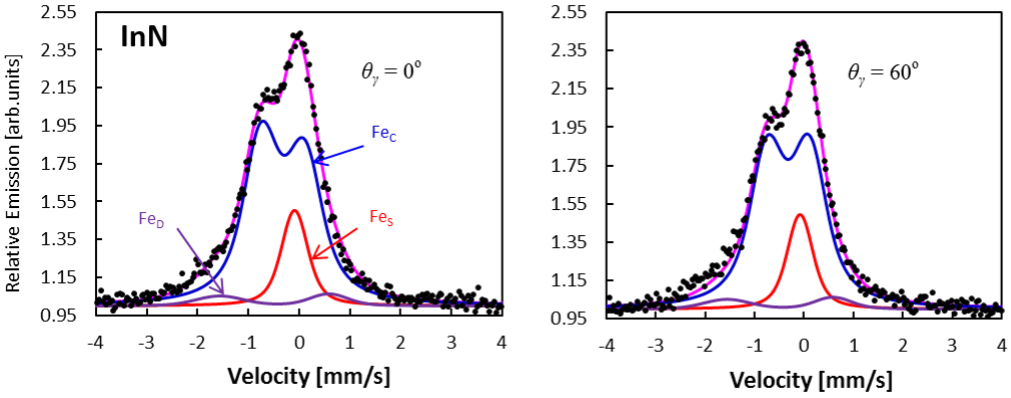


Figure 4.19: ^{57}Fe emission Mössbauer spectra obtained after implantation of ^{57}Mn* into InN at 304 K at and emission angles indicated.

The hyperfine parameters of the fitted components are listed in Table 4.3.

Table 4.3: Hyperfine parameters extracted from the analysis of the InN spectrum recorded at 310 K.

Components	D1 (Fe_S)	D2 (Fe_C)	D3 (Fe_D)
δ (mm/s)	0.08(2)	0.32(2)	0.49(4)
ΔE_Q (mm/s)	0.02(3)	0.84(1)	2.15(2)
Γ (mm/s)	0.34	0.64	0.34
$\sigma_L(\delta)$ (mm/s)	0.17(2)	-	0.40(4)
$\sigma_R(\delta)$ (mm/s)	-	-	0.30(3)

4.1.3.1. Nature of Fe in InN

Isomer shift values of 0.08(2) mm/s and 0.32(2) mm/s for Fe_S and Fe_C, respectively, were extracted from the analysis. These values suggest similar chemical nature for Fe dopants of covalently bonded Fe(III) on substitutional In sites and Fe^{2+} on or near substitutional site associated with a vacancy related defects. The absence of magnetic structure in eMS results of Fe implanted InN indicates that high spin Fe^{3+} is not present in the measured temperature range.

The analysis model was sufficient to describe the data, the spectra for the complete temperature series are shown in Figure 4.20 which clearly shows no evidence of magnetic structure as compared to the data obtained for GaN and AlN.

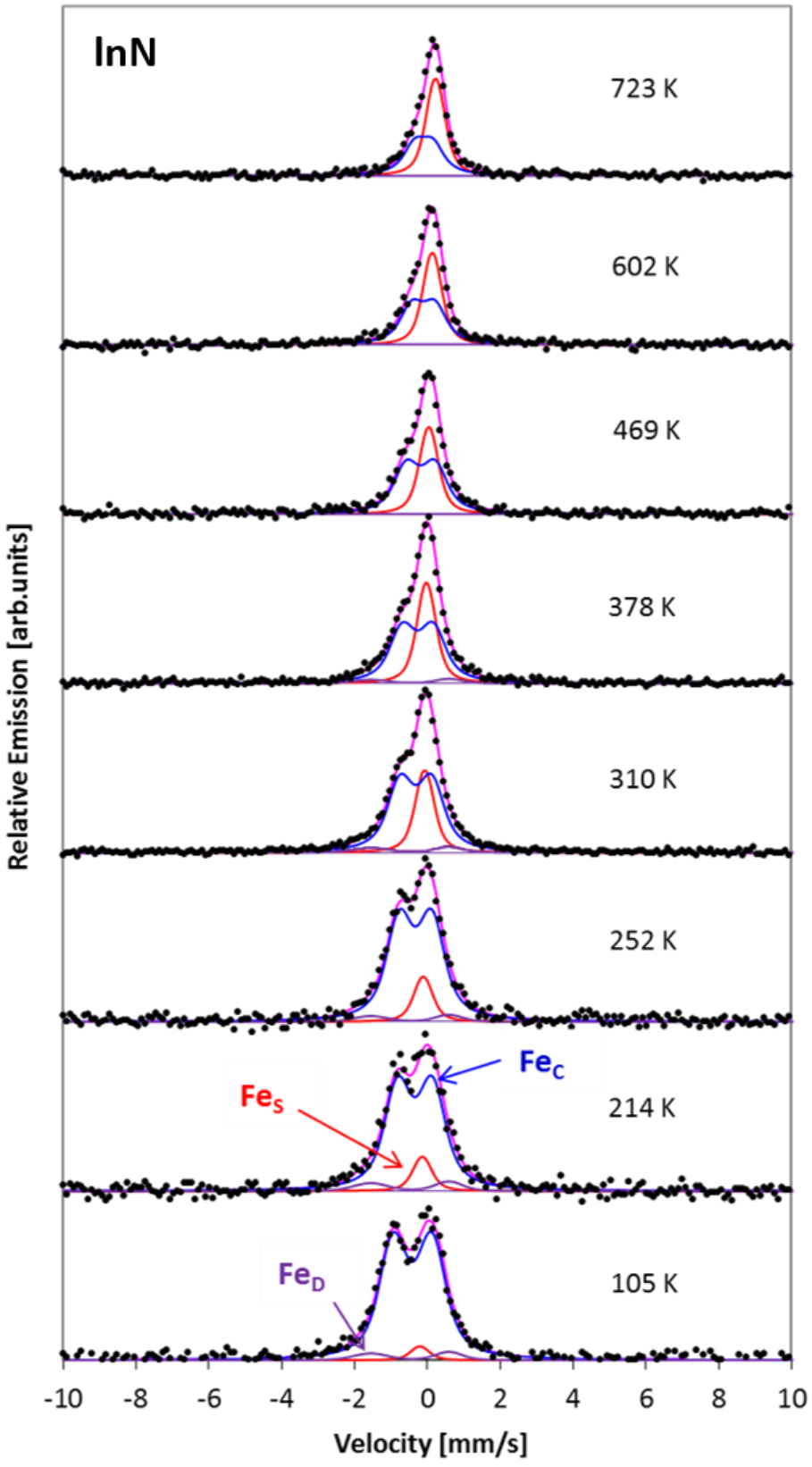


Figure 4.20: ^{57}**Fe emission Mössbauer spectra obtained after implantation of** ^{57}**Mn*** **into InN at the temperatures indicated and** θ_γ **= 60º.**

4.1.3.2. Temperature dependence of hyperfine parameters

The temperature dependence of the hyperfine parameters for InN is presented in Figures 4.21 and 4.22. The average isomer shift of Fe_C shows a trend close to the second order Doppler shift with increasing temperature, while the average quadrupole splitting of Fe_C shows a linear dependence (dotted line).

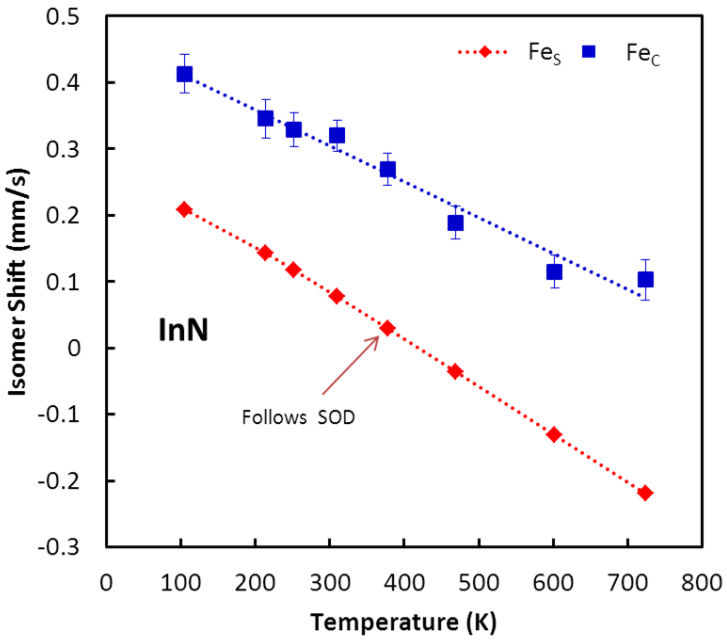


Figure 4.21: Temperature dependence of the isomer shifts observed in the Mössbauer spectra for $^{57}Mn^*$ implanted InN. (The dotted line is to guide the eye)

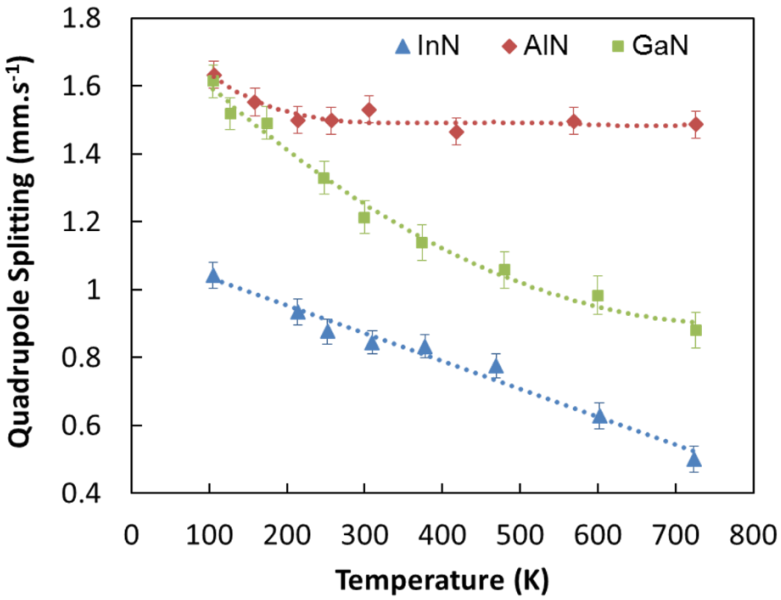


Figure 4.22: Temperature dependence of the quadrupole splitting for Fe_C observed in the Mössbauer spectra for $^{57}Mn^*$ implanted III-nitrides. (The dotted line is to guide the eye).

4.1.3.3. Annealing Behaviour

The relative area fractions of the fitted spectral components are presented in Figure 4.23 as a function of temperature.

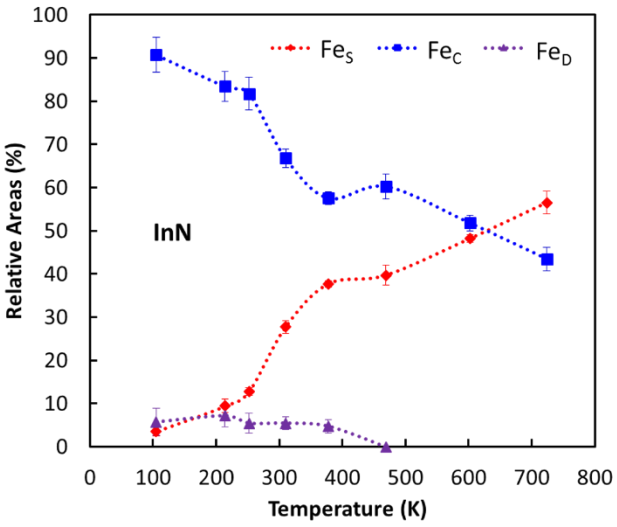


Figure 4.23: Areal fractions of spectral components as a function of temperature as determined from the Mössbauer spectra of InN following $^{57}Mn^{*}$ implantation.

At the lowest measured temperature of 105 K, ~91% of the spectrum is dominated by Fe atoms on near-substitutional sites associated with some vacancy type defects. The remaining fraction is attributed to small contributions from Fe atoms in isolated amorphous regions (~6%) and to substitutional Fe atoms (~3%). At temperatures below 240 K, the area fraction of Fe_C decreases slightly by ~8% and the purely substitutional fraction show a ~6% increases, while the area fraction of the damage component remains relatively constant.

In the temperature range, 240-380 K, a significant increase of ~29% in the area fraction of Fe_S is accompanied by a decrease of ~25% in the intensity of Fe_C, which is largely attributed to the dissociation of impurity-vacancy complexes coupled with the mobility of the resulting vacancies and Fe atoms moving towards purely substitutional sites. A minor decrease (~2%) in the area fraction of Fe_D is observed around 260 K which remains fairly constant in this temperature range.

The area contribution of Fe_D decreases to zero at temperatures between 380 K and 500 K which is accompanied by a corresponding small increase of ~3% in the area

fraction of Fe_C. This is attributed to the recovery of the lattice in the vicinity of Fe probe atoms, with the dopants possibly moving from isolated amorphous zones towards near substitutional sites. The purely substitutional fraction remains constant in this temperature range.

Above 500 K, there is ~17% increase in the population of Fe_S, resulting from Fe atoms in near substitutional sites and vacancy complexes probably moving to purely substitutional lattice sites as the vacancy complexes dissociate and the resulting vacancies become mobile. At the highest measured temperature of 723 K, 43(4) % of the Fe ions are located on near substitutional sites associated with vacancy type defects whilst the remaining 57(4) % probe atoms are on purely substitutional sites.

4.1.4. Absence of interstitials in nitrides

A significant fraction of recoil-produced Fe interstitials were expected in the nitride samples investigated in the present measurements, as reported previously in eMS studies of Mn/Fe implanted silicon [233], InP [173], GaAs and GaP [172] with an isomer shift ~1 mm/s. This is because a mean recoil energy of 40 eV is imparted to the Fe daughter atom in the $^{57}Mn^{*} \rightarrow ^{57}Fe$ β-decay, which is expected to re-locate the ^{57}Fe ions from the implanted $^{57}Mn^{*}$ sites into interstitial sites. Emission channelling results show that implanted Fe atoms in an as-implanted GaN sample were incorporated on substitutional sites whilst the remaining fraction was located on "random" sites [105], with no specific mention of Fe interstitials. On the other hand, interstitials were observed in GaN and AlN in EC studies with implantation of light radioactive ions, ^{8}Li and ^{24}Na. In their study, the authors observed a lattice site change of Na interstitials to substitutional in AlN but not in GaN after annealing at 1073 K [107]. Thus, to displace an atom from the occupied substitutional site, the recoil energy should be greater than 40 eV. As highlighted in section 1.3.1 inconsistent displacement energies of atoms mainly in GaN and AlN have been reported by different groups. Recent molecular dynamics results reported by Xiao and co-authors for GaN [64] in five main crystallographic directions in GaN estimated high average displacement energy values of E_d(Ga) = 73.2 eV and E_d(N) = 32.4 eV. On the other hand, Wendler [68] estimated displacement values of E_d(Al) = 18.8 eV and E_d(N) = 22 eV for AlN from a combination of RBS/C

experiments and SRIM based calculations. However, higher displacement energies would be expected in AlN since the Al-N bonds are relatively stronger than Ga-N in GaN. The absence of recoil produced interstitials would be expected in nitrides and could be explained by high displacement energies greater than 40 eV. As a result, the substitutional lattice site is maintained by the majority of the ^{57}Fe implanted ions.

4.1.5. Summary of results in III-nitrides

The spectra obtained for GaN and AlN revealed magnetic structure in the 'wings' of the spectra on a wide velocity scale of ±12 mm/s. This structure was analysed using the Blume-Tjon semi-empirical relaxation model [150] utilizing two sextets. The observed temperature-dependent magnetic effect is consistent with a slow spin-lattice relaxation of paramagnetic Fe^{3+}, as reported for low fluence ($\leq 10^{-12}$ cm^{-2}) implanted oxide semiconductors [150,151,152,153], namely ZnO, MgO, and α-Al_2O_3. The relaxation rate closely follows a T^2 temperature dependence, characteristic of a two-phonon Raman process. The spectra for InN showed no evidence of magnetic features which could be explained by the absence of Fe^{3+} (S=5/2) weakly coupled to the lattice in this material presumably on substitutional sites as observed in oxides.

In all nitrides, measurements at emission angles of 60^o and 0^o on a narrow velocity range of ±4.5 mm/s shows angular dependence of the central part of the spectra. Two quadrupole split components consistent with the observed anisotropy were employed in the initial analysis. These were assigned to: (i) Fe atoms incorporated on pure substitutional III sub-lattice (Fe_S) tetrahedrally coordinated with 4 N nearest neighbours resulting from covalent bonding between the atoms, and (ii) Fe atoms on near substitutional sites associated with vacancy related defects (Fe_C). In addition, a third quadrupole split doublet (Fe_D) with a relatively small area contribution was required to give good fits and the lack of angular dependence is typical of implantation induced damage. Moreover, the angular dependence of the Fe_C component observed demonstrate that Fe atoms are located close to regular crystalline sites and not in radiation induced damage zones.

The isomer shift of the substitutional component were consistence with the expected SOD shift while the quadrupole splitting showed minor variation with increasing temperature in all the materials. The isomer shift of Fe_C closely followed the second-order Doppler shift in GaN and InN, while significant variations are observed in AlN below and above 306 K signifying drastic changes in the bonding mechanism between the probe atoms and neighbouring lattice atoms. In GaN, the quadrupole splitting of Fe_C shows an exponential decrease with increasing temperature, while in InN a steady decrease is observed but in AlN a minor decrease is observed below 306 K, after which it remains fairly constant indicating minor changes in the local symmetry around the probe atoms.

In GaN, A fairly significant decrease in the population of Fe_C is evident in the range, 500-600 K which is attributed to long-range mobility of Ga vacancies. However, in AlN two major annealing stages are observed in the temperature ranges 160-260 K and above 306 K where drastic changes in the hyperfine parameters are evident. In InN there three distinct stages the temperature ranges, 105-240 K, 240-380 K and above 500 K. The multiple annealing stages in these materials are attributed to a combination of both the dissociation of Fe-vacancy complexes and mobility of the resulting vacancies and complete recovery of the lattice in implantation induced amorphous regions.

In light of the high radiation sensitivity of InN compared to AlN and GaN, a significant contribution of implantation induced damage is expected. However, the fraction of the isolated amorphous zones determined in this work is ~6%. This observation is supported by emission channelling studies of ^{59}Fe in GaN [105] where ~20% of Fe atoms were attributed to random sites partly due to unidentifiable lattice site configurations which when compared to eMS a fraction of these atoms could be assigned to implantation induced damage.

The recovery of the lattice for Fe probe atoms in isolated amorphous zones is observed above ~400 K in AlN and above ~500 K in GaN and AlN. The relatively small area contribution this component over the measured temperature range attests to the radiation hardness of these III-nitrides compared to cubic III-Vs.

4.2. Virgin ZnO and ^{56}Fe pre-implanted ZnO

In the midst of several reports with mixed reviews on the nature of magnetism in Fe doped ZnO, our collaboration has reported results on emission Mössbauer spectroscopy on virgin ZnO single crystals following $^{57}Mn^{*}$ implantation with a fluence of ~3×10^{12} ions/cm^2. The absence of ordered magnetism in extremely dilute ZnO [151] was unequivocally proven through angle dependent measurements in the presence of an external magnetic field of 0.6 T. The emission Mössbauer spectra exhibited paramagnetism, resulting from Fe^{3+} weakly coupled to the lattice located on Zn substitutional sites, showing temperature dependent spin-lattice relaxation. The spin-lattice relaxation rates of Fe^{3+} in ZnO was found to follow an unusual T^9 temperature dependence from measurements performed without an external magnetic field [153].

A typical room temperature (RT) emission Mössbauer spectrum for virgin ZnO single crystal obtained after implantation of $^{57}Mn^{*}$ is shown in Figure 4.24.

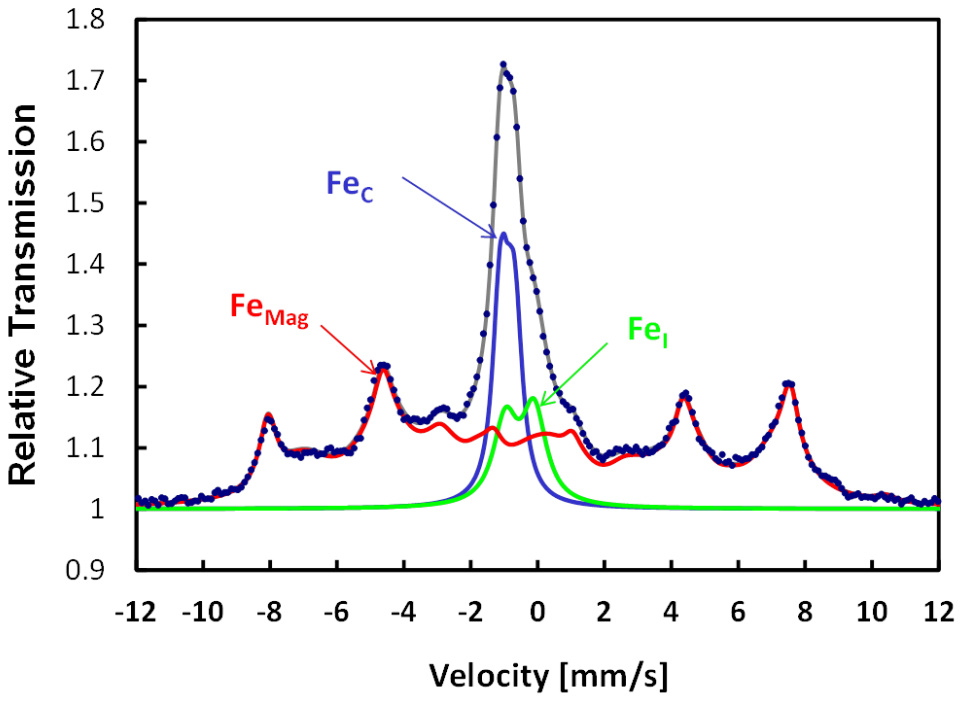


Figure 4.24: Room temperature (305 K) emission Mössbauer spectrum obtained after implantation of $^{57}Mn^{*}$ into virgin ZnO. Fe_{Mag} (Fe^{3+}) represents the sum of the five BT sextets.

The observed magnetic structure was analysed using the semi-empirical Blume-Tjon [225] (BT) model described by Mølholt *et al.* [150] . In addition, the line

broadening (ΔΓ) given by equation 4.3 is an important parameter of the BT model from which the relaxation time (τ^{-1}) is extracted. In the final fitting procedure, the magnetic feature was fitted with five BT sextets and the central region of the spectrum was best described with two doublets attributed to Fe on regular crystalline sites (Fe_C) and Fe on interstitial sites (Fe_I).

The hyperfine parameters obtained from the fit to the spectrum shown in Figure 4.24 are presented in Table 4.4.

Table 4.4: Hyperfine parameters extracted from the analysis of the virgin ZnO spectrum measured at room temperature.

Components	Fe_C	Fe_I	Fe_{Mag}^{+}
B_{hf} [T]	-	-	48.0
δ (mm/s)	0.90(2)	0.53	0.19(3)
ΔE_Q /ϵ_Q (mm/s)	-0.40(3)	0.85	0.12(2)
*Γ (mm/s)	0.17	0.50	0.63
*$\sigma(\delta)$ (mm/s)	0.02(2)	0.01(1)	-
Area (%)	17(2)	12(1)	71(1)

* Γ – FWHM and σ – Gaussian broadening with the detector values subtracted.

+ Parameters of the subsextet with the sharpest lines assumed for $S_z = \pm 5/2$.

The thermal variation of the quadrupole splitting, ΔE_Q (T) for Fe_C was observed to follow Ingalls [191] prediction given by the simplified expression,

$$\Delta E_Q(T) = \Delta E_{Q,Lat} + \Delta E_{Q,Val} \tanh\left(\frac{E_0}{2k_B T}\right), \quad (4.4)$$

where $\Delta E_{Q,Lat}$ is the contribution from non-cubic arrangement of lattice atoms, $\Delta E_{Q,Val}$ is the valence contribution resulting from Fe in z^2 d orbitals, E_0 is the splitting energy between the z^2 and x^2-y^2 orbitals. A value of $\Delta E_{Q,Lat}$ = +0.12 mm/s was obtained using a quadrupole shift of high spin Fe^{3+} in ZnO [151] and value of $\Delta E_{Q,Val}$ = -2.5 mm/s was obtained from Co/Fe implantation in ZnO [155]. However, for the interstitial component, ΔE_Q was observed to follow an exponential temperature dependence given by the equation,

$$\Delta E_Q(T) = Q_0 \exp\left(-\frac{T - T_0}{\Delta_E}\right), \quad (4.5)$$

where the fitting parameters T_0, Q_0, and Δ_E have values of 300 K, 0.85 mm/s, and 841 K [153], respectively which was obtained from simultaneous analysis. The

isomer shift of the BT sextets, Fe_C and Fe_I were restricted to follow the second-order Doppler shift with increasing temperature. The two doublets were assumed to have an angle dependence with the maximum value given by the intensity ratio (I_π/I_σ) = 0.88 for an emission angle of 60^o from equation 2.24. Angle dependent eMS measurements on virgin ZnO samples were undertaken in earlier studies of the collaboration [151] and were not repeated in the present study. The results were assumed to apply equally well to the samples herein investigated.

In addition, to investigate the effect of fluence or increase in atomic concentration on the magnetic contribution and the resulting relaxation effects, three ZnO samples were pre-implanted with ^{56}Fe ions with 60 keV energy to fluences of 8×10^{13}, 5×10^{13} and 2×10^{13} ions/cm^2 corresponding to peak concentrations of 2.8×10^{-2}, 1.8×10^{-2} and 7×10^{-3} at.%, respectively. The implantation energy of 60 keV result in a peak concentration of ^{56}Fe atoms at an implantation depth of ~27 nm. The implantation energy was chosen to match the energy of 50-60 keV used for $^{57}Mn^*$ implantation at ISOLDE to achieve overlapping depth profiles and range of atoms into the specimen during emission Mössbauer spectroscopy measurements. A similar analysis procedure and assignment of spectral components adopted for virgin ZnO was utilised for the pre-implanted samples.

The Gaussian broadening for the Fe_C component for the ZnO sample implanted with 8×10^{13} ions/cm^2 was fitted as a free parameter over the measured temperature range to obtain acceptable fits to the data. The other pre-implanted samples did not show significant changes with temperature, hence the Gaussian broadening was maintained as a global parameter. The emission Mössbauer spectra collected at temperatures between 300 and 720 K for the ZnO samples pre-implanted with ^{56}Fe ions with fluences of 8×10^{13}, 5×10^{13} and 2×10^{13} ions/cm^2 following $^{57}Mn^*$ implantation are shown in Figure 4.25 indicated by the corresponding sample identifier assigned in chapter 3 namely, ZnO:^{56}Fe8, ZnO:^{56}Fe5, and ZnO:^{56}Fe2, respectively.

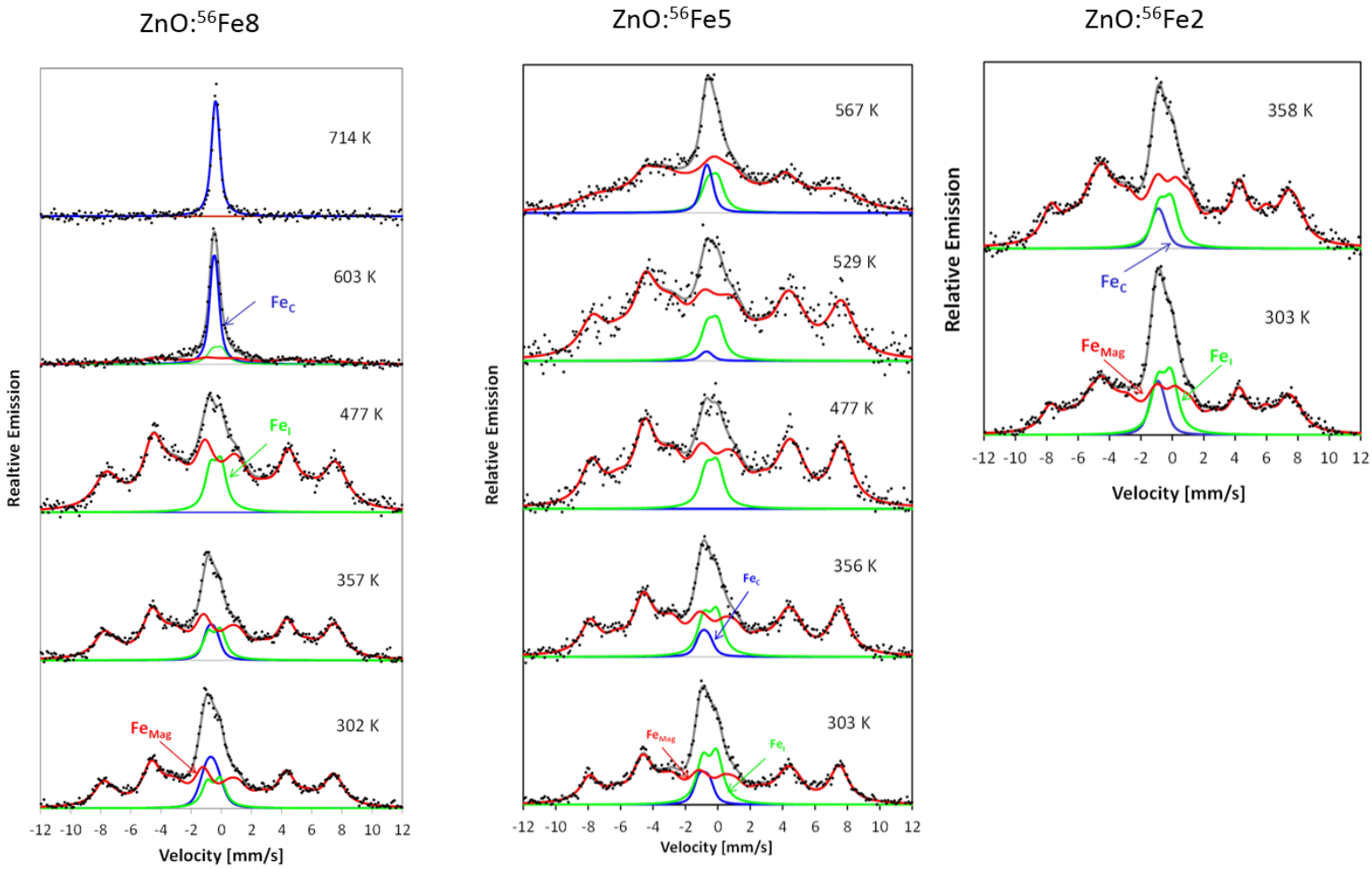


Figure 4.25: ^{57}Fe emission Mössbauer Spectra for ZnO pre-implanted with ^{56}Fe at indicated fluences.

Table 4.5: Room temperature hyperfine parameters extracted for ZnO pre-implanted with ^{56}Fe at indicated fluences.

^{56}Fe	ZnO:^{56}Fe8 (8×10^{13} ions/cm^2)			ZnO:^{56}Fe5 (5×10^{13} ions/cm^2)			ZnO:^{56}Fe2 (2×10^{13} ions/cm^2)		
Components	Fe_C	Fe_I	Fe_{Mag}^{+}	Fe_C	Fe_I	Fe_{Mag}^{+}	Fe_C	Fe_I	Fe_{Mag}^{+}
B_{hf} [T]	-	-	46 (3)	-	-	47(2)	-	-	46(2)
δ (mm/s)	0.67(4)	0.50	0.18(2)	0.85(3)	0.50	0.19(3)	0.92(2)	0.50	0.19(2)
ΔE_Q/ ϵ_Q (mm/s)	-0.61(3)	0.85	0.12(3)	-0.53(3)	0.85	0.12(2)	-0.42(3)	0.85	0.12(1)
$^{*}\Gamma$ (mm/s)	0.17	0.50	1.02	0.17	0.50	1.02	0.17	0.50	1.02
$^{*}\sigma(\delta)$ (mm/s)	0.30(2)	0.01(1)	-	0.12(2)	0.05(3)	-	0.22(3)	0.01(1)	-
E_0 [meV]	11(3)	-	-	14(2)	-	-	15(1)	-	-

* Γ – FWHM and σ – Gaussian Broadening with the detector values subtracted.

$^{+}$ Parameters of the subsextet with the sharpest lines assumed for $S_z = \pm 5/2$.

4.2.1. Hyperfine interaction (HI) parameters

The hyperfine parameters extracted at room temperature for the three pre-implanted samples are presented in Table 4.5. A quadrupole splitting value of -0.61 mm/s was obtained for Fe_C and a crystal field splitting value of E_0 =16(1) meV was determined from equation 4.4 for the high fluence implanted sample (ZnO:^{56}Fe8) using $\Delta E_{Q,Lat}$ and $\Delta E_{Q,Val}$ values of +0.12 mm/s and -2.5 mm/s, respectively, as reported by Gunnlaugsson *et al.* [155].

For the ZnO sample implanted with a fluence of 5×10^{13} ions/cm^2 (ZnO:^{56}Fe5), a quadrupole splitting value (ΔE_Q) value of -0.56(3) mm/s for Fe_C is slightly less negative compared with the value of -0.61(3) mm/s obtained for the ZnO:^{56}Fe8 sample. The E_0 value for this sample was determined to be 14(2) meV.

An ΔE_Q value of -0.42(2) mm/s obtained for Fe_C for the ZnO:^{56}Fe2 sample and this value is comparable to the value of -0.39(3) mm/s reported for virgin ZnO [151]. The resulting E_0 value of 11(3) meV is comparable to the value of 10 meV reported for virgin ZnO [153] considering the relative large error.

The ΔE_Q value of 0.85 mm/s for the interstitial component was obtained using equation 4.5 while the hyperfine parameters for Fe_{Mag} are in good agreement with values of δ = 0.19(1) mm/s and $\epsilon_Q \sim$ +0.12(1) mm/s reported by Gunnlaugsson and co-authors [151] for virgin ZnO.

The decrease in the isomer shift values of Fe_C with increasing fluence attest to an increase in the *s*-electron density at the nucleus of the probe atoms which suggest strengthening of the bonds between the Fe atoms on crystalline sites and the surrounding lattice atoms. On the other hand, the increase in the value of the negative quadrupole splitting values with increasing fluence suggests a loss of symmetry at the nucleus of the Fe atoms, resulting from the increase in the number of atoms surrounding the probe atom in the crystalline sites.

4.2.2. Fluence dependence of crystal field splitting values for Fe_C.

The fluence dependence of the E_0 values is shown in Figure 4.25 compared with previous studies [234]. The data obtained from this work follows an approximately linear dependence as observed for other ^{56}Fe pre-implanted ZnO samples. As a result, it can be concluded that for fluences below 10^{13} Fe ions/cm^2, there are minor changes in the transition energies between the z^2 and x^2-y^2 orbitals energy levels in the 3*d* orbitals of Fe^{2+}. However, above 10^{13} ions/cm^2, the crystal field splitting is observed to increase with increasing Fe fluence which follows the same trend observed for fluences >10^{14} ions/cm^2 as reported in other studies shown in Figure 4.26.

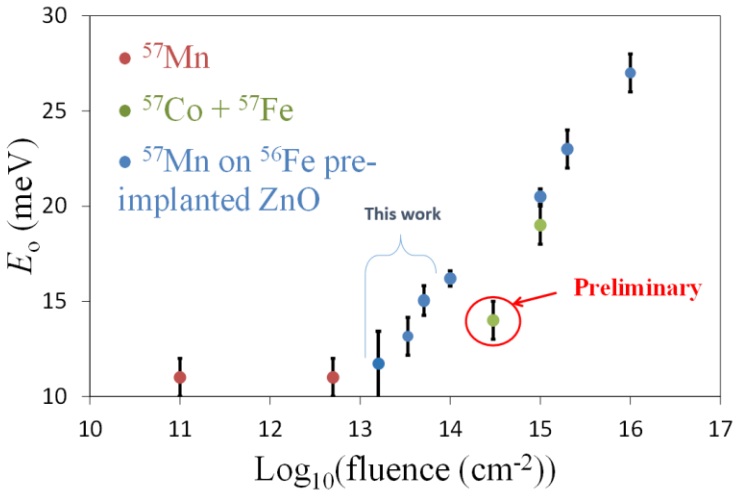


Figure 4.26: A plot of E_0 values as a function of fluence compared with other Mössbauer measurements. [Adapted from [234]]

4.2.3. Properties of the magnetic component

The area fractions extracted at room temperature for Fe^{3+} as a function of concentration compared with results obtained from other studies [234] are presented in Figure 4.27. The area fraction of Fe_{Mag} obtained for the three pre-implanted samples at RT is ~76% of the total spectral area. The results indicate

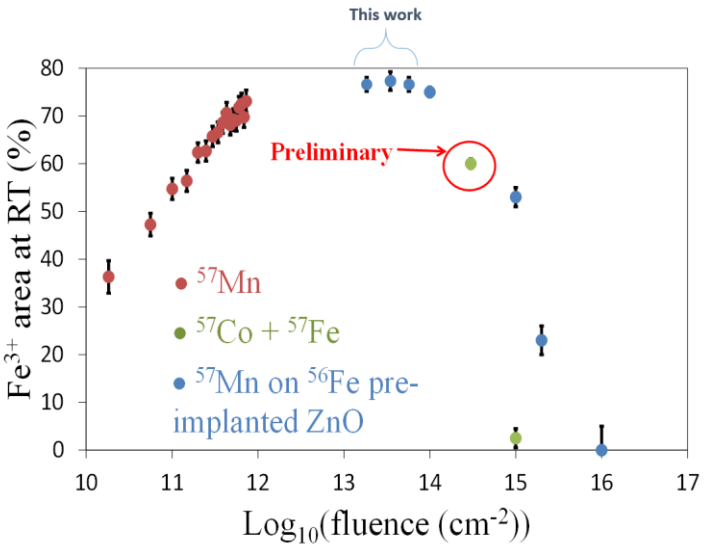


Figure 4.27: Fluence dependence of the area fraction of Fe^{3+} at room temperature. [Adapted from [234]]

that the contribution of Fe^{3+} reaches a saturation for fluences in the range of 10^{12} - 10^{14} ions/cm^2. Thus for fluences below ~ 10^{12} ions/cm^2, the Fe^{3+} state is not stable and the crystal can be 'reset' by annealing as reported by Naidoo *et al* [235]. Above ~10^{14} ions/cm^2 spin-spin interaction occurs between the neighbouring probe atoms as the effective distance between the Fe probe atoms reduces with increasing concentration of dopants. This results in a gradual decrease in the magnetic contribution at fluences >10^{14} ions/cm^2.

4.2.4. Variation of relative area fraction with temperature

The variation of the area fractions of the fitted spectral components for ZnO:^{56}Fe8 as a function of temperature is shown in Figure 4.28.

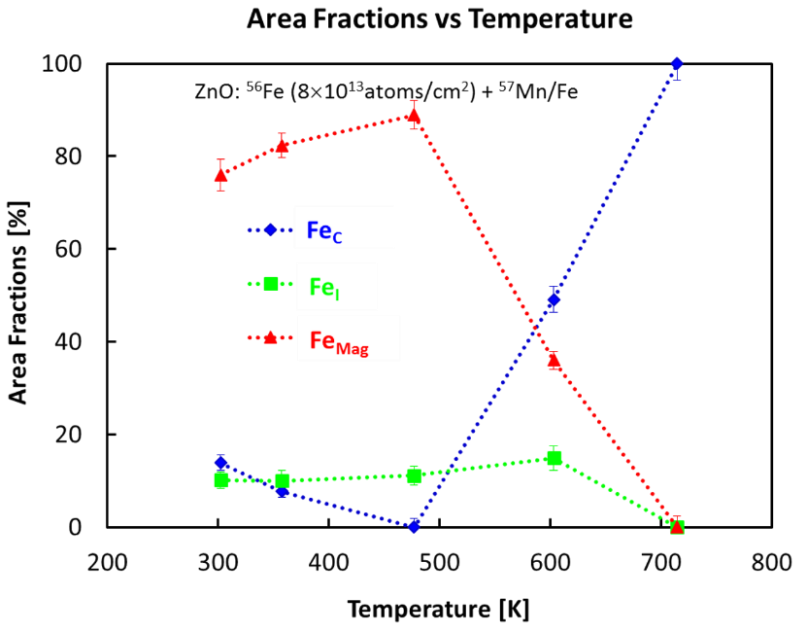


Figure 4.28: Area fractions of the spectral components obtained from the analysis of the ZnO sample pre-implanted with 8×10^{13} ions/cm^2 of ^{56}Fe.

At room temperature, the magnetic component contributes ~76(3)% of the spectral area, with the remaining fraction of ~23(2)% shared between Fe_C and Fe_I. Above RT, the magnetic fraction shows a 15(1)% increase which is accompanied by a corresponding decrease in the area fraction of Fe_C which decreases to zero around 477 K. A similar effect was observed for virgin ZnO in similar experiments [154,153]. However, the area fraction of Fe_I is fairly constant at temperatures below 500 K. The transformation of Fe^{3+} to Fe^{2+} is evident above 500 K, resulting in the spectra being completely dominated by Fe^{2+}. This is accompanied by corresponding

decrease in the area fraction of the paramagnetic Fe^{3+} component that disappears completely at the highest measured temperature of 720 K. This observation can be attributed to spin-spin relaxation processes which are prominent in this temperature range. Thus, at high temperatures the dissociation of impurity-vacancy complexes and mobility of vacancies reduce the effective distance between neighbouring ions and hence spin-spin interaction becomes effective resulting in the disappearance of the magnetic structure due to the paramagnetic Fe^{3+}. Moreover, the collapse of the magnetic hyperfine structure due to fast relaxation times occurring at high temperatures cannot be eliminated. The interstitial fraction decreases to zero above 600 K.

The temperature dependence of the area fractions of the spectral components for ZnO:^{56}Fe5 is presented in Figure 4.29.

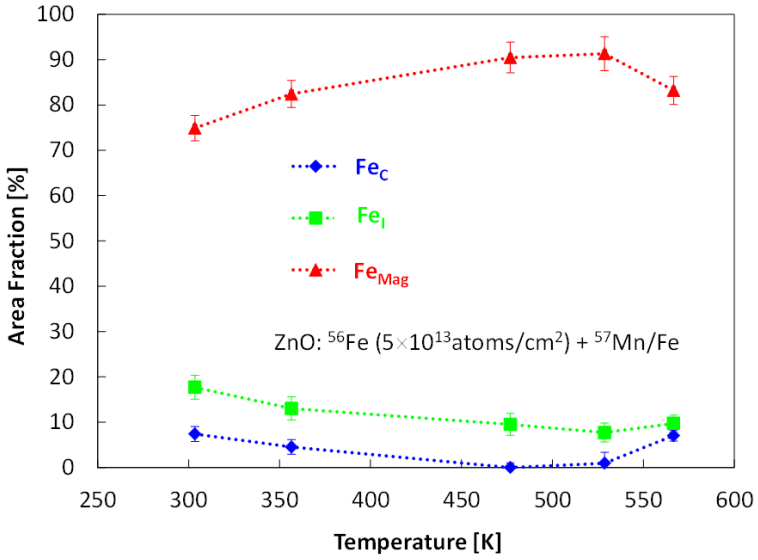


Figure 4.29: Area fractions of spectral components obtained from the analysis of the ZnO sample pre-implanted with 5×10^{13} ions/cm^2 of ^{56}Fe.

At room temperature, the magnetic structure contributes ~77(2) % of the spectral areal, whilst the interstitial component contributes ~17(1)% and the remaining fraction of ~8(1)% to Fe on crystalline sites. The magnetic component increases with increasing temperature to a maximum of ~90(1)% around 530 K and decreases by ~10(1)% at the highest measured temperature of 569 K. The site population of Fe on interstitial sites decreases slightly over the measured temperature range, which is expected since they are recoil produced during the implantation process.

The area fraction of Fe_C approaches ~1% around 477 K then increases to ~10(1)% at the highest measured temperature of 569 K.

The ^{57}Fe emission spectra for the ZnO:$^{56}Fe2$ recorded after $^{57}Mn^{*}$ implantation with the samples held at temperatures of 303 K and 358 K is shown in Figure 4.25. A diagram for the temperature dependence of relative area fractions of the spectral components is not included because of only two data points. At 303 K, the magnetic component contributes ~75(2)% of the spectral area with minor contributions of ~18(1)% and ~7(1)% from the interstitial component and crystalline fraction respectively. The area fraction of the magnetic component increases to ~90(2)% in is observed at 358 K which is accompanied by corresponding decreases in the site populations of the other two components resulting in a combined contribution of ~10(1)%.

4.2.5. Relaxation Rates

Generally, it is expected that the spin lattice relaxation rate increases with increasing temperature because the time required for energy transfer between lattice vibrations and the electron spin decreases [196]. The relaxation rates obtained from this study are shown in Figure 4.30 and are compared with those reported for virgin ZnO and other oxides [153].

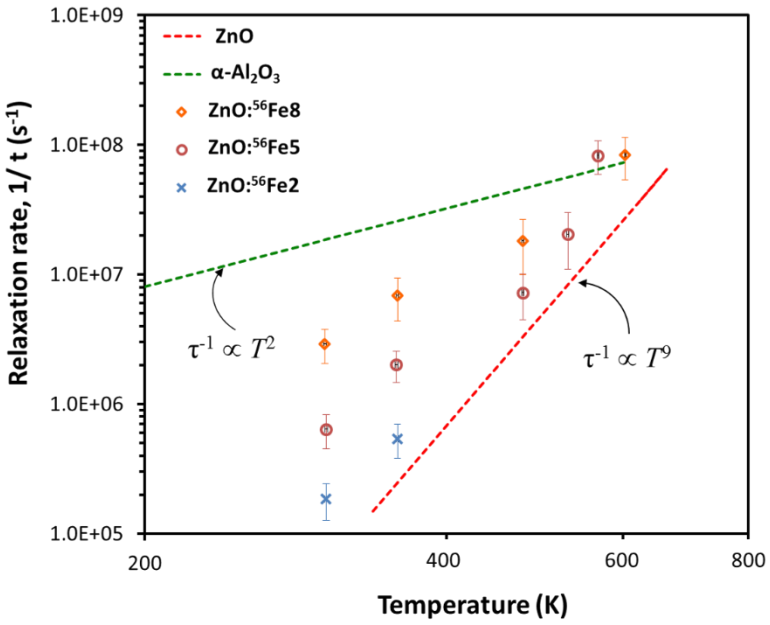


Figure 4.30: Relaxation rates of the pre-implanted ZnO samples as a function of indicated fluence compared with trends in virgin ZnO and α-Al_2O_3. [Adapted from Mølholt *et al.* [153]]

The relaxation rates derived from the analysis of the three pre-implanted samples increases with increasing fluence at equivalent temperatures. This is attributed to the increase in the spin density, which enhances spin-lattice interactions and hence the rate of energy transfer. In addition, our results for the pre-implanted ZnO samples indicate a transition in the relaxation rates from T^9 to a presumably T^2, however, for other pre-implanted samples [236] non-temperature relaxation rates were observed with increasing fluence. This suggests onset of spin-spin interaction as the effective distance between neighbouring Fe atoms decreases with increase in the Fe concentration.

4.2.6. Summary of Results in ^{56}Fe pre-implanted ZnO

An increase in the relaxation rates for the three pre-implanted samples is observed with increasing fluence at corresponding temperatures. This is due to enhanced spin-lattice interactions induced by the increasing spin density resulting from an increase in the concentration of Fe atoms. The spin-lattice relaxation rates show a transition to non-temperature dependent relaxation rates from the unexpected T^9 dependence in virgin ZnO with increasing fluence suggesting that an increase in fluence favours the onset on spin-spin relaxation.

At room temperature, the area fraction of the magnetic component (Fe_{Mag}) for the pre-implanted samples constitutes ~75% of the spectral area and shows no fluence dependence. The area fraction of Fe_C approaches ~1% and zero for the samples pre-implanted with 5×10^{13} ions/cm^2 and 8×10^{13} ions/cm^2, respectively at 477 K. This effect was observed in ZnO virgin samples by Weyer *et al*. [154] and Mølholt *et al*. [153] at similar temperatures.

The presence of the damage component has been observed in other studies [234]with fluences above 10^{14} ions.cm^{-2} resulting in lowering of the magnetic contribution. Moreover, the observed broadening of the Fe_C component for the ZnO:^{56}Fe8 sample could be attributed to implantation induced damage building up in the vicinity of the Fe probe atoms located in crystalline sites. However, the possibility of a relatively small damage component in the form of isolated amorphous zones cannot be completely ruled out as it may be masked by the dominant magnetic component especially for the ZnO:^{56}Fe8 sample.

4.3. ZnO samples implanted with box profile of ^{56}Fe and ^{59}Co

4.3.1. ZnO:^{57}Fe+^{56}Fe

4.3.1.1. Conversion Electron Mössbauer Spectroscopy (CEMS) studies

Several CEMS studies on Fe implanted ZnO have been reported [116,118,169,117,130] where the resulting implantation profile is a Gaussian implantation profile. Thus, dopants are not uniformly distributed across the sample. In this study, as highlighted in section 3.3.3, multiple implantations using different energies were employed to achieve homogenous distribution of Fe impurities to a depth of about 200 nm from the surface of the sample. CEMS measurements were performed at room temperature on the as-implanted sample and after annealing for 30 minutes in a vacuum (with pressure < 10^{-6} mbar) at temperatures of 773 K and 973 K.

A. Analysis, Results and Discussion

The room temperature conversion electron Mössbauer spectra for the as-implanted ZnO sample and after annealing at 773 K are shown in Figure 4.31. The sample was implanted with ^{57}Fe and ^{56}Fe with fluences of 5×10^{15} ions/cm^2 and 4.58×10^{16} ions/cm^2, respectively resulting in a total iron concentration of ~2.5 at.%. The spectra were analysed with three doublets; D1, D2, and D3. The extracted hyperfine parameters with their corresponding line assignments are listed in Table 4.6, where the isomer shifts are given with respect to α-Fe at room temperature.

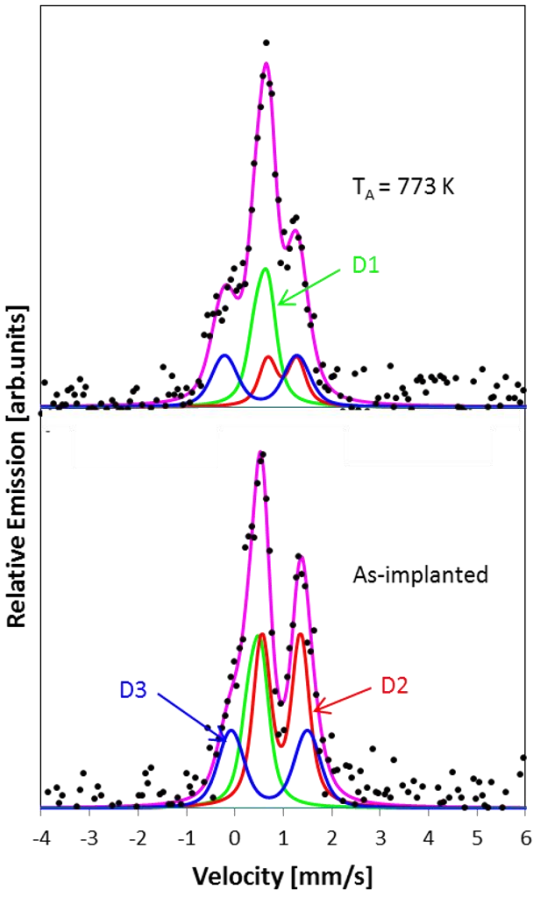


Figure 4.31: CEMS spectra for as-implanted ZnO:^{57}Fe+^{56}Fe sample and after annealing at 773 K

Table 4.6: Hyperfine parameters, Gaussian broadening and area fractions of fitted spectral components for the as-implanted ZnO:^{57}Fe+^{56}Fe sample and after annealing at 773 K.

T_A (K)		δ (mm/s)	ΔE_Q (mm/s)	$\sigma(\delta)$ (mm/s)	Area (%)
As-implanted	D1 (Fe^{3+})	0.41(2)	0.25(2)	0.10(1)	28(1)
	D2(Fe^{2+})	0.96(2)	-0.79(2)	0.11(2)	45(2)
	D3 (Fe_D)	0.71(1)	1.58(1)	0.20(1)	27(1)
773	D1 (Fe^{3+})	0.57(1)	0.25(2)	0.10(1)	43(2)
	D2(Fe^{2+})	0.98(2)	-0.60(1)	0.11(2)	23(1)
	D3 (Fe_D)	0.53(1)	1.49(1)	0.20(1)	34(1)

The spectrum for the as-implanted ZnO:^{57}Fe+^{56}Fe sample shows that a significant area fraction of ~27% is attributed to probe atoms located in implantation induced defect regions (Fe_D) as reflected by the relatively high quadrupole splitting of 1.58(1) mm/s. In addition, the spectral components, D1 and D2 are characteristic of Fe^{3+} and Fe^{2+} on regular crystalline or substitutional Zn sites were utilised. Similar line assignments were reported by Potzger *et al.* [116], for ZnO single crystal implanted with ^{57}Fe at 623 K using an energy of 180 keV and fluence of 4×10^{16} ion/cm^2.

The quadrupole splitting for D2 was determined as -0.79(2) mm/s and such a negative quadrupole splitting of Fe^{2+} on crystalline sites has been reported by Gunnlaugsson *et al.* [155]. This result indicates that the valence contribution to the EFG is more negative compare to the lattice contribution which could be explained by the fact that Fe^{2+} may be in an "almost" tetrahedral symmetry, the x^2-y^2 and z^2 orbitals are at lowest energy. As z^2 gives a negative contribution to V_{ZZ}, [191] it must have lower energy. This is expected from the wurtzite structure, as the tetrahedral symmetry is slightly elongated along the *z*-direction. As a result, the z^2 orbital is expected to be more populated than the x^2-y^2 orbital.

Significant spectral changes are observed after annealing the ZnO:^{57}Fe+^{56}Fe sample at 773 K and this is accompanied an increase in the Fe^{3+}/Fe^{2+} ratio. This result suggests that annealing favours the conversion of ferrous Fe to ferric Fe and is in agreement with the observation reported by Potzger *et al.* [116].

Furthermore, after annealing the sample at 973 K the spectrum displays drastic changes, yielding a very strong asymmetric magnetic structure suggesting a

contribution from Fe in different bonding environments with a total spectral area of ~52% (See Figure 4.32).

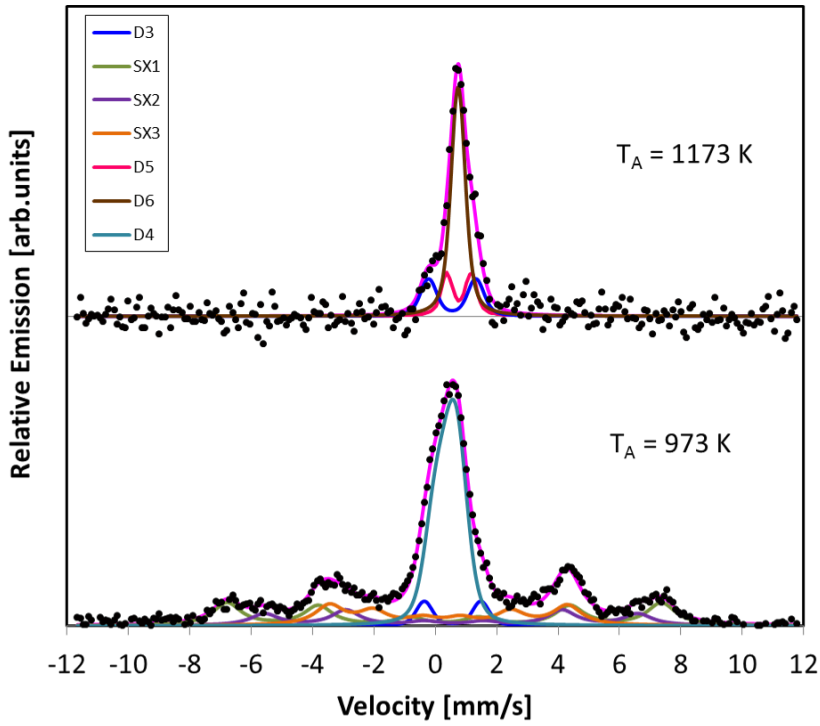


Figure 4.32: CEMS spectra for ZnO:^{57}Fe+^{56}Fe obtained after annealing at 973 K and 1173 K.

The magnetic feature observed at 973 K was analysed with three Lorentzian sextets (SX1, SX2 and SX3) with the intensities of lines 2 and 5 allowed to vary. In addition to sextets and the component due to implantation induced damage, a new quadrupole split doublet D4 was required to obtain acceptable fits to the data. The hyperfine parameters of the spectral components are listed in Table 4.7.

Table 4.7: Hyperfine parameters, Gaussian broadening and area fractions of the fitted spectral components for the ZnO:^{57}Fe+^{56}Fe sample after annealing at 973 K and 1173 K.

T_A (K)		δ (mm/s)	ΔE_Q (mm/s)	ϵ_Q (mm/s)$^+$	$\sigma(\delta)$ (mm/s)	Area (%)	B_{hf} (T)
973	D3	0.56(1)	1.84(2)	-	0.20	5(2)	-
	SX1	0.28(2)	-	0.01(1)	-	23(2)	43.8(4)
	SX2	0.56(2	-	-0.09(2)	-	13(3)	37.7(3)
	SX3	0.32(2)	-	0.22(1)	-	18(2)	24.0(4)
	D4	0.35(1)	0.64(2)	-	0.30	41(2)	-
1173	D3	0.55(2)	1.54(2)	-	0.20	22(2)	-
	D5	0.77(3)	-0.80(2)	-	0.11	18(3)	-
	D6	0.74(2)	0.13(3)	-	0.15	60(2)	-

$^+$ ϵ_Q-quadrupole shift of the sextets

The three sextets may be attributed to Fe^{3+} in different orthorhombic sites of ε-Fe_2O_3 phase which has been reported by several authors [237,238,239,240,241]. ε-Fe_2O_3 is a rare polymorph of iron (III) oxide which exist as nanoparticles [241]; there exist four distinct cation positions (Fe_1, Fe_2, Fe_3 and Fe_4) [240,242] in the orthorhombic crystal structure where Fe_4 is tetrahedrally coordinated, Fe_3 is a regular octahedral site while Fe_1 and Fe_2 are distorted octahedral sites with similar hyperfine parameters [243]. The hyperfine parameters of δ = 0.28(2) mm/s, quadrupole shift (ϵ_Q) = 0.01(1) mm/s and magnetic hyperfine field of ~43.8(5) T for SX1 are indicative of Fe^{3+} in distorted octahedral environments characteristic of either Fe_1 and Fe_2 as was observed by Lancok *et al.* [240] who obtained magnetic hyperfine fields in the range, 43.1-44.6 T. On the other hand, a similar B_{hf} value was reported by Ligenza *et al.* [244] for Fe^{3+} which the authors attributed to the ions in octahedral B sites in the $ZnFe_2O_4$ powder measured in transmission geometry at 4.2 K. However, from room temperature CEMS studies of Fe implanted ZnO [117], secondary phases such as $ZnFe_2O_4$ were formed after annealing at 800ºC represented by a doublet due superparamagnetic effects without magnetic sextets in the spectrum. SX2 is characterised by δ = 0.56(2) mm/s, ϵ_Q = -0.09(2) mm/s and B_{hf} ~37.7(3) T and is assigned to Fe^{3+} on a regular octahedral site (Fe_3). The hyperfine parameters for SX3 are B_{hf} ~24.0(4) T, δ = 0.32(2) mm/s and ϵ_Q = 0.22(1) mm/s which are characteristic of the regular tetrahedral site (Fe_4). The obtained hyperfine fields for Fe_3 and Fe_4 are in good agreement with values of ~38 T and ~25 T, respectively which have been reported by several authors [240,242,239]. In this study, the prominent magnetic feature which is apparent after annealing the sample at 973 K is attributed to nanoparticles in the form of ε-Fe_2O_3. The total Fe concentration in the ZnO:^{57}Fe+^{56}Fe sample is ~2.5 at.%, which eliminates the presence of secondary phases and micro-precipitates that have been reported for Fe implanted ZnO [117,118] and also by Schumm *et al.* [133] who performed Raman spectroscopy measurements on ZnO implanted with Mn concentrations ≥ 8 at.%.

The new broadened quadrupole spilt doublet (D4) contributing ~57% of the spectral area with hyperfine parameters of D4 was determined as δ = 0.35(1) mm/s and ΔE_Q = 0.64(2) mm/s suggest that Fe ion in a 3+ state in the β-Fe_2O_3 [238], also a rare

phase of iron(III) oxide which only exist as nanoparticle. The lower isomer shift value of D4 compared to the values of 0.41(2) mm/s and 0.57(1) mm/s obtained for D1 from measurements on the as-implanted sample and after annealing at 773 K, respectively, indicate an increase in the *s*-electron density at the nuclei of Fe atoms suggesting strengthening of bonds between Fe and neighbouring atoms. The high quadrupole splitting of 0.64(1) mm/s for D4 compared to 0.25(2) mm/s obtained for D1 for the as-implanted sample implies a loss of symmetry around the probe atoms indicating disturbed surrounding environments.

After annealing the sample at 1173 K, the magnetic structure completely disappears and the spectrum consists of implantation induced damage (D3), and two new quadrupole split doublets, D5 and D6. The spectral component D5 has similar hyperfine parameters as D1 obtained for the as-implanted sample which is characteristic of Fe^{2+}. The isomer shift value of 0.74(3) mm/s determined for D6 also suggest Fe^{2+} in a superparamagnetic/paramagnetic state.

4.3.1.2. VSM studies

The observation of a relatively strong magnetic interaction in the vicinity of Fe probe atoms in CEMS measurements after annealing the sample at 973 K prompted investigation of the magnetic properties of the bulk material. Subsequently, magnetisation measurements using a vibrating sample magnetometer were carried out as a function of applied field (±1T) at temperatures of 293 K and 4 K at iThemba LABS, Cape Town.

A. Analysis of VSM Data

Virgin ZnO crystals exhibit diamagnetic behaviour both at 4 K and 293 K, therefore such measurements were performed and used as references. The *M*(*H*) curves for virgin ZnO samples obtained at both temperatures are shown in Figure 4.33. Good fits to the data were achieved with 7^{th} and 9^{th} order polynomials for the magnetisation curves obtained at 4 K and 293 K, respectively. The polynomials (as shown in blue) were used to subtract the diamagnetic component from the magnetisation curves of the implanted and annealed sample.

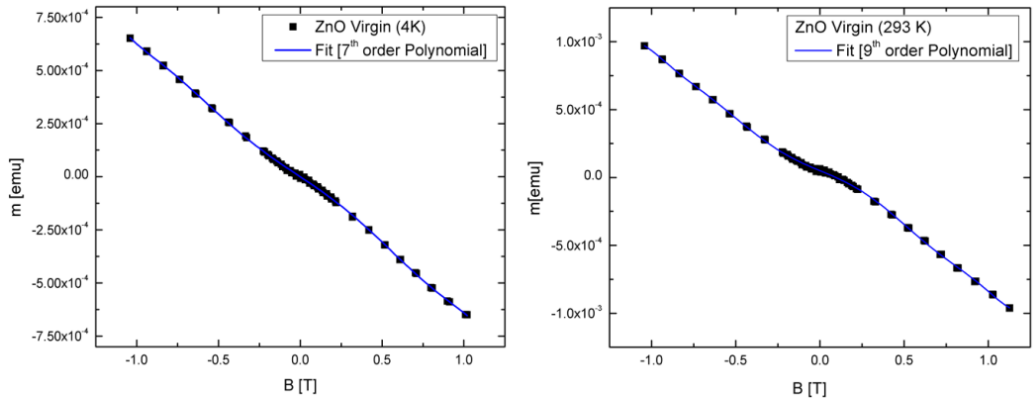


Figure 4.33: Magnetisation curves for the virgin ZnO sample measured at temperatures of 4 K and 293 K and fitted with 7th and 9th order polynomials, respectively.

B. Results and Discussion

The study of magnetic properties of the ZnO:^{57}Fe+^{56}Fe sample after annealing at 973 K were performed using a vibrating sample magnetometer and results of the magnetic moment measurements are shown in Figure 4.34 as a function of magnetic field.

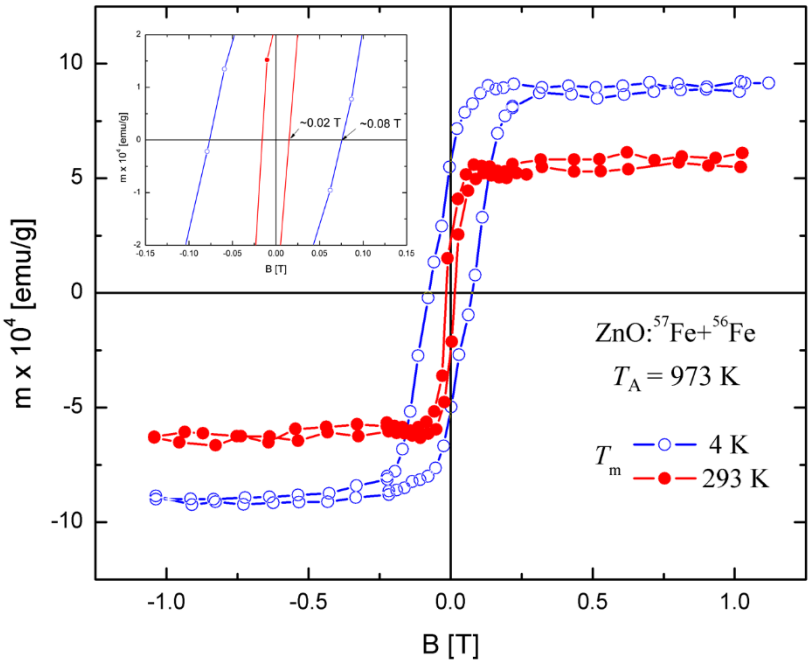


Figure 4.34: Magnetisation curves of ZnO:^{57}Fe+^{56}Fe measured at 4 K and 293 K after annealing at 973 K.

The sample shows strong signatures of ferromagnetic behaviour as is evident by the presence of hysteresis loops at both temperatures. The diamagnetic component was subtracted in order to obtain information on the magnetic properties of the Fe impurities in ZnO. The magnetisation curve measured at 293 K gives a saturation

magnetic moment of ~5.8×10^{-4} emu/g with a very small coercive field of ~0.02 T as observed from a separation between the magnetisation and demagnetisation curves. However, field reversal measurements at 4 K reveals a very strong ferromagnetic behaviour with a saturation magnetisation of ~9.2×10^{-4} emu/g and also a relatively large coercive field of ~0.08 T, resulting in the larger separation between the positive and negative legs of the hysteresis loop. In addition, at 4 K, the sample is also characterised by a remanent magnetisation of ~5.7×10^{-4} emu/g, which account for ~62% of the saturation magnetisation. At lower temperatures, relatively large values for the coercive field, remanent magnetisation and saturation magnetisation are expected because spin orientation is less affected by the thermal vibrations compared to room temperature which is consistent with Curie's law.

4.3.2. ZnO:^{57}Fe+^{59}Co

4.3.2.1. CEMS Results

A second box profile ZnO sample was prepared using ^{59}Co instead of ^{56}Fe (ZnO:^{57}Fe+^{59}Co) in order to investigate the effect of a different transition element on the magnetic properties. Implantation energies were chosen to achieve a similar homogeneous distribution of dopants to a depth of approximately 200 nm. Figure 4.35 presents room temperature CEMS spectra for the as-implanted ZnO: ^{57}Fe+^{59}Co sample and after annealing at indicated temperatures.

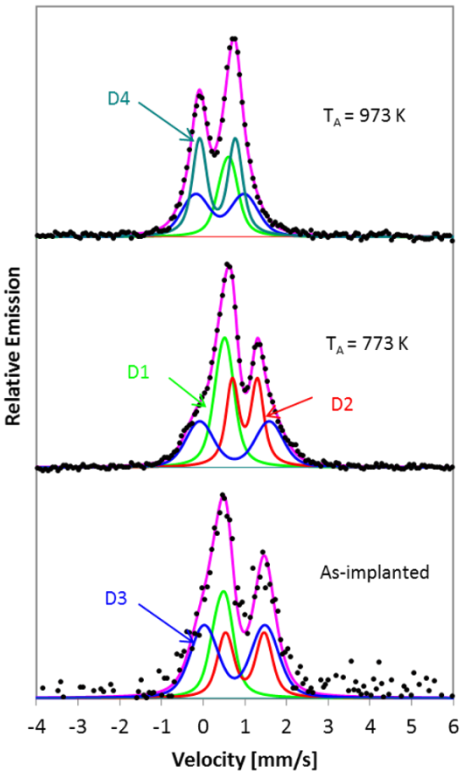


Figure 4.35: Room temperature CEMS spectra for the as-implanted ZnO:^{57}Fe+^{59}Co sample and after annealing at 773 K and 973 K.

The data were fitted with three doublets similar to the approach adopted for the ZnO:^{57}Fe+^{56}Fe sample. The extracted hyperfine parameters of the fitted spectral components with assignments are listed in Table 4.8. The isomer shifts are given with respect to α-Fe at RT.

Table 4.8: Hyperfine parameters, Gaussian broadening and area fractions of the fitted spectral components for the ZnO:^{57}Fe+^{59}Co sample.

T_A (K)	Components	δ (mm/s)	ΔE_Q (mm/s)	$\sigma(\delta)$ (mm/s)	Area (%)
As-Implanted	D1 (Fe^{3+})	0.43(1)	0.25(1)	0.12(1)	27(1)
	D2 (Fe^{2+})	1.00(1)	-0.93(2)	0.13(1)	30(2)
	D3 (Fe_D)	0.75(2)	1.46(1)	0.27(2)	43(2)
773	D1 (Fe^{3+})	0.47(1)	0.25(2)	0.12(1)	35(1)
	D2 (Fe^{2+})	0.98(1)	-0.66(2)	0.07(1)	38(1)
	D3 (Fe_D)	0.75(2)	1.74(1)	0.27(2)	28(2)
973	D1 (Fe^{3+})	0.56(1)	0.23(1)	0.12(1)	25(1)
	D4 (Fe^{3+})	0.34(1)	0.88(1)	0.10(1)	57(2)
	D3 (Fe_D)	0.40(1)	1.29(2)	0.27(1)	18(1)

The as-implanted spectrum is dominated by doublet D3 assigned to Fe in defect sites in the ZnO crystal lattice contributing ~43(2)% of the spectral area. The hyperfine parameters of D3 are characteristic of Fe^{2+}. Moreover, the spectral component D2 has an isomer shift of δ = 1.00(1) mm/s which is also typical of Fe^{2+}, while D1 has an isomer shift, δ = 0.43(1) mm/s and a quadrupole splitting of ΔE_Q = 0.25(1) mm/s which is typical of Fe^{3+} on regular lattice sites.

After annealing the sample at 773 K, the area fraction of the damage component (D3) decreases to ~28(2) %, while corresponding increases of ~8% are observed for both D1 and D2. At this annealing temperature, no significant change in the Fe^{3+}/Fe^{2+} ratio was observed.

After annealing the sample at 973 K, no magnetic features are observed. However a change in the asymmetry of the spectrum is evident, with the right leg being more intense than the left leg. A similar behaviour was observed in ZnO samples implanted with ^{57}Fe to fluences of 4 at.% and 8 at.% [245]. At this annealing temperature, doublet D2 which is attributed to Fe^{2+} on crystalline regular sites disappears, a similar observation was evident for the ZnO:^{57}Fe+^{56}Fe sample. A new quadrupole split doublet, D4 with an area contribution of ~57% is clearly visible in the spectrum. The hyperfine parameters of D4 were extracted as δ = 0.34(1) mm/s and ΔE_Q = 0.88(1) mm/s characteristic of Fe^{3+} in the β-Fe_2O_3 [241,239] where Fe^{3+} ions are located at non-equivalent octahedral sites in a body-centred cubic structure. At this annealing temperature, the spectrum is dominated by Fe^{3+} in different

environments as reflected by the different hyperfine parameters of D1 and D4, with the remaining fraction of ~18(1)% in implantation induced damage regions. The absence of magnetic features in Mössbauer spectroscopy suggests that the absence of ε-Fe_2O_3 which could be attributed to the low Fe concentration (0.5 at.%) in this sample limiting the interaction with neighbouring lattice atoms and hence formation of ε-Fe_2O_3 nanoparticles. The absence of magnetic structure in CEMS measurements after annealing the sample at 973 K did not warrant any magnetisation measurements. However, this does not rule out the magnetic interaction between Co and O atoms, since the presence of Co_3O_4 complexes has been suggested by Matei *et al.* [131] and also the formation of small metallic Co clusters upon annealing at 550°C has been reported [246] for ZnO doped with ≤ 5 at.% of Co.

4.3.3. Summary of results in box profile implanted ZnO samples

Room temperature conversion electron Mössbauer spectroscopy measurements on ZnO samples with a box implantation profile; ZnO:^{57}Fe+^{56}Fe and ZnO:^{57}Fe+^{59}Co with total concentrations of ~2.5 at.% were carried out on the as-implanted samples and after annealing up to 973 K. The spectra for the as-implanted samples were analysed with three doublets, one doublet attributed to Fe on implantation induced damage (Fe_D) with the other two assigned to Fe^{2+} and Fe^{3+} on substitutional Zn sites or regular crystalline lattice sites.

Significant spectral changes are observed after annealing the ZnO:^{57}Fe+^{56}Fe sample at 773 K resulting in an increase in the Fe^{3+}/Fe^{2+} ratio. For a similar measurement on the ZnO:^{57}Fe+^{59}Co sample, this ratio remained fairly constant however a significant decrease in the area fraction of the spectral component assigned to implantation induced damage is observed as compared to the former case. The increase in the Fe charge ratio with annealing temperature suggests that heat treatment favours the oxidation or charge transfer from Fe^{2+} to Fe^{3+}.

After annealing the ZnO:^{57}Fe+^{56}Fe sample at 973 K, a strong magnetic feature is observed and was analysed with three Lorentzian sextets with signatures of Fe^{3+} in ε-Fe_2O_3 phase located on: (i) distorted octahedral site (Fe_1/Fe_2), (ii) regular octahedral site (Fe_3) and (iii) regular tetrahedral sites (Fe_4). Zinc ferrite ($ZnFe_2O_4$)

is excluded because it is superparamagnetic at room temperature and yields a quadrupole split doublet in Mössbauer spectroscopy measurements. On the other hand, the spectrum for ZnO:^{57}Fe+^{59}Co did not show any magnetic structure, but a 'switch' in the asymmetry of the spectrum was observed at the same temperature. This required a new quadrupole split component as observed in the ZnO:^{57}Fe+^{56}Fe, with hyperfine parameters typical of Fe^{3+} suggesting a β-Fe_2O_3 phase. However, the presence of ferrites such as $Zn_xFe_{3-x}O_4$, $Zn_xFe_{2-x}O_3$, or any other highly defective ferric oxide cannot be completely ruled out as a range of nanoparticle size could exist in the sample. The complete disappearance of the magnetic structure after annealing at 1173 K suggests that the oxide formed upon annealing at 973 K can be destabilised at relatively high annealing temperatures (1173 K).

In light of the magnetic structure detected in the Mössbauer measurements on the ZnO:^{57}Fe+^{56}Fe sample, magnetic characterisation investigations were conducted using a vibrating sample magnetometer at 4 K and 293 K. This sample showed a strong ferromagnetic signal at 4 K with a coercive field of about ~0.08 T and remanent magnetisation which is ~62% of the measured saturation magnetisation of $\sim 9.2\times10^{-4}$ emu/g. A field reversal measurement at room temperature (293 K) showed a relatively small hysteresis loop with a coercive field of ~0.02 T and remanent magnetisation of $\sim 2.0\times10^{-4}$ emu/g, which is ~34% of the saturation magnetisation.

4.4. Overview of Results

This chapter has presented the data analysis and discussion of results. The major findings are highlighted in the summary below:

- Paramagnetic behaviour is observed from emission Mössbauer investigations in GaN, AlN and ^{56}Fe pre-implanted ZnO samples implanted ^{57}Fe with fluences of $\sim 3\times10^{12}$ ions/cm^2 via the decay of $^{57}Mn^*$. The paramagnetic effect stems from the presence of high spin Fe^{3+} weakly coupled to the lattice which shows spin-lattice relaxation effects.
- The temperature dependent spin-lattice relaxation rates were obtained from a semi-empirical model utilizing Blume-Tjon sextets which approximately

follows a T^2 temperature dependence, characteristic of a two-phonon Raman process in GaN and AlN.

- No magnetic structure is observed in the spectra for InN, which could be explained by the absence of high spin Fe^{3+}.
- The anisotropy of the central region of the spectra for all nitrides at emission angles of (θ_γ) of 0° and 60° and the corresponding extracted hyperfine parameters suggest that Fe probe atoms located in regular crystalline sites are assigned to; (i) covalently bonded Fe (III) on purely substitutional III sublattice tetrahedrally coordinated with four N atoms (Fe_S) and (ii) the majority to the Fe^{2+} configuration on or near substitutional sites associated with vacancy type defects. This confirms that majority of the probe atoms are located on substitutional III sites and/or slightly displaced around the lattice site.
- In nitrides, a relatively small fraction of Fe atoms are observed to be located in implantation induced isolated amorphous zones (Fe_D) and lattice recovery in these regions occurred at temperatures between 400 and 500 K. In addition, the absence of anisotropy of Fe_D attests that the probe atoms are located in isolated amorphous or damage regions. This result confirms the radiation hardness of III-nitrides compared to cubic III-Vs where the implantation induced damage dominated the spectra over the measured temperature range in similar measurements.
- Different annealing stages are observed in nitrides marked by a decrease in the spectral area contributions of Fe_C. In GaN, a significant change in the area fraction is apparent in the temperature range, 500-600 K and is attributed to long-range mobility of Ga vacancies. In the case of AlN, two annealing stages are evident in the temperature ranges, 150-260 K and $T \geq 306$ K, whilst for InN similar stages were observed in the range, 240-380 K and above 500 K which could be explained by a dissociation of impurity-vacancy related defects coupled with mobility of the resulting vacancies and Fe probes moving towards pure substitutional sites. A small increase in the contribution of Fe_C in InN around 470 K results from the lattice recovery of Fe atoms in isolated amorphous zones.

- The absence of recoil produced interstitials in nitrides is tentatively attributed to displacement energies greater than the average recoil energy 40 eV given to ^{57}Fe in the $^{57}Mn^{*}$ β-decay. As a result the daughter ^{57}Fe remains on the substitutional lattice site originally occupied by $^{57}Mn^{*}$ upon implantation.
- The spin–lattice relaxation rates of Fe^{3+} in the ^{56}Fe pre-implanted ZnO samples increase with increasing fluence at equivalent temperatures. In addition, the increase in fluence is accompanied by a transition from T^{9} to non-temperature dependent relaxation rates suggesting the onset of spin-spin interactions. The contribution (~75%) of Fe^{3+} at room temperature for the pre-implanted ZnO samples saturates within the fluence range of 10^{13}-10^{14} ions/cm^2.
- The central region of spectra obtained for the ^{56}Fe pre-implanted ZnO samples was analysed and interpreted with two quadrupole split doublets assigned to Fe^{2+} on Zn sites (Fe_C) and recoil produced interstitial sites (Fe_I) in a similar way to previous studies in virgin ZnO. Moreover, the absence of implantation induced isolated amorphous regions in pre-implanted samples is attributed to the self-annealing tendency in ZnO during the implantation process for fluences below 10^{14} ions/cm^2.
- The as-implanted CEMS spectra for homogeneous implantation in ZnO with fluences of ~2.5 at.% did not show any magnetic features but were characterised with Fe in both 2+ and 3+ states and the remaining Fe fraction to implantation induced damage. An increase in the Fe^{3+}/Fe^{2+} ratio is observed for the ZnO:^{57}Fe+^{56}Fe sample after annealing at 773 K while the ratio does not show significant change in the ZnO:^{57}Fe+^{59}Co sample.
- A strong magnetic structure is evident in the spectrum of ZnO:^{57}Fe+^{56}Fe after annealing at 973 K resulting from the formation ε-Fe_2O_3 nanoparticles. Magnetisation curves obtained at 4 K and 293 K using VSM are characterised by ferromagnetic signals with coercive fields of ~0.08 T and ~0.02 T coupled with remanent magnetisation fields which are ~62% and ~34% of the saturation magnetisation, respectively. However, after annealing the sample at 1173 K, the magnetic feature completely disappears resulting in Fe^{2+} dominating the spectrum.

- The ZnO:^{57}Fe+^{59}Co sample did not reveal any magnetic behaviour after annealing at 973 K, but a "switch' in the overall asymmetry of the spectrum could be explained by Fe^{3+} in different local environments as result of the heat treatment. The absence of any magnetic structure in the spectra for the ZnO:^{57}Fe+^{59}Co sample is attributed to the absence of ε-Fe_2O_3 because of low fluence (0.5 at.%) employed but does not rule out the presence of Co clusters and/or Co_3O_4 which are not detectable by ^{57}Fe Mössbauer spectroscopy.

- Room temperature conversion electron Mössbauer spectroscopy measurements for box profile implanted ZnO samples did not show any magnetic structure while emission Mössbauer spectroscopy measurements on extremely dilute systems reveal a dominant magnetic structure. This could be explained by spin-spin interactions between neighbouring Fe atoms and/or the presence implantation induced damage due to higher fluences of implanted stable isotopes.

Finally, an outlook and recommendation for further studies are proposed in the next chapter with concluding remarks.

Chapter 5

Concluding Remarks

Amid several controversial reports on the nature and origin of magnetism in doped semiconductors, emission Mössbauer spectroscopy results of extremely dilute Fe (~10^{-4} at.%) implanted GaN and AlN show that these materials exhibit magnetic features in the 'wings' of the spectra. This magnetic structure could be explained by the presence of paramagnetic Fe^{3+} with S=5/2 weakly coupled to the lattice. The observed spin-lattice relaxation with T^2 temperature dependent is typical of a two-phonon Raman process which is expected in the measured temperature range. Spin-spin interactions could be eliminated because the low fluences (~3×10^{12} ions/cm^2) employed limit the effective distance between the neighbouring probe atoms and also prevent the formation of metallic clusters/precipitates. Moreover, InN did not reveal any magnetic behaviour and this could be explained by the absence of high spin Fe^{3+}.

Emission Mössbauer studies on nitrides using $^{57}Co^{*}$ prepared by surface ionisation at ISOLDE and implanted for offline home laboratory based measurements were initially proposed but were unsuccessful due to low yields in the prepared samples for two consecutive years. A minimum activity of ~3 μCi is required for a series of measurements in a year [247], however, the activity in the prepared samples was found to be ~0.016 μCi from gamma spectroscopy measurements. A relatively good beam was produced in 2010 and successful measurements were done on a prepared ZnO [155] sample. Future similar studies on nitrides are required as they will aid in investigating the behaviour and understanding of a different transition metal in these materials. In addition, future studies on (Al,Ga)N have been proposed for measurements at ISOLDE motivated by different spectral features and hyperfine parameters in GaN and AlN [248].

In ^{56}Fe pre-implanted ZnO, similar results were observed as in earlier measurements on virgin ZnO [151], where paramagnetic Fe^{3+} (S=5/2) is responsible for the magnetic phenomenon, however, an increase in fluence favours temperature

independent spin-spin interactions. The contribution of Fe^{3+} at room temperature in all pre-implanted samples did not show any fluence dependence for the three fluences, while the crystal field splitting values followed an approximately linear trend with increasing fluence. However, more measurements in the fluence range 10^{12}-10^{15} ions/cm^2 are required in addition to low temperature measurements for in depth studies of these effects.

For Fe concentrations of the order of 2.5 at.% in ZnO with a homogenous distribution of ions to a depth of 200 nm, ferromagnetic behaviour is observed after annealing at 973 K and is attributed to the formation of nanoparticles of ε-Fe_2O_3. This is supported by hysteresis loops detected in magnetisation measurements using VSM with coercive fields of ~0.08 T at 4 K and ~0.02 T at 293 K. The corresponding remanent magnetisation fields measured are ~62% and ~34% of the saturation magnetisation at 4 and 293 K, respectively. However, the sample implanted with ^{59}Co in place of ^{56}Fe did not show any magnetic features, which could be limited by the element specificity of ^{57}Fe Mössbauer spectroscopy since the presence of Co clusters and/or Co_3O_4 is envisaged. Furthermore, for a better understanding of the structural properties and magnetic character of Co and Fe in these samples, synchrotron techniques such as synchrotron X-ray diffraction (SR-XRD) and X-ray magnetic circular dichroism (XMCD) would be good candidates for future investigations, coupled with high resolution transmission electron microscopy (HR-TEM). In addition, field cooled and zero-field cooled magnetisation measurements could also be used to ascertain the origin of hysteresis and distinguish between real ferromagnetic behaviour and other effects such as superparamagnetism or spin glass effects below a blocking temperature [249].

Complementary vibrating sample magnetometer measurements were planned and are feasible on box profile implanted samples because of the relatively higher concentration of transition metals (~2.5 at.%); similar measurements may not be possible on the samples with extremely dilute doping (~10^{-4} at.%) as such concentrations are below the sensitivity limit of the magnetometer. Emission Mössbauer spectroscopy using short-lived radioactive isotopes is perhaps the most

viable option of probing the magnetic structure at these very low concentration levels (10^{-3}-10^{-4} at. %).

The central region in the spectra for all nitrides showed anisotropic behaviour typical of Fe probe atoms located on regular lattice sites. This region was analysed with two quadrupole split doublet consistent with the angular dependence assigned to covalently bonded Fe (III) on purely substitutional sites on the III sublattice and Fe^{2+} on or near substitutional sites associated with vacancy related defects. Moreover, a third asymmetric doublet only present below 500 K was also included and assigned to Fe in implantation induced isolated amorphous zones based on the absence of anisotropy. These materials revealed small area fraction (≤ 7%) of probe atoms in isolated damaged regions attesting to the radiation hardness of III nitrides compared to cubic III-V's where this component dominated the spectra. The observation of angle dependence in the central region of the spectrum supports the argument that majority of the Fe probe ions are located on crystalline sites either pure substititutional or associated with vacancy related defects. Emission channelling results [105] confirm that the majority of the Fe probe ions are on substitutional sites in GaN. From similar experiments, heavy ions (^{119}In and ^{89}Sr) were found to be slightly displaced from the perfect substitutional site.

In ^{56}Fe pre-implanted ZnO, the central part of eMS spectra obtained using $^{57}Mn^{*}$ was analysed with two doublets assigned to Fe^{2+} on substitution Zn sites and also Fe atoms on interstitial sites similar to earlier virgin ZnO measurements. However, for stable implantation with a relatively higher fluence (~2.5 at.%), Fe in both charge states of 3+ and 2+ were located on regular crystalline sites and also in implantation induced damage. Heat treatment of the samples favoured the oxidation from ferrous to the ferric state, which dominates at the highest annealing temperature of 973 K, but damaged regions do not completely recover after annealing at this temperature.

Vacancy related complexes associated with Fe atoms on or near substitutional sites seem to dissociate and become mobile at temperatures above ~400 K in nitrides. These vacancy complexes, their dissociation and resulting vacancies did not play an active role in the observed paramagnetic and spin-lattice relaxation effects.

The absence of recoil produced interstitials in nitrides is tentatively attributed to displacement energies larger than the mean recoil energy of 40 eV given to the daughter ^{57}Fe in the β-decay of ^{57}Mn*. Surprisingly, there is no consensus on reported threshold displacement values in literature in both nitrides and ZnO hence there is still a need for an effective determination of the E_d values both from theory and experiments. The absence of Fe on interstitial sites from this study is in agreement with emission channelling studies [105].

In conclusion, paramagnetism has been observed in extremely dilute systems stemming from high spin Fe^{3+} weakly coupled to the lattice showing slow spin-lattice relaxation. On the other hand, ferromagnetic behaviour is evident after annealing for implantation fluences in the range predicted by theory [19]. This is attributed to the formation of 'unstable' nanoparticles of ferric oxide and/or other zinc ferrites, which can be destabilised by further annealing at higher temperatures. In light of the results presented in this thesis and other work cited herein, observation of real carrier mediated dilute magnetic behaviour in these semiconductors which may persists at and above room temperature has not yet been realised since Dietl's theoretical prediction more than a decade ago. The proposed potential practical applications in spintronic devices are still limited with the leading candidate, (Ga,Mn)As with a T_c ~185 K [29].

Appendix A: Basics on Magnetism

A.1. Magnetism

The origin of magnetism depends on spin motions of electrons, their orbital arrangements and how they interact with each other. In general, almost all materials are magnetic to some extent, the distinction stems from the fact that there exists very strong interactions between atomic magnetic moments while in others no collective interactions exist. As a result, there are different types or classes of magnetism, which can be best described by how materials respond in the presence of a magnetic field. The magnetic behaviour of materials can be classified within the five categories: diamagnetic, paramagnetic, ferrimagnetic, ferromagnetic or antiferromagnetic. However, there is need for a quantity that can describe a material's magnetic response in an applied field. Magnetic susceptibility (χ) characterises the magnetic behaviour of a material through the relation

$$M = \chi H_0, \tag{A. 1}$$

where M is the magnetisation (or magnetic moment per unit volume) and H_0 is the applied or external magnetic field.

A.1.1. Classes of magnetic materials

A.1.1.1. Diamagnetism

Diamagnetism is observed in materials in which the atoms have no net magnetic moment, with all electron orbitals completely filled (i.e. without any unpaired electrons). Figures A.1 (a) and (b) show the lattice arrangement in crystalline and amorphous materials without a net magnetic moment from the atoms. In the presence of an external magnetic field, a magnetic flux is induced which counters the change in the applied field resulting in an anti-parallel magnetisation (i.e. negative magnetism). This is due to a non-cooperative behaviour between the orbiting electrons, as a result a negative and temperature independent susceptibility is observed for diamagnetic materials. The constant susceptibility with increasing temperature and the $M(H)$ curve showing negative magnetisation for a diamagnetic material are illustrated in Figures A.1 (c) and (d), respectively.

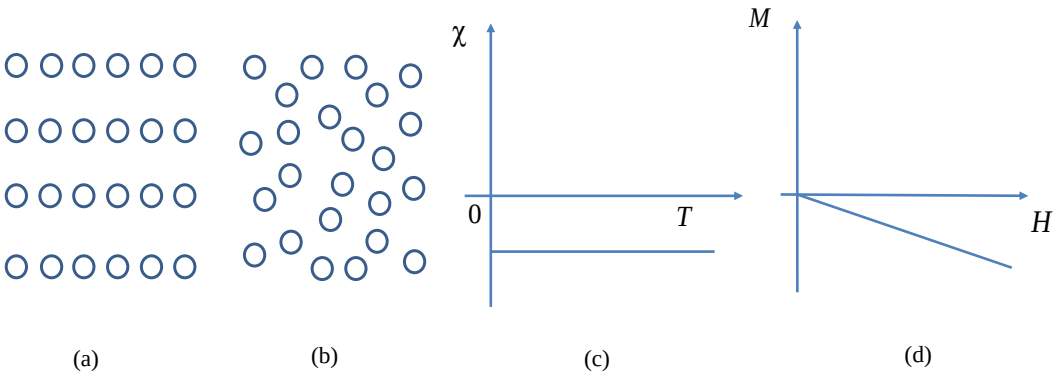


Figure A.1: Diamagnetism: (a) Crystalline and (b) amorphous lattice showing atoms without net magnetic moments, (c) Temperature dependence of susceptibility and (d) Field dependence of magnetisation of a diamagnetic material.

A.1.1.2. Paramagnetism

Paramagnetism is characteristic of materials with atoms, molecules or ions that have partially filled orbitals with unpaired electrons resulting in a net magnetic moment. The lattice arrangements of atoms in both crystalline and amorphous structures are depicted in Figures A.2 (a) and (b), respectively, showing randomly oriented magnetic moments.

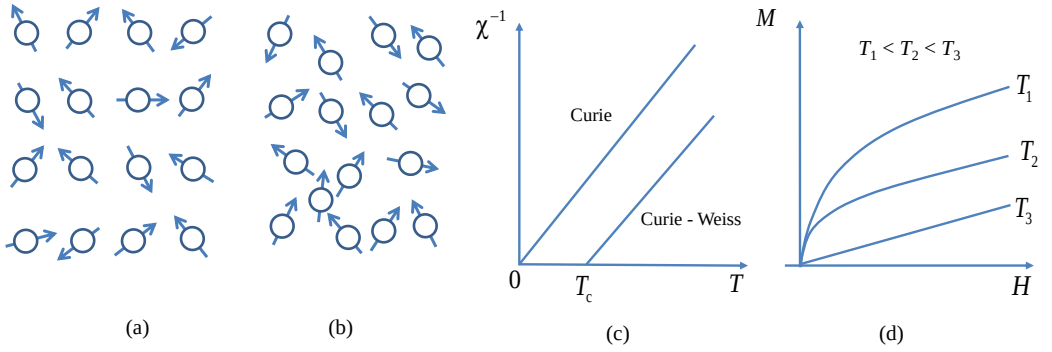


Figure A.2: Paramagnetism: Spin lattice arrangements in (a) crystalline and (b) amorphous structures showing spins randomly oriented, (c) Temperature dependence of χ^{-1} (d) *M*(*H*) curve at different temperatures.

An external magnetic field will induce a flux that tends to align the spins in the direction of the applied field. The induced magnetisation is proportional to the applied magnetic field and remains positive. Thus a positive magnetisation and in turn a positive susceptibility is observed in paramagnetic materials. However, the susceptibility decreases with increasing temperature. Figure A.2 (c) shows the thermal dependence of χ^{-1}. It obeys the *Curie-Weiss law* given by the expression,

$$\chi = \frac{C}{T - T_c}, \tag{A.2}$$

where C is the Curie constant and T_c is the Curie temperature. The magnetisation drops to zero when the external field is removed, because the thermal vibrations causes the spin to randomly orient. Figure A.2 (d) illustrates the magnetic behaviour of a paramagnetic material as a function of external magnetic field at different temperatures. Similar to diamagnetism, there is no cooperative interaction between the individual magnetic moments and thus no net magnetisation effects are observed.

A.1.1.3. Ferrimagnetism

Ferrimagnetism is most common in ionic compounds where opposing spin orientation results from the host ions on two different lattice sites. The resultant non-zero spontaneous magnetisation depends on which spin orientation has a stronger magnetisation with respect to the opposing orientation. The spin lattice arrangement is depicted in Figure A.3 (a) showing sub-lattices A and B with unequal opposing spins. An increase in the temperature influences the thermal motion of spins and brings about disorder in the spin arrangements. This results in completely randomly orientated spins at the Curie temperature, when the material becomes paramagnetic. The temperature dependence of both the reciprocal of the susceptibility and the spontaneous magnetism are shown in Figures A.3 (b) and (c) respectively, while the Figure A.3 (d) shows the effect of increasing the field on the magnetisation of a ferrimagnetic material at different temperatures.

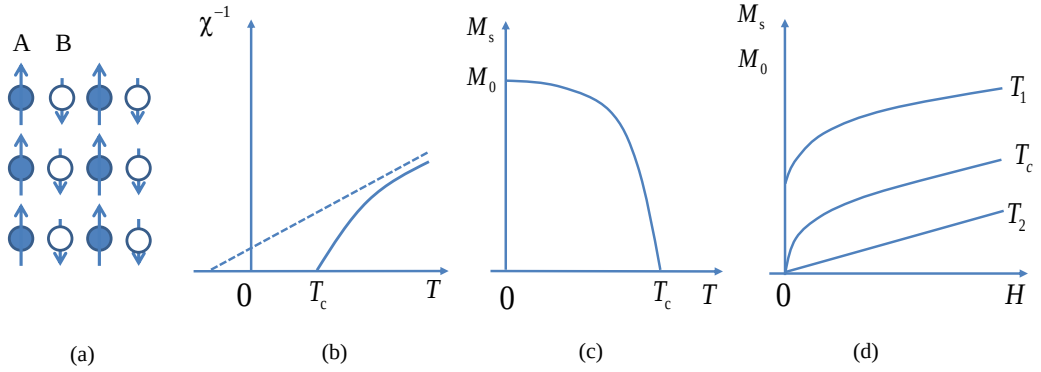


Figure A.3: Ferrimagnetism: (a) Spin lattice arrangement, (b) Temperature dependence of χ^{-1}, (c) Variation of spontaneous magnetisation with temperature, (d) $M(H)$ curve at different temperatures.

A.1.1.4. Ferromagnetism

Ferromagnetism is the strongest type of magnetism and is associated with materials that exhibit spontaneous magnetisation stemming from the alignment of neighbouring magnetic moments in domains even in the absence of an applied magnetic field as shown in Figure A.4 (a). The spontaneous magnetisation is a co-operative occurrence arising from the ordering of magnetic moments due to *exchange interactions* between the electron spins. A magnetic domain is a small region which has uniform magnetisation, i.e. containing a number of atoms with magnetic moments that are aligned in parallel. The spin magnetic moments of all atoms in a domain are oriented in the same direction (see Figure A.4 (b)), but the magnetisation directions of different domains of a ferromagnetic material are random as illustrated in Figure A.4 (c). The resultant magnetisation is zero on a macroscopic scale and the material is said to be demagnetised.

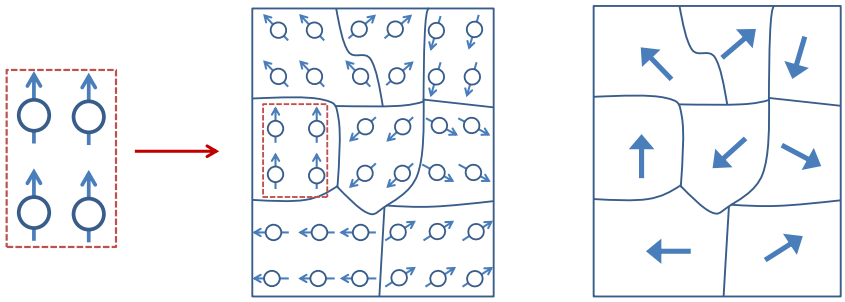


Figure A.4: (a) Neighbouring moments in a ferromagnetic material, (b) Parallel alignment of neighbouring spins in different magnetic domains, (c) Overall spontaneous magnetisation in magnetic domains.

In the presence of an external field, the magnetisation increases up to a saturation value (M_s). When the applied field is decreased or reversed, the magnetisation of the ferromagnetic material decreases without tracing the original path, that is, magnetisation and demagnetisation processes are irreversible. The lack of retraceability of a magnetisation curve is a characteristic of ferromagnetic materials known as *hysteresis*. This property is related to the presence of magnetic domains which when oriented in one direction, energy is required to reverse their orientation. The ability to retain magnetism in ferromagnetic materials is useful in magnetic 'memory' hence the use of iron and chromium oxides in magnetic storage for computer hard drives and audio tape recording. Figure A.5 shows a hysteresis loop

which contains information on intrinsic and extrinsic properties of a ferromagnetic material.

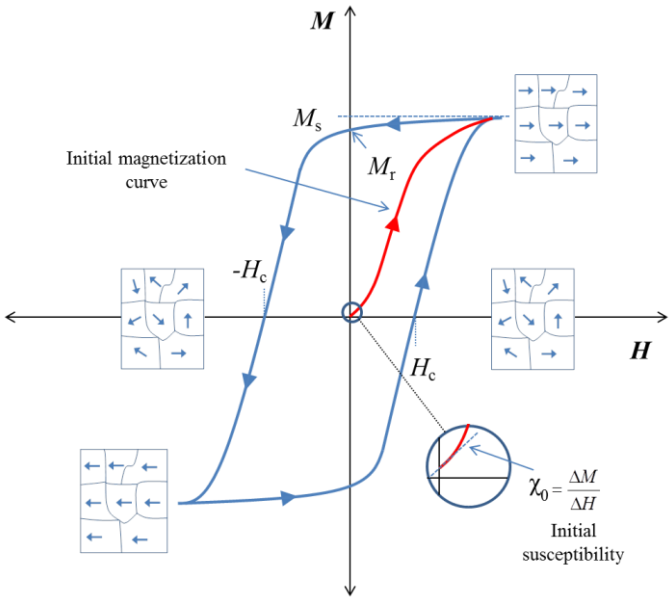


Figure A.5: Magnetisation curve for a ferromagnetic material, showing hysteresis loop and arrangement of magnetic domains.

The remanent or 'left over' magnetisation (M_r) is a measure of the materials' ability to retain magnetisation when the external magnetic field has been removed. Coercive field (H_c) is the external field required to counteract the remanent magnetisation in a ferromagnetic material and reduce the magnetisation to zero. The thermal dependences of χ^{-1} and spontaneous magnetisation in a ferromagnetic material are illustrated in Figures A.6 (a) and (b), respectively, while the field dependence of magnetisation at different temperatures is show in Figure A.6 (c).

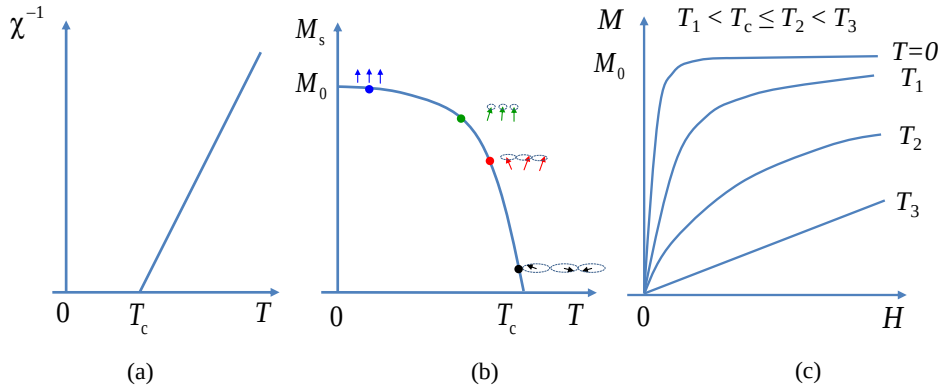


Figure A.6: Ferromagnetism: (a) Temperature dependence of χ^{-1}, (b) Variation of spontaneous magnetisation with temperature, (c) *M*(*H*) curve at different temperatures in a ferromagnetic material.

A.1.1.5. Antiferromagnetism

Antiferromagnetism (AF) is a form of magnetism resulting from anti-parallel (exactly equal and opposite) aligned spins on different sub-lattices in a material as shown in Figure A.7 (a). Thus, no net spontaneous magnetism is present in antiferromagnetic materials. In addition, these materials have no hysteresis, but a small positive susceptibility. Above a critical temperature known as the *Néel temperature* (T_N), the susceptibility obeys the Curie-Weiss law for paramagnetism (i.e. spins are randomly oriented) with a negative intercept indicative of *negative* exchange interactions. These exchange interaction act to anti-align neighbouring spins in different sub-lattices. The spins become randomly oriented because the thermal energy is large enough to destroy the magnetic ordering. However, below T_N the electron spins are anti-parallel and hence no net magnetisation. The interaction between the spins strongly opposes an external field resulting in a decrease in the susceptibility with decreasing temperature. Thus, the T_N is the temperature above which an antiferromagnetic (or ferrimagnetic) material becomes paramagnetic. Figure A.7 (b) depicts the antiferromagnetic and paramagnetic behaviours below and above T_N, respectively. The variation of magnetisation as a function of applied field at different temperatures is shown in Figure A.7 (c).

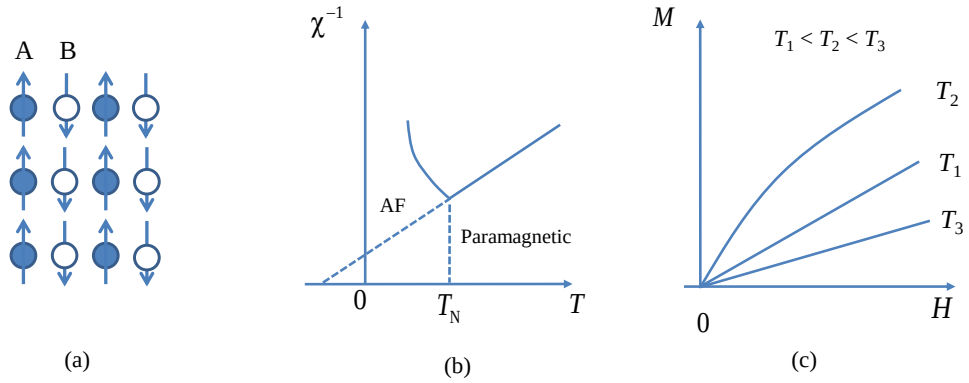


Figure A.7: (a) Spin lattice arrangements in an antiferromagnetic material (b) Temperature dependence of χ^{-1} (c) $M(H)$ curve at different temperatures.

A.1.2. Density of states on ferromagnetic material

The most important property of a ferromagnetic material is spontaneous magnetism due to strong collective ordering of neighbouring magnetic moments. Schematic illustrations [250] of the electronic density of states available in a ferromagnetic

material compared to a normal metal are shown in Figures A.8 (a) and (b), respectively. In a ferromagnetic material the *d* band is split into spin-up and spin-down sub-bands with corresponding states displaced in energy with respect to each other. Consequently, the spin-up sub-band is filled first while the remaining electrons occupy the spin-down. As a result, the difference in the number of electrons with spin-up and spin down gives rise to the spontaneous magnetic moment.

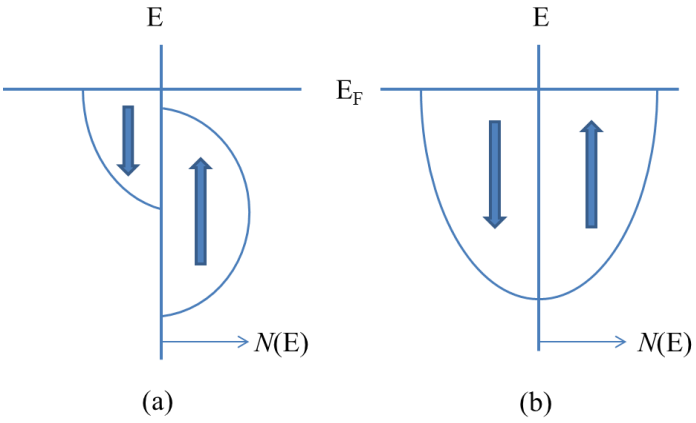


Figure A.8: Schematic illustration of the electronic density of states in (a) A ferromagnetic metal and (b) A normal metal. [Adopted from Prinz 1998 [250]]

Appendix B: FeAl Detector Development

B.1. Introduction

The FeAl detector developed is a parallel plate avalanche detector (PPAC) similar in design and working principle to the ^{57}Fe-enriched stainless steel discussed in section 3.6.3.1. The main aim of this project is to develop a more efficient detector for both online and offline emission Mössbauer spectroscopy measurements by utilising multiple FeAl plates. The first stage involved the construction of the detector with a single FeAl layer and the determination of best operating condition of bias voltage, acetone gas pressure and plate separation distance.

B.2. FeAl sample preparation

The FeAl plates were prepared by Marat Minnekaev and Andrei V. Zenkevich at the NRNU Moscow Engineering Physics Institute in Russia. The samples were produced by co-deposition of Fe and Al onto Be substrates at room temperature using pulsed laser deposition (PLD) technique in a dedicated vacuum setup with a base pressure $<10^{-5}$ Pa. Enriched ^{57}Fe (95.2 %) and Al elemental targets were alternately ablated using YAG:Nd^{3+} laser operating in the *Q*-switched regime with 150 mJ energy (t = 15 ns) and 45 Hz repetition frequency. The deposition rate was in the range 0.2-0.4 nm.s^{-1} (≈0.01 nm per laser pulse). The Fe-Al alloy composition was controlled by setting the number of pulses on each target as calibrated with RBS which was performed with 2 MeV $4He^{+}$ ions. ^{54}Fe was used at the bottom and on top to prevent the functional layer from oxidising and to exclude possible reactions with the substrate during the annealing. After the deposition the samples were annealed in high vacuum chamber of the PLD setup at the optimised temperature of T = 470ºC for ~24 hours.

B.3. Typical FeAl Mössbauer Spectrum

A typical emission Mössbauer spectrum obtained for the prepared FeAl sample was analysed with an asymmetric single line as shown in Figure B.1. The spectrum was recorded for 90s with an operating negative bias voltage of 620 V, plate separation of 1.66 mm and acetone gas pressure of 35 mbar. The asymmetry in the spectrum

stems from the non-linear BCC phase of FeAl which is Fe rich (Al vacancies). An isomer shift of ~0.30(1) mm/s and a linewidth of ~0.23(1) was extracted from the analysis. The isomer shift compares well with a value of 0.27(2) mm/s reported by Mielczarek and Papaconstantopoulos [251] while the linewidth is lower than an average value of 0.34 mm/s used for the ^{57}Fe-enriched stainless steel detector.

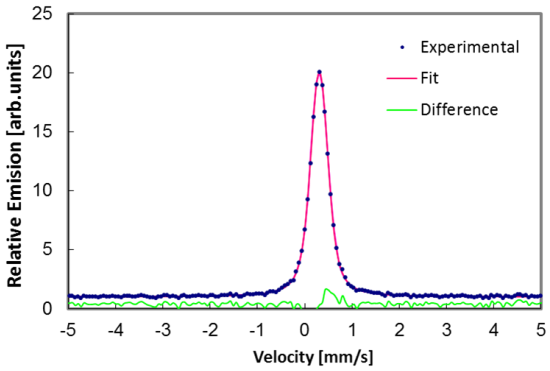


Figure B.1: Typical emission Mössbauer spectrum for FeAl sample with a signal to background ratio ~20.

B.4. Theory behind offline tests

A typical folded Mössbauer spectrum illustrating the maximum counts (m_p), background counts (B) and the relative signal (S) is depicted in Figure B.2.

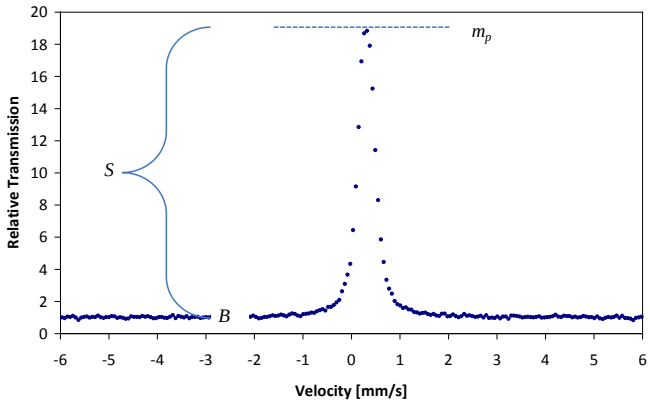


Figure B.2: FeAl emission Mössbauer spectrum illustrating spectral parameters.

The objective of the detector optimisation is to maximise the signal to noise (S/N) ratio per unit time.

The signal is given by the relation

$$S = (m_p - 1).B, \tag{B.1}$$

and the noise (N) is given by

$$N = \sqrt{m_p.B}. \tag{B.2}$$

Dividing yields the signal to noise ratio

$$S/N = \left(\frac{m_p - 1}{m_p}\right).\sqrt{B}, \tag{B.3}$$

and using the assumption,

$$b = \frac{\Delta B}{\Delta t}, \tag{B.4}$$

yields

$$S/N = \left(\frac{m_p - 1}{m_p}\right)\sqrt{b.t}. \tag{B.5}$$

However, m_p is a variable dependant on the relative solid angle (Ω) which is dependent on the strength of radioactive source S_s, surface area of the FeAl foils (A) and the source-FeAl foil distance (D), and can the expressed by the relation:

$$\Omega = \frac{S_s.A}{4\pi D^2}. \tag{B.6}$$

Thus defining an optimisation parameter C_s which is directly proportional to the signal to noise ratio (from equation B.5) and related to the solid angle effect yields,

$$C_s = \left(\frac{4\pi D^2}{S_s A}\right)\left(\frac{m_p - 1}{m_p}\right)\sqrt{b}\ . \tag{B.7}$$

B.5. Offline Tests Measurements

The electronics illustrated in the experimental set-up shown in Figure 3.13 was employed for detector optimisation tests to collect Mössbauer spectra. Initial detector tests were carried out at the Institute of Physics and Astronomy, Aarhus University after assembly of the detector components and similar experiment were later performed at iThemba LABS using the detector by varying the acetone vapour pressure (P) from 5 to 50 mbar taking 5 mbar steps at each plate separation distances, **s** = 1.16, 1.66, 2.16 and 2.66 mm as a function of bias voltage. A source of approximately 28 mCi was placed a distance of about 12 mm and 23 mm from the face detector and FeAl plate. An additional HV connection to a multimeter was incorporated to the set-up to obtain digital reading of the bias voltage.

B5.1. Data Analysis and Results

The analysis of Mössbauer data was done following the theory prescribed above and the results of different C_s values obtained for different gas pressures for each of the four plate separation distances are presented in Figure B.3.

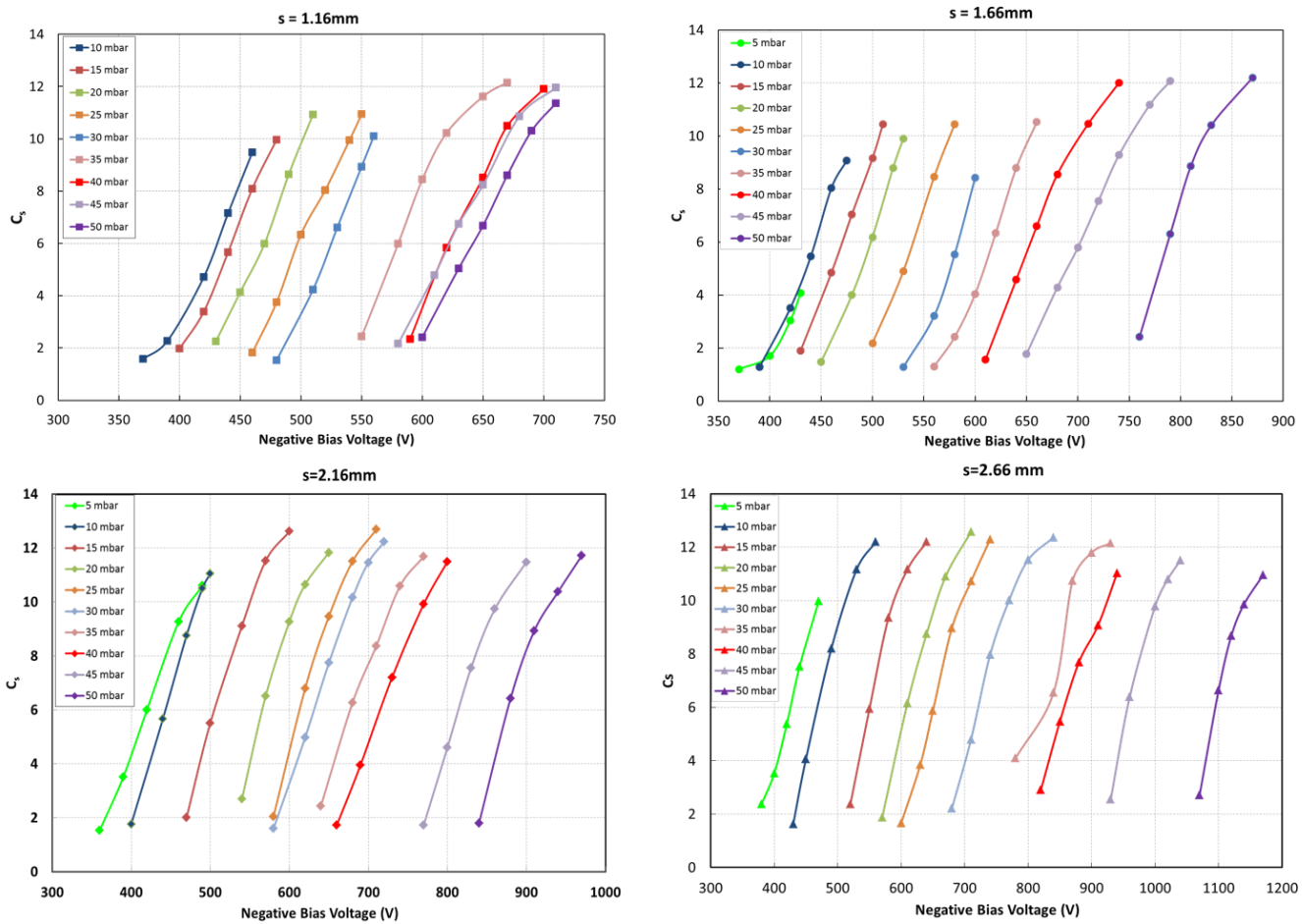


Figure B.3: Curves of optimisation parameters obtain as a function of acetone vapour pressure and bias voltage at plate separation distances indicated.

The results show that increasing the bias voltage increase the optimisation parameter stemming from the increase in charge multiplication in the acetone vapour contained between the parallel plates. Moreover, it is evident that increasing separation distance of the plates increases the range of operation of the bias voltage as evident by the maximum operating voltages reached at high gas pressure values. In addition, different C_s values are obtained at different gas pressures and bias voltage values at the four different plate separations:

- For the minimum plate separation distance of **s** = 1.16 mm, a maximum C_s value of ~12 is obtained for a gas pressures of 30, 40 and 45 mbar when the detector is operated at voltages between 680-720 V.
- For **s** = 1.66, a maximum value of C_s ~ 12 is obtained for the detector filled with acetone vapour pressure of 40, 45 and 50 mbar with a voltage operating range of 740 – 875 V.
- C_s values of 12.7(1) and 12.6(1) were obtained for the detector when the distance separating the plates is set to 2.16 mm at gas pressures of 15 mbar and 25 mbar, respectively. The detector was operated at voltages of ~ 600 V and 720 V each corresponding to the respective C_s and pressure values.
- A maximum C_s value of 12.6(1) is obtained for **s** = 2.66 mm with the detector operating at ~ 710 V and with a gas pressure of 20 mbar. In addition, average C_s values above 12 are obtained for the voltage range 550 – 940 V with corresponding acetone vapour pressures between 10 – 35 mbar.

Moreover, the linewidth was observed to increase with increasing bias voltage for different operating condition of gas pressure and plate separation distances. For example, values varying from ~0.17(1) mm/s to 0.27(1) mm/s with increasing operating voltages of ~ 390 V to ~ 870 V were obtained for a plate separation of 1.66 mm/s and pressures of 10 mbar and 50 mbar, respectively.

B.6. Online Detector Tests Measurements

In addition to offline laboratory tests, an online emission Mössbauer measurement was performed at ISOLDE on the AlN sample following $^{57}Mn^{*}$ implantation. AlN was chosen because the room temperature spectrum obtained on a narrow velocity

scale revealed more complicated features compared to GaN and InN hence was the ideal sample to perform a test measurement using the FeAl detector with a view to further resolve the spectral features. Figure B.3 shows the visual inspection spectra for AlN obtained at room temperature using the FeAl and stainless steel detectors.

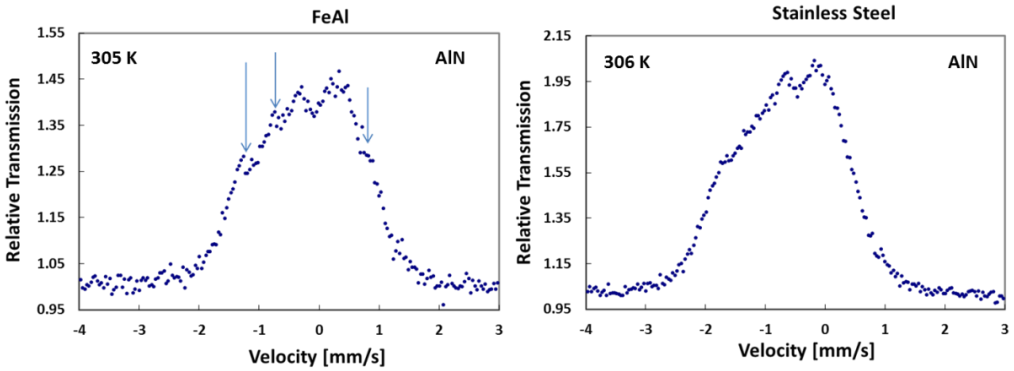


Figure B.4: $^{57}Mn^{*}$ emission Mössbauer spectra for AlN obtained with FeAl and stainless steel detectors, respectively.

Clearly the spectrum measured with the FeAl detector shows more features as indicated by the arrows. In addition the spectral lines are much sharper compared to the spectrum obtained with the stainless steel detector.

B.7. Conclusion and Future Tests

Offline detector test measurements show that increasing the plate separation distance increases the bias voltage operation range at equivalent gas pressures. Moreover, an average maximum C_s value of ~12.5(1) was obtained for various combinations of bias voltage and gas pressure. Future offline measurements for a wide range of values for the plate separation distance will be carried out to determine the breakdown voltage of the gas as a function of pressure and plate separation distance. The visual inspection spectrum for AlN obtained using the FeAl detector clearly revealed more spectral features compared to that measured with the stainless steel. As a result, more online test measurements are planned during the next beam time. This will be followed by the second phase which involves incorporating more FeAl parallel plates to increase detector efficiency and lower data acquisitions times.

References

[1] Bardeen, J.: *Nobel Lecture* (1956) 318.

[2] Bardeen, J. and Brattain, W. H.: *Phys. Rev.*, **74** (1948) 230.

[3] Baibich, M.N., Broto, J.M., Fert, A., Nguyen Van Dau, F., and Petroff, F.: *Phys. Rev. Lett.*, **61** (1988) 2472.

[4] Binasch, G., Grünberg, P., Saurenbach, F., and Zinn, W.: *Phys. Rev. B*, **39** (1989) 4828.

[5] Fert, A.: *Rev. Mod. Phys.*, **80** (2008) 1517.

[6] Wolf, S. A., Awschalom, D. D., Buhrman, R. A., Daughton, J. M. *et al.*: *Science*, **294** (2001) 1488.

[7] Narisetti, R.: *The Wall Street Journal* (10 November 1997) B8.

[8] Ohno, H.: *Science*, **281** (1998) 951.

[9] Pereira, L.M.C.: *Structure and magnetism of transition-metal implanted dilute magnetic semiconductors*. PhD Thesis, Katholieke Universiteit Leuven, 2011.

[10] Steigmeier, E.F. and Harbeke, G.: *Phys. Kondens. Materie.*, **12** (1970) 1.

[11] Treitinger, L., Pink, H., Mews, H., and Köpl, R.: *J. Magn. Magn. Mater.*, **3** (1976) 184.

[12] Mauger, A. and Godart, C.: *Phys. Rep.*, **141** (1986) 1375.

[13] van Son, P. C., van Kempen, H., and Wyder, P.: *Phys. Rev. Lett.*, **58** (1987) 2271.

[14] Valet, T. and Fert, A.: *Phys. Rev. B.*, **48** (1993) 7099.

[15] Barnaś, J. and Bruynseraede, Y.: *Europhys. Lett.*, **32** (1995) 167.

[16] Mott, N. F.: *Proc. R. Soc. Lond. A*, **153** (1936) 669.

[17] Nesbet, R. K.: *J. Phys.:Condens. Matter.*, **6** (1994) L449.

[18] Lui, C., Yun, F., and Morkoç, H.: *J. Mater. Sci. Mater. Electron.*, **16** (2005) 555.

[19] Dietl, T., Ohno, H., Matsukura, F., Cibert, J., and Ferrand, D.: *Science*, **287** (2000) 1019.

[20] Liu, C., Yun, F., and Morkoç, H.: *J. Mater. Sci. Mater. Electron.*, **16** (2005) 555.

[21] Bonanni, A.: *Semicond. Sci. Technol.*, **22** (2007) R41.

[22] Pereira, L.M.C., Araujo, J.P., Wahl, U., Decoster, S., Van Bael, M.J., Temst, K., and Vantomme, A.: *J. Appl. Phys.*, **113** (2013) 023903.

[23] Avrutin, V., Izyumskay, N., Ozgur, U., Silversmith, D. J., and Morkoc, H.: *Proc. IEEE*, **98** (2010) 1288.

[24] Ando, K.: *Science*, **312** (2006) 1883.

[25] Özgür, Ü., Alivov, Ya. I., Liu, C., Teke, A. *et al.*: *J. Appl. Phys.*, **98** (2005) 041301.

[26] Zunger, A., Lany, S., and Raebiger, H.: *Physics*, **3** (2010) 53.

[27] Dietl, T.: *Nature. Mater.*, **9** (2010) 965.

[28] Ohno, H., Shen, A., Matsukura, F., Oiwa, A., Endo, A., Katsumoto, S., and Iye, Y.: *Appl. Phys. Lett.*, **69** (1996) 363.

[29] Wang, M., Campion, R.P., Rushforth, A.W., Edmonds, K. W., Foxox, C.T., and Gallagher, B.L.: *Appl. Phys. Lett.*, **93** (2008) 132103.

[30] Pearton, S. J., Abernathy, C. R., and Ren, F.: *Gallium Nitride Processing for Electronics, Sensors and Spintronics*. Springer-Verlag, London, 2006.

[31] Quay, R.: In Hull, R. *et al.*, eds., *Gallium Nitride Electronics - Springer series in MATERIALS SCIENCE*. Springer, 2008.

[32] Yue, H., Jinfeng, Z., Bo, S., and Xinyu, L.: *J. Semicond.*, **33** (2012) 081001.

[33] Yao, T. and Hong, S., eds.: *Oxide and Nitride Semiconductors*. Springer, Berlin, Heidelberg, 2009.

[34] Sato, K. and Katayam-Yoshida, H.: *Jpn J. Appl. Phys.*, **39** (2000) L555.

[35] Slack, G. A. and T. F. McNelly.: *J. Cryst. Growth.*, **34** (1976) 263.

[36] Chin, V. W. L., Tansley, T. L., and T. Osotchan.: *J. Appl. Phys.*, **75** (1994) 7365.

[37] Harima, H.: *J. Phys-Condens. Matter*, **14** (2002) R967.

[38] T. L. Tansley.: In H, Edgar J., ed., *Properties of Group III nitrides - EMIS Data Reviews Series*. INSPEC, 1994.

[39] Geurts, J.: Crystal Structure, Chemical Binding, and Lattice. In Hull, R. *et al.*, eds., *Zinc Oxide - From Fundamental Properties Towards Novel Applications*. Springer , Heidelberg Dordrecht London New York, 2010.

[40] Pankove, J. I. and Schade, H.: *Appl.Phys. Lett.*, **25** (1974) 53.

[41] Marmalyuk, A. A., Akchurin, R. Kh., and Gorbylev, V. A.: *High. Temp.*, **36** (1998) 839.

[42] Nipko, J. C., Loong, C.-K., Balkas, C. M., and Davis, R. F.: *Appl. Phys. Lett.*, **73** (1998) 34.

[43] Davydov, V. YU., Emtsev, V. V., Goncharuk, I. N., Smirnov, A. N. *et al.*: *Appl. Phys. Lett.*, **75** (1999) 3297.

[44] Robie, R.A., Haselton Jr., H.T., and Hemingway, B.S.: *J. Chem. Thermodynamics*, **21** (1989) 743.

[45] Ioffe Institute, St. Petersburg, http://www.ioffe.rssi.ru/SVA/NSM.

[46] Hanada, T.: Basic Properties of ZnO, GaN, and Related Materials. In Yao, T. and Hong, S., eds., *Oxide and Nitride Semiconductors - Processing, Properties and Applications*. Springer, Berlin Heidelberg, 2009.

[47] Baur, W.H.: *Cryst. Rev.*, **1** (1987) 59.

[48] Jeffs, N.J., Blant, A. V., Cheng, T. S., Foxon, C. T. *et al.*: *Mat. Res. Soc. Symp. Proc.*, **512** (1998) 519.

[49] Vurgaftman, I., Meyer, J.R., and Ram-Mohan, L.R.: *J. Appl. Phys.*, **89** (2001) 5815.

[50] Dmitriev, A. V. and Oruzheinikov, A.L.: *Mat. Res. Soc. Symp. Proc.*, **423** (1996) 69.

[51] Davydov, V. Yu., Klochikhin, A. A., Seisyan, R. P., Emtsev, V. V. *et al.*: *Phys. Stat. Sol. (B)*, **229** (2002) R1.

[52] Davydov, V. Yu., Klochikhin, A. A., Emtsev, V. V., Kurdyukov, D. A. *et al.*: *Phys. Stat. Sol. (B)*, **234** (2002) 787.

[53] Matsuoka, T., Okamoto, H., M.Nakao, Harima, H., and Kurimoto, E.: *Appl. Phys. Lett.*, **81** (2002) 1246.

[54] Davydov, V. Yu., Klochkin, A. A., Emtsev, V. V., Ivanov, S. V. *et al.*: *Phys. Stat. Sol. (B)*, **230** (2002) R4.

[55] Wu, J., Walukiewicz, W., Yu, K.M., J.W.Ager *et al.*: *Appl. Phys. Lett.*, **80** (2002) 3967.

[56] Wu, J., Walukiewicz, W., Shan, W., yu, K.M. *et al.*: *Phys. Rev. B*, **66** (2002) 201403.

[57] Inushima, T., Mamutin, V. V., Vekshin, V. A., Ivanov, S. V., Sakon, T., Motokowa, M., and Ohoya, S.: *J. Cryst. Growth.*, **227-228** (2001) 481.

[58] Pearton, S. J., Norton, D. P., Ip, K., Heo, Y. W., and Steiner, T.: *Progress in Material Science*, **50** (2005) 293.

[59] Phillips, J. C.: *Rev. Mod. Phys.*, **42** (1970) 317.

[60] Ziegler, J. F.: Ion Implantation Physics. In Ziegler, J. F., ed., *Handbook of Ion Implantation Technology*. North Holland, 1992.

[61] Desnica, U.V., Ulri, N.B., and Etlinger, B.: *Phys. Rev. B*, **15** (1977) 4119.

[62] Van Vechten, J.A.: In Ulri, N.B. and Corbett, J.W., eds., *Radiation Effects in Semiconductors, IOP Conf. Ser. 31*. Institute of Physics, London, 1977.

[63] Nord, J., Nordlund, K., and Keinonen, J.: *Phys. Rev. B*, **68** (2003) 184104.

[64] Xiao, H.Y., Gao, F., Zu, X.T., and Weber, W.J.: *J. Appl. Phys.*, **105** (2009) 12527.

[65] Look, D.C., Reynolds, D.C., Hemsky, J.W., Sizelove, J.R., and Molnar, R.J.: *Phys. Rev. Lett.*, **79** (1997) 2273.

[66] Ionascut-Nedelcsescu, A., Carlone, C., A., Houdayer., von Bardelleben, H.J., Cantin, J.L., and Raymond, S.: *IEEE Trans. Nucl. Sci.*, **49** (2002) 2733.

[67] Van Vechten, J. A.: A simple man's view of the thermochemistry of semiconductors. In Moss, T. S. and Keller, S. P., eds., *Handbook on Semiconductors*. North-Holland, Amsterdam, 1980 p102.

[68] Wendler, E.: *AIP Conf. Proc.*, **1336** (2011) 621.

[69] Ziegler, F. J. and Biersack, J. P.: *James Zeigler - SRIM & TRIM, http://www.srim.org*.

[70] Jones, R.E.: *Electrical and optical characterization of group III-nitride alloys for solar energy conversion.* ProQuest, UMI Dissertation Publishing, 2011.

[71] Zinkle, S. J. and Kinoshita, C.: *J. Nucl. Mater.*, **251** (1997) 200.

[72] Lorenz, K., Alves, E., Wendler, E., Bilani, O., Wesch, W., and Hayes, M.: *Appl. Phys. Lett.*, **87** (2005) 191904.

[73] Locker, D. R. and Meese, J. M.: *IEEE Trans. Nucl. Sci.*, **19** (1972) 237.

[74] Pazionis, G. and Schulz, H. -J.: *Mater. Sci. Forum*, **10-12** (1986) 839.

[75] Erhart, P., Juslin, N., Goy, O., Nordlund, K., Müller, R., and Albe, K.: *J. Phys.: Condens. Matter.*, **18** (2006) 6585.

[76] Tan, H.H., Williams, J.S., Zou, J., Cockayne, D.J.H., S.J., Pearton, and Stall, R.A.: *Appl. Phys. Lett.*, **69** (1996) 2364.

[77] Liu, C., Mensching, B., Volz, K., and Rauschenbach.: *Appl. Phys. Lett.*, **71** (1997) 2313.

[78] Williams, J.S.: *Materials Science and Engineering*, **A253** (1998) 8.

[79] Lorenz, K., Alves, E., Gloux, F., Ruterana, P., Peres, M., Neves, A.J., and Monteiro.: *J. Appl. Phys.*, **107** (2010) 023525.

[80] Liu, C., Alves, E., Sequeira, A.D., Franco, N., Silva, M.F. da, and Soares, J.C.: *J. Appl. Phys.*, **90** (2001) 81.

[81] Kucheyeva, S.O. and Williams, J.S. Pearton, S.J.: *Materials Science and Engineering*, **33** (2001) 51.

[82] Azarov, A. Y., hallen, A., Jensen, J., and Aggerstam, T., Lourdudoss, S.: *J. Phys. Conf. Ser.*, **100** (2008) 042036.

[83] Lacroix, B., Chauvat, M.P, Ruterana, P., Alves, E., and Syrkin, A.: *J. Phys. D: Appl. Phys.*, **44** (2011) 295402.

[84] Gou, Q., Kato, O., and A., Yoshida.: *J. Appl. Phys.*, **73** (1993) 7969.

[85] Shrestha, S.K., Timmers, H., Scott, K., Butcher, A., Wintrebert-Fouquet, M., and Chen, P.P.-T.: *Nucl. Instr. and Meth. in Phys. Res. B*, **234** (2005) 291.

[86] Emstev, V.V., Davydov, V.Y., Haller, E.E., Klochikhin, A.A. *et al.*: *Physica B*, **208-310** (2001) 58.

[87] Mkhoyan, K.A. and Silcox, J.: *Appl. Phys. Lett.*, **82** (2003) 859.

[88] Tuomisto, F.: *J. Phys.: Conf. Ser.* , **265** (2011) 012003.

[89] Ganchenkova, M.G. and Nieminen, R.M.: *Phys. Rev. Lett.*, **96** (2006) 196402.

[90] Uedono, A., Ito, K., Nakamori, H., Mori, K. *et al.*: *J. Appl. Phys.*, **102** (2007) 084505.

[91] Saarinen, K., Suski, T., Grzegory, I., and Look, D.C.: *Physica B*, **308–310** (2001) 77.

[92] Saarinen, K., Suski, T., Grzegory, I., and Look, D.C.: *Phys. Rev. B*, **64** (2001) 233201.

[93] Lee, J.S., Lim, J.D., Khim, Z.G., Park, Y.D., Pearton, S. J., and Chu, S.N.G.: *J. Appl. Phys.*, **93** (2003) 4512.

[94] Kim, W., Kang, H.J., Oh, S.K., Shin, S.W. *et al.*: *Journal of Magnetics.* , **11** (2006) 16.

[95] Kim, W., Kang, H.J., Noh, S.K., Song, J., and Kim, C.S.: *J. Magn. Magn. Mater.*, **310** (2007) e729.

[96] Talut, G., Reuther, H., Zhou, S., Potzger, K., Eichhorn, F., and Stromberg, F.: *J. Appl. Phys.* , **102** (2007) 083909.

[97] Wang, X., Yang, S., Wang, J., Li, M. *et al.*: *J. Cryst. Growth.*, **226** (2001) 123.

[98] Kaschner, A., Haboeck, U., Strassburg, M., Kaczmarczyk, G. *et al.*: *Appl. Phys. Lett.*, **80** (2002) 1909.

[99] Wang, Y.G., Lau, S.P, Zhang, X.H., Lee, H.W., H.H., Hng, and B.K., Tay.: *J. Cryst. Growth.*, **252** (2003) 265.

[100] Bundesmann, C., Ashkenov, N., Schubert, M., Spemann, D. *et al.*: *Appl. Phys. Lett.*, **83** (2003) 1974.

[101] Manjón, F.J., Marĭ, B., Serrano, J., and Romero, A.H.: *J. Appl. Phys.* , **97** (2005) 053516.

[102] Zhang, B., Li, Q.H., Shi, L.Q., Cheng, H.S., and Wang, J.Z.: *Nucl. Instr. and Meth. B*, **266** (2008) 4891.

[103] Zhong, H., Wang, J., Chen, X., Li, Z., W., Xu, and Lu, W.: *J. Appl. Phys.*, **99** (2006) 103905.

[104] Alves, E., Lui, C., Waerenborgh, J.C., Silva, M.F. da, and Soares, J.C.: *Nucl. Instru. and Meth. in Phys. Res.*, **B175-177** (2001) 241.

[105] Wahl, U., Vantomme, A., Langouche, G., Correia, J.G., Peralta, L., and Collaboration, The ISOLDE.: *Appl. Phys. Lett.*, **78** (2001) 3217.

[106] Vantomme, A., Vries, B. De, and Wahl, U.: In O'Donell, K. and Dierolf, V., eds., *Topics in Applied Physics: Rare Earth Doped III-Nitrides for Optoelectronics and Spintronics Applications*. Springer, 2010.

[107] Ronning, C., Dalmer, M., Uhrmacher, M., Restle, M. *et al.*: *J. Appl. Phys.*, **87** (2000) 2149.

[108] Dhara, S., Sundaravel, B., Nair, K.G.M., Kesavamoorthy, R. *et al.*: *Appl. Phys. Lett.*, **88** (2006) 173110.

[109] Borowski, M., Traverse, A., and Eymery, J. P.: *Nucl. Instr. Meth. B*, **122** (1997) 247.

[110] Talut, G., Reuther, H., Mücklich, A., Eichhorn, F., and Potzger, K.: *Appl. Phys. Lett.*, **89** (2006) 161909.

[111] Talut, G., Reuther, H., Grenzer, J., Mucklich, A., Shalimov, A., Skorupa, W., and Stromberg, F.: *Phys. Rev. B*, **81** (2010) 155212.

[112] Lorenz, K., Ruske, F., and Vianden, R.: *Phys. Stat. Sol.(B)*, **228** (2001) 331.

[113] Miranda, S.M.C., Franco, N., Alves, E, and Lorenz, K.: *Nucl. Instr. and Meth. in Phys. Res. B*, **289** (2012) 43.

[114] Miranda, S.M.C., Kessler, P., Coreia, J.G., Vianden, R., Johnston, K., Alves, E., and Lorenz, K.: *Phys. Stat. Sol. (C)*, **9** (2012) 1060.

[115] Kessler, P., Lorenz, K., Miranda, S.M.C., Simon, R. *et al.*: *Phys. Stat. Sol. (C)*, **9** (2012) 1032.

[116] Potzger, K., Zhou, S., Reuther, H, Mucklich, A. *et al.*: *Appl. Phys. Lett.*, **88** (2006) 052508.

[117] Zhou, S., Potzger, K., Reuther, H, Talut, G. *et al.*: *J. Phys. D: Appl. Phys.*, **40** (2007) 964.

[118] Potzger, K., Zhou, S., Reuther, H, Kuepper, K. *et al.*: *Appl. Phys. Lett.*, **91** (2007) 062107.

[119] Monteiro, T., Boemare, C., Soares, M. J., E., Rita, and Alves, E.: *J. Appl. Phys.*, **93** (2003) 8995.

[120] Rita, E., Wahl, U., Correia, J. G., Alves, E., Soares, J.C., and Collaboration, The ISOLDE.: *Appl. Phys. Lett.*, **85** (2004) 4899.

[121] Pereira, L.M.C., Som, T., Demeulemeester, J., Van Bael, M. J., Temst, K., and Vantomme, A.: *J. Phys.: Condens. Matter*, **23** (2011) 346004.

[122] Bonanni, A., Kiecana, M., Simbrunner, C., Li, T. *et al.*: *Phys. Rev. B*, **75** (2007) 125210.

[123] Frazier, R. M., Stapleton, J., Thaler, G.T., Abernathy, C.R. *et al.*: *J. Appl. Phys.*, **94** (2003) 1592.

[124] Belabbes, A., Zaoui, A., and Ferhat, M.: *Appl. Phys. Lett.*, **97** (2010) 242509.

[125] Xie, Q.Y., Gu, M.Q., Huang, L., Zhang, F.M., and Wu, X.S.: *AIP Advances*, **2** (2012) 012185.

[126] Wu, P., Saraf, G., Lu, Y., Hill, D. H. *et al.*: *Appl. Phys. Lett.*, **89** (2006) 012508.

[127] Norton, D. P., Overberg, M. E., Pearton, S. J., Pruessner, K. *et al.*: *Appl. Phys. Lett.*, **83** (2003) 5488.

[128] Akdogan, N., Nefedov, A., Westerholt, K., Zabel, H. *et al.*: *J. Phys. D: Appl. Phys.*, **41** (2008) 165001.

[129] Potzger, K., Kuepper, K. Xu, Q., Zhou, S., Schmidt, H., Helm, M., and Fassbender, J.: *J. Appl. Phys.*, **104** (2008) 023510.

[130] Zhou, S., Potzger, K., Talut, G., Reuther, H *et al.*: *J. Phys. D: Appl. Phys.*, **41** (2008) 105011.

[131] Matei, E., Enculescu, I., Vasilache, V., and Teodorescu, C. M.: *Phys. Stat. Sol. (A)*, **207** (2010) 2517.

[132] Zhang, Z. H., Müller, S., Ronning, C., Wang, X. F., Xu, J. B., and Quan, L.: *Nat. Nanotechnol.*, **4** (2009) 523.

[133] Schumm, M., Koerdel, M., Müller, S., Ronning, C. *et al.*: *J. Appl. Phys.*, **105** (2009) 083525.

[134] Pereira, L.M.C., Araujo, J.P., Van Bael, M.J., Temst, K., and Vantomme, A.: *J. Phys. D: Appl. Phys.*, **44** (2011) 215001.

[135] Zener, C.: *Phys. Rev.*, **81** (1951) 440.

[136] Ruderman, M. A. and Kittel, C.: *Phys. Rev.*, **96** (1954) 99.

[137] Kasuya, T.: *Prog. Theor. Phys.*, **16** (1956) 45.

[138] Yosida, K.: *Phys. Rev.*, **106** (1957) 893.

[139] Coey, J.M.D., Venlatesan, M., and Fitzgerald, C.B.: *Nat. Mat.*, **4** (2005) 173.

[140] Pemmaraju, C. D. and Sanvito, S.: *Phys. Rev. Lett.*, **94** (2005) 217205.

[141] Osorio-Guillén, J., Lany, S., Barabash, S. V., and Zunger, A.: *Phys. Rev. Lett.*, **96** (2006) 107203.

[142] Bouzerar, G. and Ziman, T.: *Phys. Rev. Lett.*, **96** (2006) 207602.

[143] Coey, J. M. D., Wongsaprom, K., Alaria, j., and Venkkatesan, J.: *J. Phys. D: Appl. Phys.*, **41** (2008) 134012.

[144] Potzger, K. and Zhou, S.: *Phys. Stat. Sol. (B)*, **246** (2009) 1147.

[145] Zhou, S., Potzger, K., Xu, Q., Talut, G. *et al.*: *Vacuum*, **83** (2009) S13.

[146] Kapilashrami, M., Xu, J., Ström, V., Rao, K. V., and Belova, L.: *Appl. Phys. Lett.*, **95** (2009) 033104.

[147] Khalid, M., Ziese, M., Setzer, A., Esquinazi, P. *et al.*: *Phys. Rev. B*, **80** (2009) 035331.

[148] Wang, Q., Sun, Q., Chen, G., Kawazoe, Y., and Jena, P.: *Phys. Rev. B*, **77** (2008) 205411.

[149] Wang, Q., Sun, Q., Jena, P., and Kawazoe, Y.: *Phys. Rev. B*, **79** (2009) 115407.

[150] Mølholt, T. E., Mantovan, R., Gunnlaugsson, H. P., Naidoo, D. *et al.*: *Hyp. Int.* , **197** (2010) 89.

[151] Gunnlaugsson, H. P., Mølholt, T. E., Mantovan, R., Masenda, H. *et al.*: *Appl. Phys. Lett.*, **97** (2010) 142501.

[152] Gunnlaugsson, H. P., Mantovan, R., Mølholt, T. E., Naidoo, D. *et al.*: *Hyp. Int.* , **198** (2010) 5.

[153] Mølholt, T. E, Gunnlaugsson, H. P., Johnston, K, Mantovan, R. *et al.*: *Phys. Scr.*, **T148** (2012) 014006.

[154] Weyer, G., Gunnlaugsson, H. P., Mantovan, R., Fanciulli, M., Naidoo, D., Bharuth-Ram, K., and Agne, T.: *J. Appl. Phys.*, **102** (2007) 113915.

[155] Gunnlaugsson, H. P., Johnston, K., Mølholt, T. E., Weyer, G. *et al.*: *Appl. Phys. Lett.*, **100** (2012) 042109.

[156] de Biasi, R.S. and Portella, P.D.J.: *J. Magn. Magn. Mater.*, **15** (1980) 737.

[157] Bhargava, S. C., Knudsen, J. E., and Mørup, S.: *J. Phys. Chem. Solids.*, **40** (1979) 45.

[158] Abragam, A. and Bleaney, B.: Spin-Phonon Interaction. In *Electron Paramagnetic Resonance of Transition Metals*. Oxford University Press, London, 1970.

[159] Poole, Jr. C. P. and Farach, H. A.: *Relaxation in Magnetic Resonance - Dielectric and Mössbauer Applications*. Academic Press, New York and London, 1971.

[160] Srivastava, K. K. P. and Mishra, S. N.: *Phys. Stat. Sol. (B)*, **100** (1980) 65.

[161] Stevens, K. W. H.: *Rep. Prog. Phys.*, **30** (1967) 189.

[162] Shrivastava, K. N.: *Phys. Stat. Sol. (B)*, **117** (1983) 437.

[163] Zhang, G., Hübner, W., Beaurepaire, E., and Bigot, J-Y.: Laser-Induced Ultrafast Demagnetization: Femtomagnetism, a New Frontier? In Hillebrands, B. and Ounadjela, K., eds., *Spin Dynamics in Confined Magnetic Structures I*. Springer, Berlin Heidelberg, 2002.

[164] Orbach, R.: *Proc. R. Soc. Lond. A*, **264** (1961) 458.

[165] Van Vleck, J. H.: *Phys. Rev.*, **57** (1940) 426.

[166] Kohmoto, T., Sakaguchi, H., Takahashi, M., Kakita, K., Koyama, Y., and Moriyasu, T.: *Phys. Rev. B*, **78** (2008) 144420.

[167] Singh, J.: *Quantum Mechanics: Fundamentals and Applications to Technology*. Wiley-VCH , Weinheim, 2004.

[168] Talut, G., Grenzer, J., Reuther, H., Shalimov, A., Baehtz, C., Novikov, D., and Walz, B.: *Appl. Phys. Lett.*, **95** (2009) 232506.

[169] Zhou, S., Potzger, K., Talut, G., Reuther, H *et al.*: *J. Appl. Phys.*, **103** (2008) 023902.

[170] Coey, J.M.D, Wongsaprom, K., Alaria, J., and Venkatesan, M.: *J. Phys. D: Appl. Phys.*, **41** (2008) 134012.

[171] Coey, J.M.D., Stamenov, P., Gunning, R.D., Venkatesan, M., and Paul, K.: *New J. Phys.*, **12** (2010) 053025.

[172] Masenda, H., Naidoo, D., Bharuth-Ram, K., Gunnlaugsson, H. P. *et al.*: *Hyp. Int.*, **198** (2010) 15.

[173] Bharuth-Ram, K., Dlamini, W. B., Masenda, H., Naidoo, D. *et al.*: *Nucl. Instr. Meth. B* , **272** (2011) 414.

[174] De Wit, M. and Estle, T.L.: *Phys. Rev.*, **132** (1963) 195.

[175] Mössbauer, R.: *Hyp. Int.*, **126** (2000) 1.

[176] Albanese, G., Fabri, G., Lamborizio, C., Musci, M., and Ortalli, I.,.: *IL Nuove Cimento*, **L.B, N.1** (1967).

[177] Masenda, H.: *^{57}Fe Mössbauer investigations in GaAs and GaP following implantation of ^{57}Mn**. Master's Dissertation, University of the Witwatersrand, 2010.

[178] Mössbauer, R.: *Noble Lecture* (1961) 584.

[179] Gutlich, P., Bill, E, and Trautwein, A.: *Mössbauer Spectroscopy and Transition Metal Chemistry*. Springer-Verlag, 2011.

[180] Gunther, W. K.: *Mössbauer Effect: Principles and Applications*. Academic Press, New York and London, 1964.

[181] Schiffer, J. P. and Marshall, W.: *Phys. Rev. Lett.*, **3** (1959) 556.

[182] Pound, R. V. and Rebka Jr, G. A.: *Phys. Rev. Lett.*, **3** (1959) 554.

[183] Kolk, B.: *S. Afr. J. Sci.*, **83** (1987) 480.

[184] Williamson, D.L., Niesen, L., Weyer, G., Sielemann, R., and Langouche, G.: Mössbauer spectroscopy. In Langouche, G., ed., *Hyperfine Interaction of Defects in Semiconductors*. Elsevier, Amsterdam, 1992.

[185] Chen, Y. and Yang, D.: *Mössbauer Effect in Lattice Dynamics-Experimental Techniques and Applications.* Willey-VCH, Weinheim, 2007.

[186] Mössbauer Spectroscopy. In *Physics and Chemistry of The Earth*. Elsevier, 1992.

[187] Cadogan, J.M. and Ryan, D.H.: Mössbauer Spectroscopy. In Vij, D.R., ed., *Handbook of Applied Solid State Spectroscopy*. Springer US, 2006.

[188] Kuzmann, E., Nagy, S., and Vertes, A.: *Pure Appl. Chem., IUPAC*, **75** (2003) 801.

[189] Dyar, M.D., Agresti, D.G., Schaefer, M.W., Grant, C.A., and Sklute, E.C.: *Annu. Rev.Earth Planet. Sci.*, **34** (2006) 83.

[190] Collins, R. L.: *J. Chem. Phys.*, **42** (1965) 1072.

[191] Ingalls, R.: *Phys. Rev.*, **133** (1964) A787.

[192] Lin, C.M. and Lin, S.T.: *J. Phys. Condens. Matter* , **5** (1993) L247.

[193] Christiansen, J., Heubes, P., Keitel, R., Klinger, W., Loeffler, W., Sander, W., and Witthuhn, W.: *Z. Phys. B*, **24** (1976) 177.

[194] Kaufmann, E. N. and Vianden, R. J.: *Rev. Mod. Phys.* , **51** (1979) 161.

[195] van Zorge, B. C., Caspers, W. J., and Dekker, A. J.: *Phys. Stat. Sol.*, **18** (1966) 761.

[196] Raj, P. and Kulshreshtha, S. K.: *Phys. Stat. Sol. (A)*, **4** (1971) 501.

[197] Nastasi, M. and Mayer, J. W.: *Ion Implantation and Synthesis of Materials*. Springer, Verlag Berlin Heidelberg New York, 2006.

[198] Langouche, G and Yoshida, Y.: Ion Implantation. In Yoshida, Y and Langouche, G, eds., *Mössbauer Spectrsoscopy*. Springer, Verlag Berlin Heidelberg, 2013.

[199] Rimini, R.: Ion Implantation. In Levy, R. A, ed., *Microelectronic Materials and Processes*. Kluwer Academic Plublishers, Dordrecht, 1989.

[200] Dearnaley, G.: *Annu. Rev. Mater. Sci.*, **4** (1974) 93.

[201] Larson, L. A., Williams, J. M., and Current, M. I.: *Reviews of Accelerator Science and Technology*, **4** (2011) 11.

[202] Gibbons, J. F.: *Proc. IEEE*, **56** (1968) 295.

[203] Gibbons, J. F.: *Proceedings of the IEEE*, **60** (1972) 1062.

[204] Cook, D. C.: *Hyp. Int.*, **141/142** (2002) 21.

[205] Dhanaraj, G. *et al.*, eds.: *Springer Handbook of Crystal Growth*. Springer, Verlag Berlin Heidelberg, 2010.

[206] Auger, M. A., Vazquez, L., Jergel, M., Sanchez, O., and Albella, J. M.: *Surface and Coating Technology*, **180-181** (2004) 140.

[207] Wang, J., Chen, D., Xu, Y., Liu, Q., and Zhang, L.: *Journal of Spectroscopy*, **2013** (2013) 103602.

[208] Gao, X., Wang, S., Li, J., Zheng, Y. *et al.*: *Journal of the Korean Physical Society*, **44** (2004) 765.

[209] Kim, W., Aktas, O, Botchkarev, A. E., Salvador, A., Mohammad, S. N., and Morkoc, H.: *J. Appl. Phys.*, **79** (1996) 7657.

[210] Jamil, M., Arif, R. A., Ee, Y., Tong, H., Higgins, J. B., and Tansu, N.: *Phys. Stat. Sol. (A)*, **205** (2008) 1619.

[211] Lu, H., Schaff, W. J., Hwang, j., Wu, H., Yeo, W., Pharkya, A., and Eastman, L. F.: *Appl. Phys. Lett.*, **77** (2000) 2548.

[212] Vispute, R. D., Wu, H., and Narayan, J.: *Appl. Phys. Lett.*, **67** (1995) 1549.

[213] Kuzmann, E., Homonnay, Z., Nagy, S., and Nomura, K.: Mössbauer Spectroscopy. In Vértes, A. *et al.*, eds., *Handbook of Nuclear Chemistry*. Springer US, 2011.

[214] Deicher, M., Weyer, G., Wichert, Th., and collaboration, the ISOLDE.: *Hyp. Int.*, **151/152** (2003) 105.

[215] Dézsi, I.: *J. Radioanal. Nucl. Chem.* , **190** (1995) 225.

[216] Weyer, G.: Applications of Parallel-Plate Avalanche Counters in Mössbauer Spectroscopy. In Gruverman, I.J. and Seidel, C. W., eds., *Mössbauer Effect Methodology*. Plenum, New York, 1976.

[217] Weyer, G., Petersen, J.W, and Damgaard, S.: *Physica* , **116B** (1983) 470.

[218] Weyer, G.: *Hyp. int.*, **177** (2007) 1.

[219] Foner, S.: *Rev. Sci. Instrum.*, **27** (1956) 548.

[220] Wecker, J., Bayreuther, G., Ross, G., and Grössinger, R.: Magnetic Properties. In Czichos, H. *et al.*, eds., *Springer Handbook of Metrology and Testing*. Springer , Berlin Heidelberg, 2011.

[221] Foner, S.: *J. Appl. Phys.*, **79** (1996) 4740.

[222] Doyle, T. B.: *Fluxon pinning and geometrical Effects in a type II superconductor*. PhD Thesis, University of the Witwatersrand, (1975).

[223] Mørup, S.: In Gütlich, P. *et al.*, eds., *Mössbauer Spectroscopy and Transition Metal Chemistry: Fundamentals and Application*. Springer, Berlin, 2010.

[224] Heitz, R., Thurian, P., Loa, I., Eckey, L. *et al.*: *Appl. Phys. Lett.*, **67** (1995) 2822.

[225] Blume, M. and Tjon, J. A.: *Phys. Rev.*, **165** (1968) 446.

[226] Gunnlaugsson, H. P.: *Vinda: users-phys.au.dk/hpg/vinda.htm*. Aarhus University, (2011).

[227] Bonanni, A., Przybylinska, H., Wolos, A., Simbrunner, C. *et al.* In *Proceedings of the GMe Forum* (2005).

[228] Bonanni, A., Simbrunmer, C., Wegscheider, M., Przybylinska, H., Wolos, A., Sitter, H., and Jantsch, W.: *Phys. Stat. Sol. (B)*, **243** (2006) 1701.

[229] Bharuth-Ram, K., Gunnlaugsson, H. P., Mantovan, R., Naicker, V. V. *et al.*: *Hyp. Int.*, **1-3** (2008) 621.

[230] Bharuth-Ram, K., V., Naicker V., Naidoo, D., Gunnlaugsson, H. P. *et al.*: *Hyp. Int.*, **179** (2007) 17.

[231] Gunnlaugsson, H. P., Bharuth-Ram, K., Dietrich, M., Fanciulli, M., Fynbo, H. O. U., and Weyer, G.: *Hyp. Int.*, **169** (2006) 1319.

[232] Jencic, I., Bench, M. W., Robertson, I. M., and Kirk, M. A.: *J. Appl. Phys.*, **78** (1995) 974.

[233] Weyer, G. and Collaboration, the ISOLDE.: *Hyp. Int.*, **129** (2000) 371.

[234] Gunnlaugsson, H. P.: *Manuscripts in preparations [from Internal Notes]*.

[235] Naidoo, D, Gunnlaugsson, H. P., Mølholt, T. E., Mantovan, R. *et al.*: *Hyp. Int.*, **221** (2013) 45.

[236] Mantovan, R., Gunnlaugsson, H. P., Mølholt, T. E., Naidoo, D. *et al.*: *Manuscript in Preparation*.

[237] Tronc, E., Chaneac, C., and Jolivet, J. P.: *J. Solid State Chem.*, **139** (1998) 93.

[238] Zboril, R., Mashlan, M., and Petridis, D.: *Chem. Mater.*, **14** (2002) 969.

[239] Zboril, R., Mashlan, M., Machala, L., and Bezdicka, P.: Iron(III) oxide formed during thermal conversion of rhombohedral iron(III) sulphate. In Mashlan, M. *et al.*, eds., *Material Research in Atomic Scale by Mössbauer Spectroscopy*. Kluwer Academic Press, Netherlands, 2003.

[240] Lancok, A., Miglierini, M., and Kohout, J.: *The Physics of Metals and Metallography*, **109** (2010) 524.

[241] Machala, M. and Tucek, J. Zboril, R.: *Chem. Mater.*, **23** (2011) 3255.

[242] Tucek, J., Ohkoshi, S., and Zboril, R.: *Appl. Phys. Lett.*, **99** (2011) 253108.

[243] Tucek, J., Zboril, R., Namai, A., and Ohkoshi, S.: *Chem. Mater.*, **22** (2010) 6483.

[244] Ligenza, S., Lukasiak, M., Kucharski, Z, and Suwalski, J.: *Phys. Stat. Sol (B)*, **117** (1983) 465.

[245] Bharuth-Ram, K., Masenda, H., Doyle, T. B., Geburt, S., Ronning, C., and Gunnlaugsson, H. P.: *Hyp. Int.*, **207** (2012) 49.

[246] Potzger, K., Kuepper, K., Xu, Q., Zhou, S., Schmidt, H., Helm, M., and Fassbender, J.: *J. Appl. Phys.*, **104** (2008) 023510.

[247] Gunnlaugsson, H. P., Olafsson, S., Bharuth-Ram, K., Correia, J. G. *et al.*: *Emission Mössbauer spectroscopy of advanced materials for opto- and nano- electronics*. ISOLDE, CERN, Geneva, [Addendum submitted to the INTC] 2012.

[248] Bonanni, A., Gunnlaugsson, H. P., Mantovan, R., Masenda, H. *et al.*: *Magnetic and structural properties of manganese doped (Al,Ga)N studied with Emission Mössbauer spectroscopy*. Geneva, ISOLDE/CERN, [Proposal Sumbitted to INTC] 2013.

[249] Heo, Y. W., Kelly, J., Norton, D. P., Hebard, A. F., Pearton, S. J., Zavada, J. M., and park, Y. D.: *Semicond. Sci. Technol.*, **4** (2004) 312.

[250] Prinz, G. A.: *Science*, **828** (1998) 1660.

[251] Mielczarek, E. V. and Papaconstantopoulos, D. A.: *Phys. Rev. B*, **17** (1978) 4223.